A Thesis Submitted for the Degree of PhD at the University of Warwick

Permanent WRAP URL:

http://wrap.warwick.ac.uk/152817

Copyright and reuse:

This thesis is made available online and is protected by original copyright.
Please scroll down to view the document itself.
Please refer to the repository record for this item for information to help you to cite it.
Our policy information is available from the repository home page.

For more information, please contact the WRAP Team at: wrap@warwick.ac.uk

warwick.ac.uk/lib-publications

Nonlinear Methods for Modelling Atomistic Brittle Fracture

Punit Patel

Thesis submitted for the degree of

Doctor of Philosophy

University of Warwick, School of Engineering

September 2019

Contents

Contents **i**

List of Figures **v**

List of Tables **ix**

Acknowledgements **xi**

Declaration **xiii**

Abstract **xv**

Acronyms **xvii**

1 Introduction **1**

2 Background **5**

- 2.1 Introduction 5
- 2.2 Atoms 5
- 2.3 Quantum Mechanics 6
  - 2.3.1 Density Functional Theory 8
- 2.4 Classical Mechanics 15
  - 2.4.1 Molecular Dynamics 16
  - 2.4.2 Interatomic Potentials 17
  - 2.4.3 Dynamics at Finite Temperature 19
- 2.5 Multiscale Mechanics 20
- 2.6 Geometry Optimisation 24
  - 2.6.1 Steepest Decent Method 24
  - 2.6.2 Fast Inertial Relaxation Engine Method 25
  - 2.6.3 Broyden–Fletcher–Goldfarb–Shanno Method 25

2.6.4 Limited-Memory Broyden–Fletcher–Goldfarb–Shanno Method 26
2.6.5 Interior-Point Primal-Dual Newton Method 27
2.7 Surface Energy 30
2.8 Linear Elasticity 31
2.9 Brittle Fracture 34
2.9.1 Griffith Thermodynamic Energy Balance 34
2.9.2 Stress Intensity Factor 36
2.9.3 Mode I Fracture 39
2.10 Materials 39
2.10.1 Crystals 39
2.10.2 Carbon 40
2.10.3 Silicon Carbide 41
2.10.4 Two Dimensional Hexagonal Lattice 42
2.11 Simple Potentials 43
2.12 Force Locality 46
2.12.1 Molecular Dynamics 47
2.12.2 Forces 48
2.13 Summary 51

3 Brittle Fracture of Silicon Carbide 53
3.1 Introduction 53
3.2 Background 54
3.2.1 Silicon Carbide 54
3.2.2 Statistical Thermodynamics 56
3.2.3 Phonons 57
3.2.4 Finite Temperature Surface Energy 62
3.2.5 Thin Strip Geometry 62
3.3 Methodology 63
3.3.1 Experimental 63
3.3.2 Computational 66
3.4 Results and Discussion 75
3.4.1 Experimental 75
3.4.2 Computational 79
3.4.3 Discussion: Experimental and Computational 87
3.5 Conclusion 89

4 Energy Paths for Crack Propagation 91
4.1 Introduction 91
4.2 Background 92
4.2.1 Energy Barriers 92
4.2.2 Lattice Trapping 94
4.2.3 Pseudo Arc-length Continuation Method 95
4.2.4 Hausdoff Distance 98
4.3 Methodology 99
4.3.1 Static and Flexible Boundaries 99
4.3.2 Strained Surface Energy 105
4.3.3 Pseudo Arc-length Continuation Scheme 106
4.3.4 Fitting the Crack Tip 113
4.3.5 Initial Stress Intensity Factor 115
4.4 Results and Discussion 116
4.4.1 Static and Flexible Boundaries 116
4.4.2 Strained Surface Energy 120
4.4.3 Pseudo Arc-length Continuation Scheme 122
4.5 Conclusion 126

5 Nonlinear Elastic Boundary Conditions 129
5.1 Introduction 129
5.2 Background 130
5.2.1 Pair Constrained Minimisation 130
5.3 Methodology 131
5.3.1 Correction Scheme 131
5.3.2 Convergence Tests 135
5.4 Results and Discussion 138
5.4.1 Minimisation Strain Error 138
5.4.2 Corrected Displacements 140
5.4.3 Forces 140
5.4.4 Strain and Energy Errors 144
5.5 Conclusion 148

6 Conclusion 151

Bibliography 153

List of Figures

2.1 Schematic of the real part of a one dimensional probabilistic wavefunction. 6
2.2 Schematic of the pseudo functions used in density functional theory (DFT). 13
2.3 Physical descriptions with respect to the length scales and timescales which are accessible via modelling techniques. . . 21
2.4 Graphical representation of the maximum principal stress around a crack tip, of a system under uniaxial tension. 22
2.5 Example of a bulk crystal system and a slab system used to calculate the surface energy. 31
2.6 Schematic of a stress-strain curve. 32
2.7 Schematic of the three modes of fracture. 36
2.8 Schematic of Irwin's infinitesimal narrow slit crack geometry 37
2.9 Diamond-structured carbon slab with exposed (111) surfaces. 40
2.10 Silicon carbide (SiC) 6H unit cell. 41
2.11 Two dimensional (2D) hexagonal lattice. 42
2.12 Potential energy of a Lennard-Jones (LJ) potential with varying cutoffs. 44
2.13 Force response of a LJ potential with varying cutoffs. 46
2.14 Temperature evolution of a molecular dynamics (MD) simulation of a SiC 6H bulk system. 48
2.15 Schematic of the reference and perturbed configurations used for force locality tests. 49
2.16 Force locality graphs for SiC 6H and diamond-structured carbon. 50

3.1 Unit cells of SiC polytypes 3C and 6H. 55
3.2 Inequivalent surface terminations of the SiC 6H (0001) surface. 56
3.3 Schematic of the thin strip geometry. 62
3.4 Schematic of the double cantilever beam (DCB) geometry. . 64

3.5 SiC 6H (0001) surfaces terminated with hydrogen. 73
3.6 Scanning electron microscope (SEM) images of the loaded SiC DCB sample. 76
3.7 Data analysis of a SiC DCB sample. 77
3.8 Fracture energies of the SiC 6H (0001) surface, obtained through loading of a different DCB samples. 78
3.9 Fracture energies and surface energy of the SiC 6H (0001) surface. 80
3.10 Frames from a MD simulation of a fractured SiC 6H slab which was open along the (0001) plane. 81
3.11 Finite temperature surface energies for the SiC 6H (0001) surface 85

4.1 Schematic of an energy profile with respect to a reaction coordinate. 93
4.2 Schematic of the lattice trapping range. 94
4.3 Schematic of the pseudo arc-length continuation method. . . 96
4.4 A fractured diamond-structured carbon system which is open along the (111) plane. 101
4.5 Critical points along the energy paths for breaking a single bond ahead of the crack tip, for different stress intensity factors. 103
4.6 A mode I fracture system of a 2D hexagonal lattice. 108
4.7 Schematic of a continuation path. 109
4.8 Schematic of the energy paths extracted from a continuation path. 111
4.9 Visualisation of a fitted crack tip. 114
4.10 Energy profiles for breaking a single bond of a fractured diamond-structured carbon system, which was open along the (111) plane, for a range of stress intensity factors. 117
4.11 Key stress intensity factors of a fractured diamond-structured carbon system which was open along the (111) plane, for multiple system sizes. 118
4.12 Convergence of the errors of key stress intensity factors of a fractured carbon system, with respect to system size. 119
4.13 Strain components of atoms along the crack surfaces. 121
4.14 Surface energy as a function of strain. 122

4.15 Continuation paths for fractured 2D hexagonal lattices of different system sizes. 124
4.16 Continuation path of a fractured 2D hexagonal lattice with a few extracted energy paths. 125
4.17 Normalised errors of the energy barrier and key stress intensity factors. 127
4.18 Hausdorff distance between the continuation paths of the radially smaller systems and the continuation path of the reference system. 127

5.1 Schematic diagram for generating an initial stable crack configuration. 134
5.2 Schematic of the systems used to compute the correction term and perform the convergence tests. 135
5.3 Decay of the strain error as a result of minimisation for different potentials. 139
5.4 A fractured 2D hexagonal lattice, with the continuum linear elastic (CLE) displacement, and the corrected CLE displacements, viewed close to the crack tip. 141
5.5 Decay of the atomic forces within a fractured 2D hexagonal lattice, using the CLE displacements and the corrected displacements. 142
5.6 Sum of the force components within a ball of a given radius, for the CLE displacements and the corrected displacements, with respect to the size of the ball. 143
5.7 Strain error of a fractured 2D hexagonal lattice with respect to a reference system, for the CLE displacements and the corrected displacements. 144
5.8 Convergence of the strain error and the energy error with respect to system size, of the CLE displacements and the corrected displacements, using an ideal brittle solid (IBS) potential. 146
5.9 Convergence of the strain error and the energy error with respect to system size, of the CLE displacements and the corrected displacements, using the LJ potential. 147

List of Tables

3.1 Lattice structure and the stacking sequence of the silicon carbide (SiC) polytypes 3C and 6H. 55

3.2 A passivated surface energy value, from density functional theory (DFT) using the Perdew–Burke–Ernzerhof (PBE) exchange correlation functional, for the SiC 6H (0001) surfaces. 82

3.3 DFT surface energy values for the SiC 6H (0001) surface, of two exchange correlation functionals local density approximation (LDA) and PBE. 84

3.4 Computed lattice constants, for the SiC 6H and SiC 3C unit cells. 86

3.5 Fracture energy, surface energy, and fracture toughness, of the SiC 6H (0001) surface and the equivalent SiC 3C (111) surface. 88

Acknowledgements

Funding and Resources

This work would not have been possible without funding from the Engineering and Physical Sciences Research Council (EPSRC), who also provided financial support for several conferences and workshops which were influential in my development. Thanks to the people that keep the computational resources up and running at the University of Warwick Scientific Computing Research Technology Platform (SCRTP) and at the Argonne National Laboratory. Thanks to the hundreds of developers that contribute to the packages and programming languages used throughout this work.

Professional

A huge thanks to James Kermode, who was instrumental in his support. It was also a joy to work with him. Some of the work would not have been possible without the help and inspiration of others, in particular: Lars Pastewka, Christoph Ortner, Maciej Buze, Julian Braun, and Giorgio Sernicola.

Lunch?

To the members of the *Lunch?* group, who have made life, inside and outside the university, much more satisfying, and who have kept me sane throughout the years. I am grateful for the countless hours of time spent together and the hours of conversation, which ranged from thought-provoking to utterly ridiculous and were always filled with *banter*. In quintessential British *tradition*, some of those hours were coupled with one or two *b........................eers.*

Declaration

This thesis is submitted to the University of Warwick in support of my application for the degree of Doctor of Philosophy. It has been composed by myself and has not been submitted in any previous application for any degree.

The work presented was carried out at the School of Engineering, University of Warwick, between October 2015 and September 2019 under the supervision of Dr. J. R. Kermode. The work presented, including data generated and data analysis, was carried out by the author except in the cases outlined below:

- Experimental silicon carbide (SiC) work in Chapter 3.

Parts of this thesis have been published between October 2015 and September 2019:

- Experimental and density functional theory (DFT) work for SiC in Chapter 3.
  - Sernicola, G., Giovannini, T., Patel, P., Kermode, J. R., Balint, D. S., Britton, T. B. & Giuliani, F. In situ stable crack growth at the micron scale. *Nature Communications* **8,** 108. doi:10.1038/s41467-017-00139-w (Dec. 2017)

Parts of this thesis are in preparation for publication after September 2019:

- Pseudo arc-length work and boundary correction work in Chapter 4 and Chapter 5 respectively.
  - Patel, P., Buze, M., Pastewka, L., Braun, J., Ortner, C. & Kermode, J. R. *Atomistic Modelling of Fracture with Nonlinear Elastic Boundary Conditions (In prep.)*

Abstract

Fracture is a fundamental process through which materials fail. Our understanding of fracture mechanics determines our ability to predict the process.

Griffith first conceptualised a continuum description of fracture in the 1920s, and today, simulations are also performed at the atomistic scale. Hierarchical, and simultaneous, multiscale approaches are used; where DFT provides accurate electronic interactions at the crack tip coupled with classical mechanics to reach the large length scale required to capture the long range stress fields found in fractured systems. Here, tools are developed with hierarchical modelling in mind and to reduce computational cost.

The accuracy of DFT is demonstrated via a comparison to experimental fracture propagation of the SiC 6H polytype on the (0001) plane. The slow stable crack growth of the experiment allowed comparison of the experimentally measured fracture energy with the computational surface energy from DFT calculations, which showed relatively good agreement.

The discretised nature of an atomistic lattice leads to a feature called lattice trapping. To explore this, methods to compute energy barriers for breaking a single bond along the crack advancement direction were developed. The methods were tested on a fractured diamond-structured carbon system, which was open along the (111) plane, and a fractured 2D hexagonal lattice.

The continuum description for fracture is not sufficient for an atomistic lattice. A method which attempts to improve the discrepancy between the descriptions by computing a correction term on a larger atomistic domain was developed. It showed improved convergence of the strain and total energy with respect to the uncorrected case.

Acronyms

2D two dimensional.
3D three dimensional.

BFGS Broyden–Fletcher–Goldfarb–Shanno.

CASTEP Cambridge Serial Total Energy Package.
CLE continuum linear elastic.

DCB double cantilever beam.
DFT density functional theory.

EPSRC Engineering and Physical Sciences Research Council.

FIB focused ion beam.
FIRE fast inertial relaxation engine.

GGA generalised gradient approximation.

IBS ideal brittle solid.
ICSD Inorganic Crystal Structure Database.

KKT Karush–Kuhn–Tucker.
KMC kinetic Monte Carlo.

L-IBS linearised ideal brittle solid.
LBFGS limited-memory Broyden–Fletcher–Goldfarb–Shanno.
LDA local density approximation.
LJ Lennard-Jones.

MD molecular dynamics.
MM molecular mechanics.

PBE Perdew–Burke–Ernzerhof.

QM quantum mechanics.
QMC quantum Monte Carlo.

SCRTP Scientific Computing Research Technology Platform.
SEM scanning electron microscope.
SiC silicon carbide.
SW Stillinger-Weber.

1 Introduction

Structures and materials are designed to a specification and are expected to withstand their operating loads and stresses for the duration of their lifetime. Components are becoming increasingly complicated and are required to withstand greater demands. Materials are rarely perfect and consist of many defects, such as impurities, vacancies, dislocations, grain boundaries, and stacking faults. While production methods continue to improve, reducing the number of unwanted defects, flaws can still develop during their operation. These defects can compromise the integrity of the material and can develop into larger scale damage even within the specified conditions. This can cause a material to fail; whether it is an operational specification loss or structural loss, both can be costly and dangerous to the user.

The need for stronger, more resilient materials is present in several industries and is growing as demand for improved properties increases. For example, superalloys and ceramic-based materials have become popular in the aerospace industry [3], where their properties make them suitable for the extremely demanding conditions within a jet engine. Superalloys can have complex grain structures. The properties of superalloys have improved over time, with techniques such as grain boundary strengthening and manufacturing techniques which reduce the number of grain boundaries in the component [4]. Components formed from ceramic matrix composites overcome some limitations of conventional ceramics and superalloys, such as improved fracture toughness and a higher temperature performance respectively [5]. However, these components can still fail via fracture mechanisms. The competition to build more efficient and reliable engines to reduce the cost of travel and improve safety, respectively, is ever-present. This contributes to the demand for ceramic-based materials. Many industries can benefit from an increased understanding of fracture mechanics. However, the information can be difficult to obtain, and thus a need for improved design and simulation tools exist.

Our understanding of fracture mechanics determines our ability to predict the process. Griffith was amongst the first to formally conceptualise the failure of brittle materials in 1921 [6]. Griffith's ideas were developed in terms of macroscopic thermodynamic quantities, such that small thermal fluctuations are negligible and so do not affect the quantity of interest. Today, the field has progressed to modelling at the atomistic scale [7–9].

The dynamic behaviour of cracks is highly specific to the material under investigation and its structural changes as defects propagate can lead to complex behaviour [8]. Experimental investigations are often extremely expensive or even unachievable, especially at the atomistic scale, suggesting that alternative computational methods would be highly beneficial.

Accurate atomistic modelling of these processes, in principle, requires hundreds of thousands of atoms to represent the long range stress fields. Complex electronic interactions near the crack tip require modelling with quantum mechanical precision. These simulations are not feasible. It is possible to reduce the computational cost while maintaining comparable accuracy overall by considering molecular mechanics for longer range effects away from defect cores [10]. These simulations, often referred to as simultaneous simulations, reduce the cost; however, errors are introduced at the boundary at which the different modelling techniques come into contact. The simulations are still limited to the timescales available via methods used to model quantum mechanics (QM). Hierarchical modelling attempts to incorporate different modelling techniques via outputs of one that feed into the inputs of another [11]. This allows for simulations with greater timescales compared to simultaneous simulations. However, errors are introduced as information is lost when the physical description changes.

The computational cost of single atomistic scale simulations is still high and outside the realms of treatment using quantum mechanical accuracy. Here, methods to reduce the domain size are presented, with the intension that they could be run with higher accuracy mechanics.

The accuracy available through quantum mechanical simulations is demonstrated, in Chapter 3, with the computation of the surface energy for silicon carbide (SiC). SiC is mainly used as an abrasive with applications in semiconductors, cutting tools, body amour, and more recently automotive parts [12]. However, it can be difficult to work with due to its extremely brittle behaviour.

Differences exist between continuum and atomistic fracture theory due to the discrete nature of atomistic lattice sites. The nature of the lattice modifies the behaviour of the fracture dynamics giving rise to a phenomenon called *lattice trapping*. Lattice trapping and the related energy barriers required to advance the crack front are explored in Chapter 4. Energy barriers for diamond-structured carbon were computed. Diamond-structured carbon is also extremely brittle, and it is used commercially within many applications from gems to cutting tools [13]. Through use of a numerical continuation method, the lattice trapping range for a simple fractured two dimensional (2D) hexagonal lattice was found, as a proof of concept.

The application of continuum fracture theory to atomistic domains produces a discrepancy. To improve upon the discrepancy, a correction scheme is introduced, in Chapter 5, and demonstrated on a fractured 2D hexagonal lattice, as a proof of concept.

First, the concepts and theory regarding atomistic simulations of brittle fracture are outlined in Chapter 2.

2 Background

2.1 Introduction

Atomistic simulations of crack propagation are key to understanding the behaviour of materials [8, 14]. Modelling both the large length scale of a fractured system and the complex chemistry at the crack tip is a difficult task. Outlined below are the fundamental concepts and theory used to model atomistic systems, mainly classical mechanics and QM. In regards to fracture, only a small subset of the field is studied here. The continuum concepts of brittle fracture are outlined. Three materials were investigated in this work. Two real-world brittle materials were studied, and for proof of concept for the new methodology developed here a simple 2D hexagonal lattice was used.

2.2 Atoms

An atom consists of subatomic particles: protons, neutrons, and electrons. The protons and neutrons are localised at the centre of the atom, and together they are called the nucleus. The electrons exist beyond the nucleus and are bound electronically to the nucleus. These subatomic particles can be considered either classically as particles or through a quantum description as waves. Together, this is known as the *wave-particle duality* principle [15]. The quantum and classical characterisations are explained in further detail in the Sec. 2.3 and Sec. 2.4, respectively.

The energy, position, and electronic charge of an atom are important properties used to describe how a collection of atoms may interact with each other. The energy of an atom depends on several factors: its mass, i.e. the number of protons and neutrons; the likely locations of its electrons at a

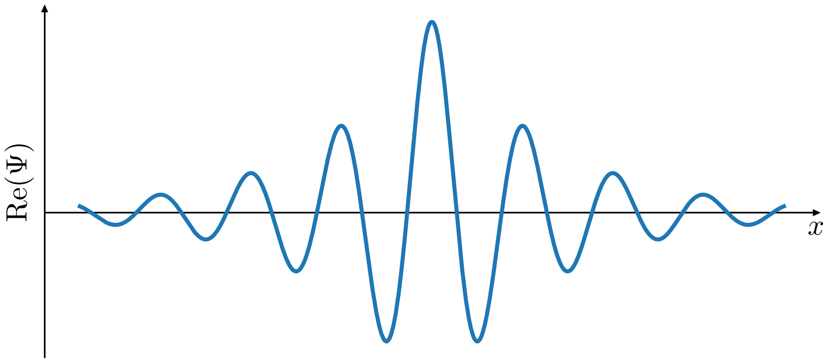

Figure 2.1: Schematic of the real part of a one dimensional probabilistic wavefunction, Ψ, where x is a spatial coordinate.

given time; and its momentum, i.e. its relative velocity in its inertial frame or its temperature. The electronic charge is dependent on the number of protons and electrons.

Atoms and their subatomic particles interact via the four fundamental forces: the gravitational, the electromagnetic, the weak, and the strong interaction. In materials the electromagnetic force is the governing force between atoms [15]. This interaction will modify the atom's energy either by changing its momentum, its position, or the likely positions of its electrons.

2.3 Quantum Mechanics

Accurate modelling of interactions between atoms requires consideration of nuclei and their electrons. In order to capture the nuclear and the electronic response of atoms interacting with one another, a first principles approach must be considered. QM establishes methods in which a system and its interactions can be represented as probabilistic wavefunctions, Fig. 2.1, where each particle is represented by a linear partial differential equation.

One formulation for QM relies on solving the Schrödinger equation. However, a direct analytical approach is practically impossible as it requires one to simultaneously solve this equation for all particles. Thus, approximations are needed in order to tackle anything beyond a system with a couple of hydrogen particles [16].

The general form for the time-independent Schrödinger equation is

$$E|\Psi\rangle = \hat{H}|\Psi\rangle, \tag{2.1}$$

where E is the energy of the system, $\hat{H}$ is the Hamiltonian operator, and Ψ is the wavefunction of the system [16]. The Hamiltonian operator describes the set of possible energies of a system and is comprised of the sum of the kinetic energies, $\hat{T}$, and potential energies, $\hat{V}$, expressed as

$$\hat{H} = \hat{T} + \hat{V}. \tag{2.2}$$

In a quantum description there are three interactions that contribute to the potential energy term: nucleus-nucleus, nn; nucleus-electron, ne; and electron-electron, ee. The kinetic energy term is the sum of the kinetic energies of the nuclei, n, and electrons, e. Hence, the Hamiltonian is expressed as

$$\hat{H} = \hat{T}_{\mathrm{e}} + \hat{T}_{\mathrm{n}} + \hat{V}_{\mathrm{nn}} + \hat{V}_{\mathrm{ne}} + \hat{V}_{\mathrm{ee}}. \tag{2.3}$$

For a many-body system the components of the Hamiltonian can be written as

$$\hat{T}_{\mathrm{e}} + \hat{T}_{\mathrm{n}} = -\frac{\hbar^2}{2m_{\mathrm{e}}}\sum_{i}^{N_{\mathrm{e}}}\nabla_i^2 - \frac{\hbar^2}{2}\sum_{I}^{N_{\mathrm{n}}}\frac{1}{m_I}\nabla_I^2, \tag{2.4}$$

$$\begin{split}\hat{V}_{\mathrm{nn}} + \hat{V}_{\mathrm{ne}} + \hat{V}_{\mathrm{ee}} = \frac{e^2}{4\pi\epsilon_0}\Bigg(\sum_{I}^{N_{\mathrm{n}}}\sum_{J>I}^{N_{\mathrm{n}}}\frac{Z_I Z_J}{|R_I - R_J|} - \sum_{i}^{N_{\mathrm{e}}}\sum_{I}^{N_{\mathrm{n}}}\frac{Z_I}{|r_i - R_I|}\\ + \sum_{i}^{N_{\mathrm{e}}}\sum_{j>i}^{N_{\mathrm{e}}}\frac{1}{|r_i - r_j|}\Bigg),\end{split} \tag{2.5}$$

where $\hbar$ is the reduced Planck constant; m_{e} is the mass of the electron; m_I is the mass of a nuclei; e is the elementary electronic charge; ϵ_0 is the vacuum permittivity; N_{e} and N_{n} are the number of electrons and nuclei respectively; i and j indices denote electrons; I and J indices denote nuclei; Z are the atomic numbers; r are the positions of the electrons; and R are the positions of the nuclei [16].

Solving the equations exactly is impossible for a many-body system and so approximations are used. One common method to simplify the Hamiltonian is using the Born-Oppenheimer approximation [17], which revolves around separating the motion of the nucleus from the electrons. The mass of a nucleus is orders of magnitude larger than that of an electron, and it can be considered that the motion of the nuclei is considerably slower than that of the electrons. First, the kinetic energy term regarding the nuclei, $\hat{T}_{\mathrm{n}}$, is neglected. The Schrödinger equation is solved for the electronic part. The term is later reintroduced and then solved for the nuclei only using classical mechanics. Thus, the approximation requires that the electronic response is instantaneous compared to nuclear motion, i.e. the electrons do not require a finite relaxation time. This is often also referred to as the *adiabatic approximation*. Therefore, the Hamiltonian for the electronic structure, i.e. ignoring the $\hat{T}_{\mathrm{n}}$ term, can be written as [18]

$$\hat{H} = \hat{T}_{\mathrm{e}} + \hat{V}_{\mathrm{nn}} + \hat{V}_{\mathrm{ne}} + \hat{V}_{\mathrm{ee}}. \tag{2.6}$$

The Born-Oppenheimer approximation allows for the separation of the wavefunction into two parts: the nuclear, Ψ_{n}, and the electronic, Ψ_{e}, such that $\Psi = \Psi_{\mathrm{n}}\Psi_{\mathrm{e}}$ [16]. This separation makes calculations of wavefunctions for elements larger than hydrogen possible. This approach is still limited to a few electrons. To go beyond this, further approximations of the Schrödinger equation are needed. There are two main types of methods: wavefunction-based methods and density-based methods. A density-based method used today is density functional theory (DFT), which was formulated in 1964 [19] and is still improved upon today. DFT is an approximate method, and thus there are issues with the methodology and its accuracy [20]. More accurate and more expensive methods exist, i.e. quantum Monte Carlo (QMC) and other similar approaches [21, 22]. However, DFT has become an accepted standard used by many today.

2.3.1 Density Functional Theory

DFT is a computational technique based on the framework by Hohenberg and Kohn [23]. One of its theorems states that the ground state energy of a system is uniquely related to its electron density, $n(r)$. The significance of this theorem is the reduction of variables in the model. A system of N electrons will have $3N$ spatial coordinates which get reduced down to an electron density of 3 spatial coordinates. From Eq. 2.1 and Eq. 2.6, the total energy of the electronic system, $E|\Psi_{\mathrm{e}}\rangle$, can be written as a functional of the density, $E[n(r)]$; thus

$$E|\Psi_\mathrm{e}\rangle = \big(\hat{T}_\mathrm{e} + \hat{V}_\mathrm{nn} + \hat{V}_\mathrm{ne} + \hat{V}_\mathrm{ee}\big)|\Psi_\mathrm{e}\rangle \tag{2.7}$$

is equivalent to

$$E_\mathrm{HK}[n(r)] = F_\mathrm{HK}[n(r)] + \int V_\mathrm{ext}(r)n(r)\ \mathrm{d}^3r + E_\mathrm{n}, \tag{2.8}$$

where F_HK is the unique Hohenberg-Kohn functional which includes all the kinetic energies, $\hat{T}_\mathrm{e}$, and potential energies, $\hat{V}_\mathrm{ee}$, of the underlying electron system; E_n includes the potential energies, $\hat{V}_\mathrm{nn}$, of the nuclei interactions; and V_ext is the external potential through which the electrons interact with the nuclei, $\hat{V}_\mathrm{ne}$ [18]. The square brackets denote functionals.

Kohn and Sham progressed the theoretical framework by assuming that the ground state density of an interacting system is equivalent to one of a non-interacting system [24]. The electron density is given in relation to the orbitals of each electron, which is

$$n(r) = \sum_s n(r,s) = \sum_s \sum_{i=1}^{N^s} |\psi_i^s(r)|^2, \tag{2.9}$$

where s denotes the spin of the electron, ψ is the particle's wavefunction, and N is the number of electrons. The Hohenberg-Kohn energy expression of Eq. 2.8 can be rewritten as

$$\begin{aligned} E_\mathrm{KS}[n(r)] =& T_s[n(r)] + E_\mathrm{Hartree}[n(r)] + E_\mathrm{xc}[n(r)] \\ &+ \int V_\mathrm{ext}(r)n(r)\ \mathrm{d}^3r + E_\mathrm{n}, \end{aligned} \tag{2.10}$$

where

$$T_s[n(r)] = \frac{1}{2}\sum_s \sum_{i=1}^{N^s} \int |\nabla\psi_i^s(r)|^2\ \mathrm{d}^3r \tag{2.11}$$

is the independent particles kinetic energy;

$$E_\mathrm{Hartree}[n(r)] = \frac{1}{2}\iint \frac{n(r)\rho(r')}{|r-r'|}\ \mathrm{d}^3r\ \mathrm{d}^3r' \tag{2.12}$$

is the self-interaction energy of the electron density, treated as a classical charge density; and

$$E_{\mathrm{xc}}[n(r)] = \frac{1}{2}\iint n(r)\frac{n_{\mathrm{xc}}(r,r')}{|r-r'|}\,\mathrm{d}^3r\,\mathrm{d}^3r' \tag{2.13}$$

is the exchange-correlation energy functional [18]. Exchange interactions are due to interactions between identical particles. Correlation interactions describe how one electron is effected by all the remaining electrons. Unfortunately, it is not possible to obtain an exact form of $E_{\mathrm{xc}}[n(r)]$ as the density of the exchange-correlation, n_{xc}, is unknown. Instead, $E_{\mathrm{xc}}[n(r)]$ is approximated. There are many functionals and many parametrisations of those functionals [25, 26] which are computed with more accurate and computationally expensive methods, such as QMC which is still an approximation [27]. Here, two exchange-correlation functionals are used. The local density approximation (LDA) exchange-correlation assumes that $E_{\mathrm{xc}}[n(r)]$ at each point is assumed to be the same as in an uniform electron gas with that density [18]. The generalised gradient approximation (GGA) builds upon LDA and considers density and the local gradient at each point; this allows for systems with more strongly fluctuating electronic densities [28].

Plane Wave Basis Set

While the Kohn-Sham formulation of DFT reduces the complexity to non-interacting particles and introduces the exchange-correlation energy functional term, the number of electrons to solve remain the same. This leaves the same number of equations to solve simultaneously. The dimensions of the problem can be reduced by using periodic domains. Bloch's theorem states that each electron in a periodic solid can be represented by a Bloch wave, $\psi(r)$, given as

$$\psi(r) = \phi(r)e^{ik\cdot r}, \tag{2.14}$$

where the $\phi(r)$ factor has the same periodicity as the domain periodicity, the wave-like part is captured by the $e^{ik\cdot r}$ factor, and k is the wave vector [29]. The periodicity of lattice allows for the solution of the Bloch wave to be characterised in a single Brillouin zone [30]. The domain periodicity can be rewritten using a basis set of discrete plane waves in reciprocal lattice vectors. Thus, the wavefunction becomes

$$\psi(r) = \sum_G c_{k+G} e^{i(k+G)\cdot r}, \tag{2.15}$$

where G are the reciprocal lattice vectors, and c_{k+G} are the plane wave coefficients. Modelling an infinite wave can be reduced by truncating the plane wave basis set. For sufficiently large kinetic energies, $|k + G|^2$, the plane wave coefficients, c_{k+G}, are less important than ones associated with smaller kinetic energies [29]. The truncation of the plane wave basis set is referred to as the *cutoff energy* [29], E_{cut}, given by

$$E_{\mathrm{cut}} = \frac{\hbar^2}{2m_{\mathrm{e}}}|k + G|^2. \tag{2.16}$$

This cutoff introduces an error which can be reduced or mitigated by converging the total energy with respect to E_{cut}, or additionally by using a *finite basis set correction* which applies a correction factor to account for the different number of k-points. This correction is particularly important for domains in which the domain size changes during computation of the Kohn-Sham equations [31].

k-point Sampling

While Bloch's theorem reduces the number of wavefunctions, the wavefunction still needs to be computed for an infinite number of k-points. However, the contributions to the wavefunction of k-points which are sufficiently close together are similar [29]. Hence, it is possible to reduce the number of k-points needed to represent a wavefunction. One method, used here, is the Monkhorst and Pack grid, which uses high symmetry sets of k-points within the Brillouin zone [32]. Using a reduced number of k-points introduces another source of error. This error can be reduced by converging the total energy with respect to the number of k-points used.

Pseudopotentials

Further simplifications can be made to reduce computational expense. The wavefunctions of the electrons are subject to an orthogonality constraint. As such, the wavefunctions of the valence electrons exhibit rapid oscillations in the core region which requires a very large basis set [29]. The size of the basis set can be reduced by considering the core electrons, i.e. tightly bound electrons, to be frozen with the nuclei. This introduces a *pseudopotential* to account for the change in interaction behaviour; a replacement for what would be a strong Coulombic potential with a weaker potential that acts on pseudo wavefunctions. This pseudo wavefunctions does not typically oscillate within the core region, so should not have any nodes, and thus the pseudo wavefunction requires a smaller basis set compared to its counterpart [29]. In this approach, it is assumed that chemical bonding does not involve any core electrons.

A pseudopotential should faithfully reproduce the valence functional form of the non-frozen electron model. Hamann *et al.* found norm-conserving pseudopotentials reproduce this behaviour [33]. Later, Vandererbilt relaxed the norm-conservation requirement to formulate ultrasoft pseudopotentials [34]. The smoother pseudopotential leads to a reduction in the plane wave cutoff energy, and thus a smaller basis set is required. This class of pseudopotentials were also found to have better transferability and accuracy compared to norm-conserving pseudopotentials [35]. A schematic of these pseudopotentials and pseudo wavefunctions are shown in Fig. 2.2.

Bloch's theorem only applies to periodic domains. Non-uniform, inhomogeneous, or anisotropic objects like defects and surfaces are not periodic. In order to model the object it must be surrounded by enough bulk periodic material such that the periodic image of the object does not interact with itself. This is called the *supercell approximation.*

These various approximations, and many more allow a computational approach for solving the Kohn-Sham DFT formulation to find the ground state energy of a system. Throughout this work the Cambridge Serial Total Energy Package (CASTEP) implementation of DFT was used [36].

Electronic Minimisation

The Kohn-Shan method provides a feasible approach to compute the ground state of the many-body electron system [18]. The solution to the Kohn-Sham formulation of the energy, shown in Eq. 2.10, can be solved as a minimisation

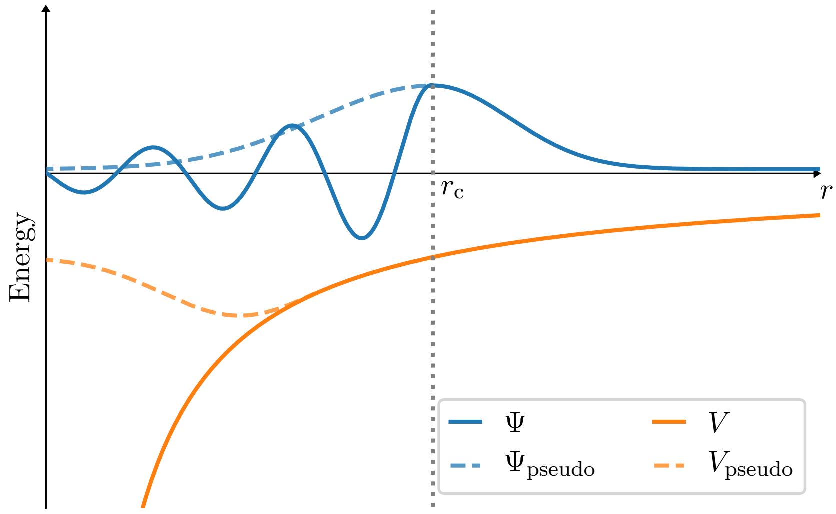

Figure 2.2: Schematic of the energy of an electron wavefunction, Ψ, and a potential, V, with respect to the distance from the centre of an atom, r. The pseudo wavefunction, Ψ_{pseudo}, and pseudopotential, V_{pseudo}, replace the description for the core electrons, below a cutoff radius, r_{c}, and match the real functions above r_{c} [29].

problem with respect to the wavefunction. The minimum [18] is given by

$$\frac{\delta E_{\mathrm{KS}}}{\delta \psi_i^{s*}(r)} = 0 \tag{2.17}$$

$$\frac{\delta T_s}{\delta \psi_i^{s*}(r)} + \left[\frac{\delta E_{\mathrm{ext}}}{\delta n(r,s)} + \frac{\delta E_{\mathrm{Hartree}}}{\delta n(r,s)} + \frac{\delta E_{\mathrm{xc}}}{\delta n(r,s)}\right]\frac{\delta n(r,s)}{\delta \psi_i^{s*}(r)} = 0 \tag{2.18}$$

where

$$\frac{\delta T_s}{\delta \psi_i^{s*}(r)} = -\frac{1}{2}\nabla^2 \psi_i^s(r), \tag{2.19}$$

$$\frac{\delta E_{\mathrm{ext}}}{\delta n(r,s)} + \frac{\delta E_{\mathrm{Hartree}}}{\delta n(r,s)} + \frac{\delta E_{\mathrm{xc}}}{\delta n(r,s)} = V_{\mathrm{KS}}^s(r), \tag{2.20}$$

and

$$\frac{\delta n(r,s)}{\delta \psi_i^{s*}(r)} = \psi_i^s(r). \tag{2.21}$$

From an effective Hamiltonian of $H^s_{\mathrm{KS}}(r) = -\frac{1}{2}\nabla^2 + V^s_{\mathrm{KS}}(r)$ the above equation can be rewritten as

$$(H^s_{\mathrm{KS}} - \epsilon^s_i)\psi^s_i(r) = 0 \tag{2.22}$$

where ϵ^s_i are the eigenvalues. These are the Kohn-Sham equations [18].

A minimisation of the Kohn-Sham equations provides a ground state energy and an electron density of the system. The equations are solved self-consistently via an iterative approach. First, an initial guess of the electron density is given. Then the effective potential $V^s_{\mathrm{KS}}(r)$ is calculated. The effective potential is used to solve the Kohn-Sham equations to provide new wavefunctions. A new electron density is calculated using the wavefunctions. This electron density is then used to compute a new effective potential. The iteration is repeated until changes in the energy are less than a given tolerance, or multiple tolerances of system properties are converged [18].

Geometry Optimisation

The minimisation of the energy with respect to the ionic positions, as well as the size and shape of the encompassing cell, can also be computed. This is achieved via computation of the forces on the ions themselves.

The Hellmann-Feynman theorem,

$$\frac{\partial E}{\partial \lambda} = \left\langle \psi_\lambda \middle| \frac{\partial H}{\partial \lambda} \middle| \psi_\lambda \right\rangle, \tag{2.23}$$

relates the derivative of the energy with respect to some parameter λ to the expectation value of the derivative of the Hamiltonian with respect to λ [16]. $\partial E/\partial \lambda$ can be interpreted as a generalised force associated with λ, if λ is a degree of freedom of the system. In the given approximate formulation of DFT, the ions of a system are treated as classical particles. Let λ be the position vector, then the Hellmann-Feynman force is the classical force on that ion [16]. The force on an ion via the Hellmann-Feynman theorem can be shown to be [18]

$$f_I = -\frac{\partial E_{\mathrm{KS}}}{\partial R_I} \tag{2.24}$$

$$= -\sum_i^N \left\langle \psi_i \middle| \frac{\partial H_{\mathrm{KS}}}{\partial R_I} \middle| \psi_i \right\rangle. \tag{2.25}$$

The minimisation of the forces are achieved in an iterative approach along with the electronic minimisation. The ions are moved along the direction of the force until the forces are below a tolerance using optimisation algorithms. The stress of the cell is computed and the cell vectors are adjusted until the stress is below a tolerance [29]. Further details regarding the optimisation algorithms are provided in Sec. 2.6.

2.4 Classical Mechanics

Classical mechanics is based on Newtonian mechanics and describes the motion of atoms using a particle description. Newton first proposed the method in the 17th century [37]. Improved reformulations and advancements such as Lagrangian mechanics were made in the 19th century [38], shortly followed by Hamiltonian mechanics.

The Hamiltonian, which often describes the total energy of a system, of a classical system is similar to that of Eq. 2.2. The total energy is comprised of the kinetic energy, T, and the potential energy, V. T is calculated using the momentum of a particle, p_i. V is calculated using a function which depends on the positions, $\{r_i\}$, and often other atomistic or system properties. Thus, the Hamiltonian, H, which is equal to the total energy, E, is

$$H = T(\{p_i\}) + V(\{r_i\}), \tag{2.26}$$

where i is the particle index; $\{p_i\}$ denotes the set of all momenta; and $\{r_i\}$ denotes the set of all positions. The kinetic energy is given by

$$T(\{p_i\}) = \sum_i^N \frac{p_i^2}{2m_i}, \tag{2.27}$$

where m is the mass of the particle [39]. The force on an atom is computed by

$$F_i = -\nabla_i V(\{r_i\}). \tag{2.28}$$

The work done, W, to move an atom from point a to point b is

$$W_{ab} = \int_a^b F_i \, \mathrm{d}s_i, \tag{2.29}$$

where s is the displacement along from a to b [39].

2.4.1 Molecular Dynamics

The dynamics of a system are evolved in discrete time steps with the interaction between the atoms being governed by interatomic potentials. Thus, the trajectories of the atoms are obtained from evolving the equations of motion with time. Dynamics is possible using forces obtained either from molecular mechanics (MM) force fields or from quantum mechanical calculations.

To perform dynamics, Newton's second law of motion is numerically integrated with respect to time to obtain the positions. The positions and velocity can be obtained from the *velocity Verlet* algorithm [40]. An outline of the method is detailed. The objective is to obtain the new positions of the atoms from the forces that act upon them. Let r_n be the positions at step n, such that the time is $t_n = nh$ and $r_n = r(t_n)$, where h is the time step. The central difference formulas, obtained from Taylor expansions of r_{n+1} and r_{n-1}, allow for approximations to the velocity, $\dot{r}$, and acceleration, $\ddot{r}$, which are

$$\dot{r}_n \approx \frac{r_{n+1} - r_{n-1}}{2h}, \tag{2.30}$$

$$\ddot{r}_n \approx \frac{r_{n+1} - 2r_n + r_{n-1}}{h^2}. \tag{2.31}$$

Treating the approximation of $\ddot{r}_n$ as an equality and substituting $F_n = m\ddot{r}_n$ gives the position of the atom in the next time step to first order as

$$r_{n+1} = 2r_n - r_{n-1} + h^2 \frac{F_n}{m}, \tag{2.32}$$

which is the Verlet algorithm. The velocities, v_n, to first order, can be obtained by treating $\dot{r}_n$ as an equality, which is given by

$$v_n = \frac{r_{n+1} - r_{n-1}}{2h}. \tag{2.33}$$

More accurate estimates of the velocity, compared to the Verlet equations, can be obtained. Rearrangement and substitution of v_n into r_{n+1}, and the velocity for the next time step, v_{n+1}, can be shown to be [41]

$$r_{n+1} = r_n + hv_n + \frac{h^2}{2}\frac{F_n}{m}, \tag{2.34}$$

$$v_{n+1} = v_n + \frac{h}{2m}(F_{n+1} + F_n). \tag{2.35}$$

These are known as the velocity Verlet equations. The velocity Verlet equations provide a simple method to integrate the equations of motion. Due to integration errors the energy of the system tends to diverge. Higher order algorithms are good at conserving energy for a few time steps; however, the energy drifts over long timescales. The energy over long timescales tend to drift less in Verlet based algorithms [41]. Time reversibility of the Verlet based algorithm also consolidates the concept of energy conversation. A true Hamiltonian based dynamical system will conserve the occupied volume in phase space over time. A non-time reversible algorithm would result in a change in this volume and thus a change in energy. The velocity Verlet equations approaches the true volume conserving Hamiltonian in the limit of $h \to 0$ [41]. Macroscopic thermodynamic properties can be determined if the system obeys the ergodic hypotheses, which states that all microstates are equally probable. Thus, the time averaged property in the limit of infinite time will tend and equal to an ensemble average [41].

2.4.2 Interatomic Potentials

Interatomic potentials aim to capture the behaviour of an interacting system of atoms. The potential typically incorporates various parameters that need to be adjusted in order to best describe the system. These empirical parameters are either fitted to the results of experimental data or *ab initio* calculations [42]. Therefore, interatomic potentials are approximations. Depending on which parameters and reference configurations are used, they can often describe certain properties more accurately than others.

In MM the atoms are considered as a whole, such that the nucleus and electrons are considered as one particle. The energy is related to the geometry, which is modified as the atoms move from their equilibrium lengths and angles. The description in which these atoms move is represented by the interatomic potential, V. The potential can be decomposed into a combination of n-body interactions, which can be written as

$$\begin{aligned} V(\{r_i\}) = \sum_{\mathrm{i}} V_1(r_i) + \sum_{\substack{i,j \\ i<j}} V_2(r_i, r_j) + \sum_{\substack{i,j,k \\ i<j<k}} V_3(r_i, r_j, r_k) \\ + \ldots + \sum_{\substack{i,\ldots,m \\ i<\ldots<m}} V_m(r_i, \ldots, r_m) + \ldots, \end{aligned} \tag{2.36}$$

where $\{r_i\}$ is the set of all positions; the r subscripts denote the atom index; V_1 is the one-body term which can describe an external force applied to the system; V_2 is the two-body term which can describe the interaction of an atom pair at a distance; V_3 is the three-body term and can include angle dependency between atoms; and V_m is a many-body term, where m is the number of atoms [43].

Interatomic potentials are atomic-species dependent and can be physical-state dependent. Potentials are often fitted to experimental measurements or more accurate QM-based energy calculations such as DFT. The computational cost of MM is significantly cheaper than say DFT. This makes MM a desirable alternative to quantum mechanical simulations. As a result of its cheaper computational cost, MM allows for simulations of much larger length scales and timescales compared to QM. Potentials generally tend towards zero at an infinite range. Thus in practice, potentials are truncated in range to reduce computation cost, often referred to as the *cutoff distance.*

While potentials are made to be as generic as possible, they are limited to the data they were fitted on. Thus, potentials are not simply transferable to other systems which are beyond their design [44]. Therefore, care must be taken when applying the potential to a previously untested system, such as comparison of the potential with electronic-based calculations. While configurational energies and quantitative values of material properties may no longer be accurate, qualitative descriptions may still be possible.

Pair potentials, i.e. two-body potentials, are relatively simple and are commonly a function of the separation length between atom pairs. An example of these potentials is the Lennard-Jones (LJ) potential. Bond angles can be introduced to form two- and three-body potentials, such as the Stillinger-Weber (SW) potential [42]. Bond order potentials attempt to describe multiple bonding states of an atom, where the strength of a bond is affected by the bonding environment. An example of this potential is the Tersoff potential [45]. This potential includes a many-body interaction term via the bond-order term.

These potentials typically consider first neighbour interactions, with their bonding environment determined with a fixed interaction range. While the potentials are able to describe properties near equilibrium, issues arise for more complicated interactions such as bond breaking [46, 47]. This can be improved upon by increasing the range of the potential and introducing screening functions which screen the strength of an interaction if there are other atoms within the interaction distance of a particular atom pair. An example of a potential improved by addressing the screening effect is the screened Tersoff potential [47].

2.4.3 Dynamics at Finite Temperature

Many real-world situations occur at a finite temperature such that the system is at a temperature that matches its surroundings. In order to simulate a system in thermal equilibrium a *thermostat* is required. This allows for the system to exchange energy with a *heat bath* and once the system has equilibrated it would allow for correct sampling of the canonical ensemble. The Langevin thermostat was used here to moderate the temperature.

Newtonian molecular dynamics (MD) simulations conserve: total energy, E; number of particles, N; and volume, V. These simulations are ensemble averages in the microcanonical ensemble, or NVE ensemble. To perform MD in different ensembles, two major methods are available; one is to mix MD with Monte Carlo moves, and the other is to reformulate the Lagrangian equations of motion [41]. Andersen first introduced a modified Lagrangian method, which allowed constant pressure simulations [48]. Here, constant temperature is required. A statistical view of constant temperature is achieved by thermal contact of the system with a large heat bath. This is the canonical ensemble, or the NVT ensemble [41].

Langevin Dynamics

The Langevin model uses an addition friction term, γ, and random force, ϕ, term to simulate the simple heat bath. Langevin dynamics is governed by

$$m\ddot{r}(t) = -\nabla V(r(t)) - \gamma m\dot{r}(t) + \phi(t), \tag{2.37}$$

where $-\nabla V(r(t))$ is the original force term [49]. γ is also known as the collection parameter, or damping constant. ϕ is a stationary Gaussian process with a mean, $\langle r(t)\rangle$, and variance, $\langle r(t)r(t')^T\rangle$, defined as

$$\langle r(t)\rangle = 0, \tag{2.38}$$

$$\langle r(t)r(t')^T\rangle = 2m\gamma k_\mathrm{B}TM\delta(t-t'), \tag{2.39}$$

where k_B is the Boltzmann constant, T is the target temperature, and δ is the Dirac delta function [49]. The addition of the friction term dampens the motion while the random force term ensures stochastic excitation to the kinetic energy. These excitations are time-dependent, as well as uncorrelated from each particle and each time step [50].

The Langevin model can be implemented via the Verlet algorithm [49], which retains the benefits and simplicity of the Verlet algorithm while providing a description of the canonical ensemble. The trajectories from Langevin dynamics can represent the canonical ensemble since the trajectories are ergodic. A system is ergodic if the trajectory averages are the same as the phase space averages on the energy surface [51].

2.5 Multiscale Mechanics

The scale of components in production run from tens of nanometres to tens of metres. Current computational techniques, along with current computational power, limit the size of the problem addressable in design and testing, as shown in Fig. 2.3. Therefore, the size of the problem in space and time determines the level of accuracy achievable and vice versa.

Continuum models work on the basis of solving for displacement fields subject to boundary conditions. Due to the complex stability of a fracture system, such models need to also incorporate consideration of a path [14], which relies on empirical data. This can be attributed to the lack of detail

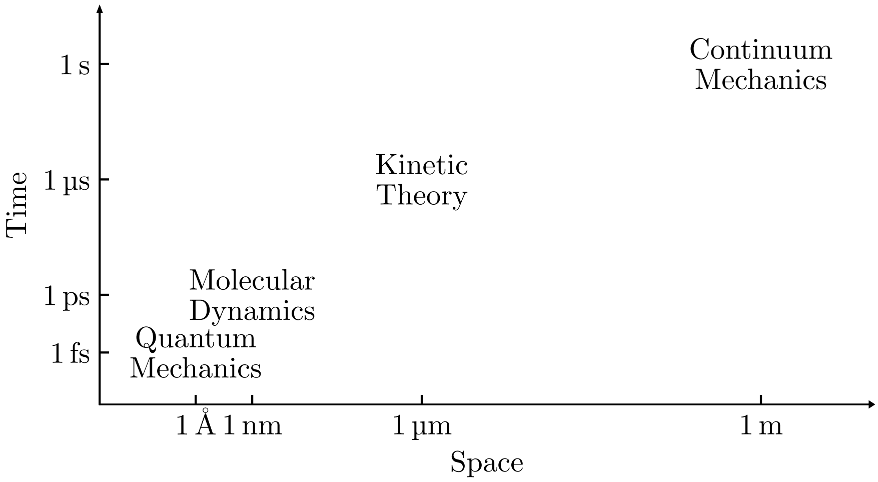

Figure 2.3: Physical descriptions with respect to the length scales and timescales which are accessible via modelling techniques [11].

at the crack tip as the instabilities occur within this region. Without this information the models lack accuracy and therefore provide only a qualitative description [52]. Due to the discrete nature of materials, a discrete representation is required to achieve better quantitative and qualitative descriptions.

The use of MD relies on a system with many bodies as the interatomic potentials that are used to describe the system describe the average interaction between atoms. While MD simulations rely on statistical techniques to average over small fluctuations to produce properties of interest [41], the details of crack propagation are located where the average description of interatomic potential breaks down, i.e. outside of the harmonic regime. For example the stress near a crack tip diverges, as shown in Fig. 2.4. MD simulations model the discrete nature of materials as opposed to a continuum description used in continuum simulations; however, MD is still not able to accurately describe the different chemical reactions near the crack tip. Furthermore, MD is only applicable to small systems in comparison to the system sizes available for continuum models. Attempts have been made to produce an environment-dependent interatomic potential for silicon [53]. However, the increased complexity makes it computationally more expensive to calculate and it has limited transferability beyond where it was fitted. Recent attempts have used machine learning techniques to produce a potential for silicon which used DFT calculations as the training data. This approach enabled computation of properties which would be relatively expensive with first-principles methods [54].

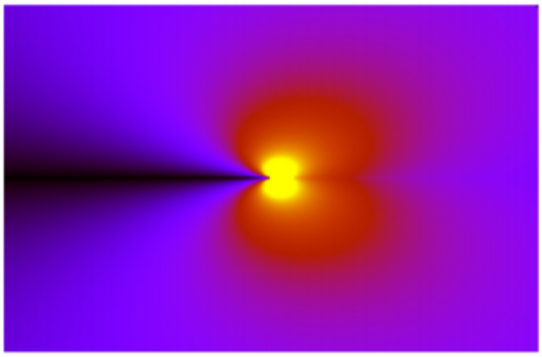

Figure 2.4: Graphical representation of the maximum principal stress around a crack tip of a system under uniaxial tension [55]. Yellow areas are the most stressed and black areas are the least stressed.

Fracture simulations can benefit from the use of QM. However, the computational costs associated with approximate QM solutions, such as DFT, are high. This limits simulations times to the order of picoseconds and system sizes to the order of hundreds of atoms.

Hybrid methods, or multiscale methods, combine different modelling techniques to capture features at different scales, which would otherwise not be feasible with the use of a single scale method. Typically, a finer scale model is combined with a coarser scale model. The finer scale model allows for detail to be retained and captured at the points of interest, and the coarser scale model is used in the remaining areas where a less detailed method is sufficient for capturing the other features. Some examples of combinations of multiscale techniques include quantum-molecular [55] and molecular-continuum [56]. This allows for larger scale simulations for a reduced computational cost compared to the same simulation with the use of only the higher accuracy method. In practice, it enables a simulation of much larger length scales than what would be possible for high accuracy single scale methods.

In general, there are two systematic methods for multiscale modelling, and they are simultaneous modelling and hierarchical modelling. Simultaneous modelling requires the use of models at different length scales coupled in real time. Typically, forces and displacements are computed on-the-fly to link the scales. For example, atomic motion computed within a quantum mechanical region is compatible with the atomic motion computed in the molecular mechanical region. Thus, information regarding the dynamics of the system can be obtained [55]. In hierarchical modelling the finer scale model is used to parametrise the coarser scale model and vice versa [57]. This can be achieved in different ways. For example, information can be passed from microscale models to macroscales models to take microscale phenomena and observe macroscale behaviour [58, 59]. Information can also be passed in the opposite direction, for example coarse gains models can help generate finer scale models to improve accuracy within domains where more detail is required [60] or where the result exceeds an error threshold [61]. The atomistic fracture simulations performed here can somewhat be considered as part of a hierarchical model as they use continuum fracture theory to set the boundary region for the atomistic domain, and thus information obtained from the simulation could be mapped into a continuum model. Multiscale modelling is key for crack defects as the chemistry near the crack tip requires a quantum level of precision with a system that is large enough to model the dynamics of a crack tip across the material for a significant time [62–65].

Several issues arise when coupling modelling techniques of two different length scales [11, 66]. In the process of changing length scales, information can be lost and the underlying physical descriptions changes, which reduces the accuracy of the calculation. The need to quantify this loss becomes increasingly important in order to validate the calculation. Fluctuations and uncertainties can naturally occur in the systems modelled with one technique. The combination of two techniques introduces further errors. The uncertainty of a calculation can arise from various sources. During a simulation, model uncertainty and input uncertainty are inherent. Model uncertainty is the inadequacy to capture the true underlying physics, whether that is due to approximations in the physics or due to natural random fluctuations. Input uncertainty is the lack of available knowledge regarding the precise details of every degree of freedom. Computer simulations also suffer from numerical errors, for example: the truncation of an infinite series, the discretisation of continuous functions, and the floating point representation of real numbers [67].

2.6 Geometry Optimisation

The energy minimisation of the positions as well as optimisation of the size and shape of the encompassing cell were performed using a few different methods.

Various optimisations methods exist. Methods such as damped MD [68] and fast inertial relaxation engine (FIRE) modify the equations of motion. Another class of optimisation methods, often referred to as *descent methods*, include methods such as *steepest-descent*, *conjugate gradient* and *Newton's method* [69]. Here, geometry optimisations were performed with, FIRE, Broyden–Fletcher–Goldfarb–Shanno (BFGS), limited-memory Broyden–Fletcher–Goldfarb–Shanno (LBFGS), and the Interior-Point Primal-Dual Newton method; an overview of the methods are detailed.

2.6.1 Steepest Decent Method

The objective of optimisation algorithms are to find the solutions to, or minimise, a function $f(x)$. The solutions to f are of the form $f(x^*) = 0$, where x^* is a solution. The *line search* method is an algorithm that for each iteration it moves along x with direction p to find a new x with a corresponding lower function value. An iteration of a line search method is given by

$$x_{k+1} = x_k + \alpha_k p_k, \tag{2.40}$$

where α_k is the step length, p_k is the search direction, and k is the current iterate [70].

The *steepest decent* method, or *gradient descent* method, is conceptually a relatively simple optimisation algorithm. The search direction is given by

$$p_k = -\nabla f_k, \tag{2.41}$$

where ∇f_k is the gradient of f_k. The descent direction of $-\nabla f_k$ is an intuitive direction to move in as it is the one along f which decreases most rapidly. While this is intuitive, the direction can lead to a slow rate of convergence [70].

2.6.2 Fast Inertial Relaxation Engine Method

FIRE is based on the idea of letting inertia decide the direction in which to descend [71]. It follows a modified Newton's equation of motion of the form

$$ma(t) = F(t) - m\gamma(t)|v(t)|\big[\hat{v}(t) - \hat{F}(t)\big], \tag{2.42}$$

where the hat denotes a unit vector. In particular, the descent is governed by γ which modifies the acceleration towards a direction that is steeper downhill, as long as the power, $P(t) = F(t) \cdot v(t)$, is positive. A similar algorithm used in the Verlet formulation is used to find the minimum. FIRE performs better than the conjugate gradient method, and similar to LBFGS, for some problems [71].

2.6.3 Broyden–Fletcher–Goldfarb–Shanno Method

The BFGS method is rooted in Newton's method for optimisation; specifically, it is referred to as a *quasi-Newton* method as it only requires the gradient of the objective function for each step [70]. The objective is to minimise a function, $f(x)$. Newton's method for optimisation, is an iterative scheme that uses

$$x_{k+1} = x_k - \alpha H_k^{-1} \nabla f_k \tag{2.43}$$

to find the minimum, where H is the Hessian, α is step length, and when $\alpha = 1$ it forms the Newton scheme. The path search direction, p_k, is

$$p_k = -H_k^{-1} \nabla f_k. \tag{2.44}$$

Let $H_k^{-1} = B_k$. The BFGS method approximates the next Hessian by accounting for the curvature measured during the most recent step.

The Hessian at the next iteration is approximated by

$$B_{k+1} = (I - \rho_k s_k y_k^T) B_k (I - \rho_k y_k s_k^T) + \rho_k s_k s_k^T, \tag{2.45}$$

where

$$s_k = x_{k+1} - x_k, \tag{2.46}$$

$$y_k = \nabla f_{k+1} - \nabla f_k, \tag{2.47}$$

$$\rho_k = \frac{1}{y_k^T s_k}, \tag{2.48}$$

and I is the identity matrix [70]. The first approximation, B_0, is computed by whichever means, such as finite differences or simply set to be the identity matrix. An overview of each iteration is detailed. First B_0 is computed, to then compute p_0 in Eq. 2.44. Then it is possible to compute x_1 using Eq. 2.43. The x_0 and x_1 are then used to compute s_0, y_0, and thus ρ_0 of Eqs. 2.46 to 2.48. These are fed into the approximation of the Hessian B_1 using Eq. 2.45. Then the next search direction, p_1 can be calculated using Eq. 2.44. The iteration is repeated until converged.

The steepest decent method is simply Eq. 2.43 without the Hessian, i.e. $x_{k+1} = x_k - \alpha \nabla f_k$. The BFGS method performs better than steepest decent methods and is also known to have effective self-correcting properties if the Wolfe line search conditions are met [70].

2.6.4 Limited-Memory Broyden–Fletcher–Goldfarb–Shanno Method

For large scale simulations, where the Hessian of the BFGS method can not be reasonably computed, the LBFGS method can be used. This memory efficient method only stores m number of vectors of length n to represent the full Hessian of $n \times n$, instead of storing the entire Hessian. Only the most recent information regarding the curvature of the previous iterations are stored, information from earlier iterations are discarded [70].

Let $V_k = I - \rho_k y_k s_k^T$. In the LBFGS implementation B_k relies on the fact that B_k can be further estimated via

$$\begin{aligned}B_k = &(V_{k-1}^T \cdots V_{k-m}^T) B_k^0 (V_{k-m} \cdots V_{k-1}) \\ &+ \rho_{k-m} (V_{k-1}^T \cdots V_{k-m+1}^T) s_{k-m} s_{k-m}^T (V_{k-m+1} \cdots V_{k-1}) \\ &+ \rho_{k-m+1} (V_{k-1}^T \cdots V_{k-m+2}^T) s_{k-m+1} s_{k-m+1}^T (V_{k-m+2} \cdots V_{k-1}) \\ &+ \cdots \\ &+ \rho_{k-1} s_{k-1} s_{k-1}^T,\end{aligned} \tag{2.49}$$

where H_k^0 is the initial matrix and it is allowed to vary between each iteration. In practice, a recursive algorithm is used to directly compute the product $B_k \nabla f_k$, which is used to compute the path direction, p_k. The iterative algorithm similar to the BFGS method is used. The LBFGS method tends to be less robust for small m, though m is dependent on the system [70].

2.6.5 Interior-Point Primal-Dual Newton Method

The aim is to minimise the energy of the system with constraints, e.g. such that certain separation distances between particular atoms are held to a prescribed length, particularly the pair(s) of atoms directly ahead of the crack tip.

Here, the interior-point primal-dual Newton method for nonlinear optimisation is used [70]. An outline of the method and its iteration step is described.

A general form of a nonlinear minimisation problem is

$$\text{minimise } f(x) \tag{2.50}$$

$$\text{subject to } g_i(x) \leqslant \text{ or } \geqslant 0 \quad \text{for } i \in \{1, \ldots, m\}, \tag{2.51}$$

$$h_j(x) = 0 \qquad \text{for } j \in \{1, \ldots, p\}, \tag{2.52}$$

where $f(x)$ is the objective function to minimise, $g_i(x)$ are known as the inequality constraints, $h_j(x)$ are the equality constraints, with a total of m inequality constraints, and and with a total of p equality constraints.

For a constraint to be within a particular tolerance an inequality constraint is used, compared to a constraint with an exact value for which an equality constraint would be used. For simplicity, the inequality constraints can be made into equality constraints through use of *slack variables*, s, such that $c(x) \leqslant$ or $\geqslant 0$ becomes $c(x) - s = 0$, with $s \geqslant 0$. The objective function can be modified to use a logarithmic barrier function, which removes the requirement for $s \geqslant 0$ as the barrier term prevents s from reaching zero or even being too close to zero.

The nonlinear minimisation problem is now of the form

$$\begin{aligned} &\text{minimise } f(x) - \mu \sum_{i=1}^{m} \log s_i && (2.53) \\ &\text{subject to } c_i(x) - s_i = 0 \qquad \text{for } i \in \{1, \ldots, m\}, && (2.54) \end{aligned}$$

where μ is the barrier coefficient, $c_i(x) - s_i$ are the new constraint functions, and s_i are the individual components of s. Define a Lagrangian function of the above problem as

$$\mathcal{L}(x, \lambda) = f(x) - \mu \sum_{i=1}^{m} \log s_i - \lambda\bigl(c(x) - s\bigr), \tag{2.55}$$

where λ is the Lagrange multiplier.

For a solution (x^*, λ^*) to be a local optimum, the solution must satisfy the Karush–Kuhn–Tucker (KKT) conditions [70] which are:

$$\begin{aligned} \text{stationarity:} \quad & \nabla_x \mathcal{L}(x^*, \lambda^*) = 0, && (2.56) \\ \text{primal feasibility:} \quad & c_i(x^*) \leqslant 0 \quad \text{for } i \in \{1, \ldots, m\}, && (2.57) \\ \text{dual feasibility:} \quad & \lambda_i \geqslant 0 \quad \text{for } i \in \{1, \ldots, m\}, && (2.58) \\ \text{complementary slackness:} \quad & \lambda_i^* c_i(x^*) = 0 \quad \text{for } i \in \{1, \ldots, m\}, && (2.59) \end{aligned}$$

where *stationarity* refers to the stationarity point of the problem in x; *primal feasibility* is the condition to meet to solve the primal problem, i.e. the original optimisation problem subject to the constraints, Eq. 2.53 and Eq. 2.54 respectively; *dual feasibility* is the condition to meet to solve the dual problem, which are Eq. 2.56 and Eq. 2.58, formulated through formation of the Lagrangian and the Lagrange multiplier λ [72]; and *complementary slackness* refers to the slack available between the primal constraint, c_i, and the dual constraint, λ_i, such that one is active and the other is zero or both are zero [70, 72].

The derivatives of the Lagrangian at the optimum point are zero, and they are written as

$$
\begin{aligned}
\nabla_x = & \nabla f(x) - A(x)\lambda = 0, & (2.60)\\
\nabla_s = & \quad -\mu S^{-1}e + \lambda = 0, & (2.61)\\
\nabla_\lambda = & \qquad c(x) - s = 0, & (2.62)
\end{aligned}
$$

where $A(x)$ is the Jacobian matrix of the constraint function, with $A_{ij} = \partial c_i / \partial x_j$; S is a diagonal matrix whose diagonal entries are the components of s; and let $e = (1, ..., 1)^T$ which has a length equal to the number of constraints.

The roots of the Lagrangian are calculated by the iterative approach of Newton's method. For a twice differentiable function, $f(x)$, to find the roots, $\nabla f(x^*) = 0$, each step of the iteration is of the form

$$x_{n+1} = x_n - \nabla^2 f^{-1}(x_n)\nabla f(x_n), \tag{2.63}$$

where $\nabla^2 f(x_n)$ is the Hessian matrix of x_n. Computing the inverse of the Hessian is a computational expensive operation. A less intensive method is to compute $\Delta x = x_{n+1} - x_n$, by solving the linear system

$$\nabla^2 f(x_n)\Delta x = -\nabla f(x_n). \tag{2.64}$$

Thus for the nonlinear system, in Eqs. 2.60 to 2.62, applying Newton's method leads to

$$\begin{bmatrix} \nabla_{xx}\mathcal{L} & 0 & -A^T(x) \\ 0 & \Omega & -I \\ A(x) & I & 0 \end{bmatrix} \begin{bmatrix} p_x \\ p_s \\ p_\lambda \end{bmatrix} = - \begin{bmatrix} \nabla f(x) - A^T(x)\lambda \\ -\mu S^{-1}e + \lambda \\ c(x) - s \end{bmatrix} \tag{2.65}$$

where p is the step direction, I is the identity matrix, $\Omega = S^{-1}\Lambda$, and Λ is a diagonal matrix whose diagonal entries are the components of λ. The points of the next step can then be calculated using

$$
\begin{aligned}
x_{n+1} &= x + \alpha_s^{\max} p_x, & (2.66)\\
s_{n+1} &= s + \alpha_s^{\max} p_s, & (2.67)\\
\lambda_{n+1} &= \lambda + \alpha_\lambda^{\max} p_\lambda, & (2.68)
\end{aligned}
$$

where

$$\alpha_s^{\max} = \max\{\alpha \in (0,1] : s + \alpha p_s \geqslant (1-\tau)s\,\}, \tag{2.69}$$

$$\alpha_\lambda^{\max} = \max\{\alpha \in (0,1] : \lambda + \alpha p_\lambda \geqslant (1-\tau)\lambda\}, \tag{2.70}$$

where $\tau \in (0,1)$. The formulae for α are called the *fraction to the boundary rule* [70].

Newton's method on the Lagrangian forms the basis of the interior-point primal-dual Newton method. Further information on this method can be found in Numerical Optimization [70]. The implementation of this method used here is via the *Optim* package [73].

2.7 Surface Energy

The surface energy, γ, is the amount of energy required to build, or cut, a surface from a bulk material per unit area. It is the energy required to break the intermolecular bonds between atoms. This makes surfaces intrinsically less energetically favourable, and thus an input of energy from an external force is required for them to be created. The surface energy of a material is quoted as if it was situated in a vacuum. A surface can oxidise or react with the air, causing the energy to change via the addition of extra atoms or subtraction of existing atoms. These surface energies are altered via the processes of passivation or adsorption. Surface atoms can also positionally rearrange, which alters the bonding between the atoms. This is known as surface reconstruction.

For a particular surface of a crystalline solid, the surface energy can be calculated by comparing the energies of the bulk material and a slab of the material, in which the slab of material exposes that particular surface. Examples of the systems used are shown in Fig. 2.5. The bulk cell is generated by replicating the unit cell of the crystal. It is possible to compare systems with different number of atoms. The energy of the bulk would need to be scaled by the number of atoms in the bulk and the number of atoms in the slab system, to give an energy per atom comparison. The atomic and cell's degrees of freedom undergo a geometry optimisation. To generate the slab system, the bulk system is duplicated and a vacuum is added in one direction on either side of the material. Periodic computational cells are used to

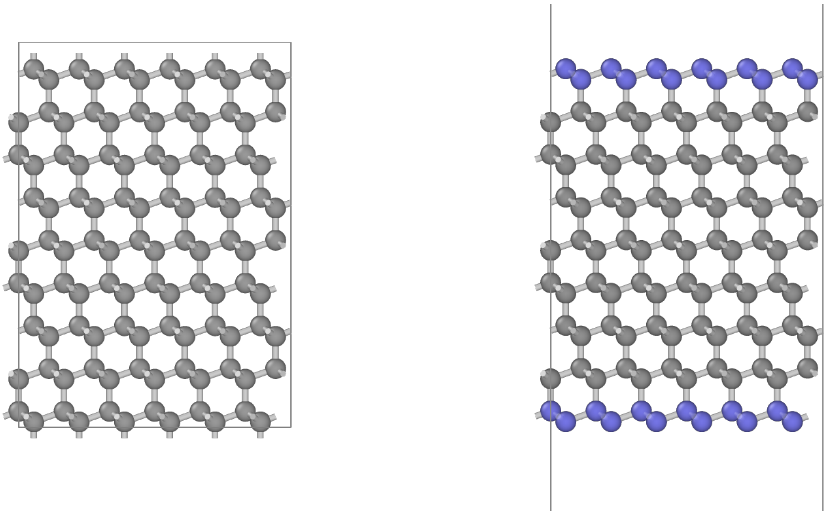

(a) (b)

Figure 2.5: For a particular surface of a crystalline solid, the surface energy can be calculated by comparing the energies of the a) bulk and b) slab systems, in which the slab system exposes that particular surface. The atoms of that surface are highlighted in blue. The box surrounding the atoms is the computational cell. For b) the box extends well away from the surfaces to implement a vacuum.

simulate larger systems. Due to the slab system having a vacuum along one direction, the size of the vacuum should be sufficient to avoid interactions with surfaces in the periodic cells.

The surface energy, γ, is calculated using

$$\gamma = \frac{E_{\text{slab}} - E_{\text{bulk}}}{2A} \tag{2.71}$$

where A is the exposed surface area, E_{bulk} is the energy of the bulk system and E_{slab} is the energy of the slab system.

2.8 Linear Elasticity

The theory of elasticity describes the relationship between the displacements, strains, and stresses of a material; it links deformations to applied loads and internal forces, and vice versa. Note that tensor notation [74] is used within this section.

Stresses represent the internal resistance due to external forces. Strains represent the change in the material's dimensions compared to its original length [75].

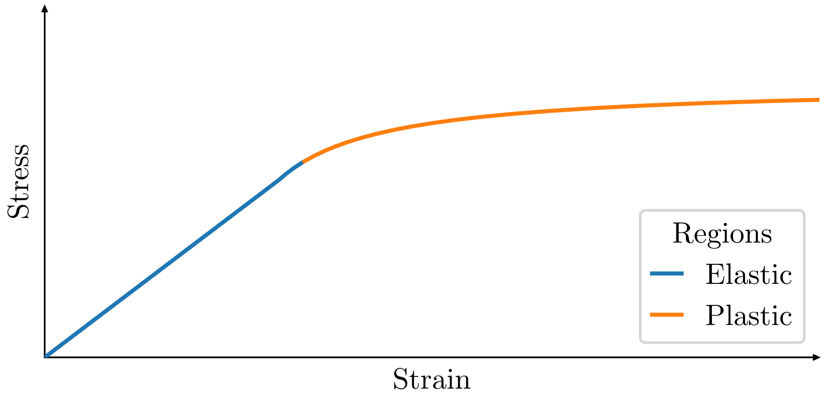

Figure 2.6: Schematic of a stress-strain curve. Some materials will undergo a linear elastic deformation phase and then undergo a plastic deformation phase. Brittle materials break near the elastic/plastic region and experience little to no plastic deformation.

For small stresses a material can be considered as *elastic*, such that it can restore itself to its original state if the external force is no longer applied. In this regime, if the relationship between stress and strain is linear it is known as *linear elasticity*. For large stresses the material can undergo *plastic* deformation, i.e. irreversible deformation, and then fracture; this relationship is non-linear. For brittle materials there is little to no plastic deformation and the material fractures beyond a certain stress. A typical stress-strain curve is shown in Fig. 2.6, with the different regimes labelled.

A force, ΔF, acting on an area, ΔA, can be related as the traction vector, T, which is defined as

$$\lim_{\Delta A_n \to 0} \frac{\Delta F_n}{\Delta A_n} = \frac{\mathrm{d}F_n}{\mathrm{d}A_n} = T_n, \tag{2.72}$$

where n is the unit normal to the area segment ΔA_n. T_n is also known as the stress vector [76]. The traction in terms of Cartesian components is

$$T_i = \sigma_{ij} e_j, \tag{2.73}$$

where e_j is the unit normal, σ_{ij} is the stress component of the Cauchy stress tensor. The first subscript i denotes the face on which T_i acts and the second subscript j denotes the direction in which the stress acts. The strain tensor in Cartesian components, ϵ_{ij}, is

$$\epsilon_{ij} = \frac{1}{2}\left(\frac{\partial u_i}{\partial x_j} + \frac{\partial u_j}{\partial x_i}\right), \tag{2.74}$$

where u are the displacements.

For a material at constant temperature and gradual loading within the linear elastic regime, stresses and strains are related by the generalised Hooke's law given by

$$\sigma = C\epsilon, \tag{2.75}$$

where σ is the stress tensor, ϵ is the strain tensor, and C is the elastic constants tensor [76]. Each component can be written as

$$\sigma_{ij} = C_{ijkl}\epsilon_{kl}. \tag{2.76}$$

The strain and stress tensors are second-order tensors of nine components each, which allows it to represent the complex possible states a material can undergo, such as compression, stretching, and shearing, in all directions. The stress tensor and the strain tensor are related by the elastic constant tensor, a fourth-order tensor. Due to the symmetry of C and a continuous strain energy density [76], the number of components can be reduced, from 81 components to 36 components, comprised of 21 independent components, leading to

$$\begin{bmatrix} \sigma_{11} \\ \sigma_{22} \\ \sigma_{33} \\ \sigma_{23} \\ \sigma_{13} \\ \sigma_{12} \end{bmatrix} = \begin{bmatrix} C_{1111} & C_{1122} & C_{1133} & C_{1123} & C_{1113} & C_{1112} \\ & C_{2222} & C_{2233} & C_{2223} & C_{2213} & C_{2212} \\ & & C_{3333} & C_{3323} & C_{3313} & C_{3312} \\ & & & C_{2323} & C_{2313} & C_{2312} \\ & & & & C_{1313} & C_{1312} \\ & & & & & C_{1212} \end{bmatrix} \begin{bmatrix} \epsilon_{11} \\ \epsilon_{22} \\ \epsilon_{33} \\ 2\epsilon_{23} \\ 2\epsilon_{13} \\ 2\epsilon_{12} \end{bmatrix}. \tag{2.77}$$

The indices of σ and ϵ are written in Voigt notation order, i.e. Voigt notation without the reduction of indices [74].

A material under tensile strain in one direction will compress in the other directions. This phenomenon is the *Poisson effect.* The ratio of a strain in an axial direction and a strain in the transversal direction is the *Poisson's* *ratio*, given by

$$\nu_{ij} = -\frac{\epsilon_{jj}}{\epsilon_{ii}}, \tag{2.78}$$

where i and j can be any direction. In other words, for an applied strain in i there is a response in j. Under an applied stress the material naturally resists deformation. For a uniaxial stress the Young's modulus, E, is a measure of this stiffness, defined by

$$E_i = \frac{\sigma_{ii}}{\epsilon_{ii}}, \tag{2.79}$$

where i can be any direction [76].

2.9 Brittle Fracture

Many causes can lead to the failure of a material. Fracture is one of the fundamental mechanisms through which a material responds as a result of stress on the system. Fracture mechanisms are extremely complicated, with many considerations to account for when modelling. The initiation of fracture is less amenable to systematic analysis. On the other hand, systematic study of fracture propagation is possible [14]. Here, only properties of brittle fracture propagation are examined.

Fracture is fundamentally driven by long range stress fields with complex electronic interactions occurring near the crack tip. Brittle fracture has its foundations in continuum techniques. Recent advancements have progressed fracture methods to the atomistic scale in order to include electronic considerations of the bonds and atoms around the crack tip.

Continuum fracture theory was predominantly progressed by Inglis, Griffith and Irwin: Inglis showed that near an elliptical cavity the local stress can rise to levels much higher than the applied stress; Griffith considered the system with reversible thermodynamical processes; and Irwin formulated the solutions for the stress and the displacements fields [6, 14].

2.9.1 Griffith Thermodynamic Energy Balance

The energy balance of a crack system allows the comparison between the energy released and the energy required to generate surfaces.

Griffith first modelled a continuum static crack as a reversible thermodynamical system. This was instrumental in understanding crack propagation.

The concept was that a crack system is always in a state which minimises the total energy, i.e. in equilibrium, and thus on the verge of extension. The formulation considers the components of energy which change during crack extension.

The total energy of the system, U, can be considered as a combination of mechanical, U_{M}, and surface, U_{S}, terms, such that

$$U = U_{\mathrm{M}} + U_{\mathrm{S}}. \tag{2.80}$$

The mechanical term can be further broken down into the potential energy of the applied load, U_{A}, and the stored elastic potential energy in the system, U_{E}. U_{S} is the free energy expended in creating new surfaces. The equilibrium condition is such that

$$\frac{dU}{dC} = 0, \tag{2.81}$$

where C is the crack interfacial area [14]. This implies that a small deviation from equilibrium would result in extension or retraction of the crack. Mechanical energy, U_{M}, decreases as crack extends, i.e. $\frac{\mathrm{d}U_{\mathrm{M}}}{\mathrm{d}C} < 0$, while the surface energy contribution, U_{S}, increases as crack extends, i.e. $\frac{\mathrm{d}U_{\mathrm{S}}}{\mathrm{d}C} > 0$. The mechanical term favours crack extension, while the surface energy term resists crack extension.

The *mechanical energy release rate*, G, is defined to be

$$G = -\frac{\mathrm{d}U_{\mathrm{M}}}{\mathrm{d}C}, \tag{2.82}$$

i.e. the loss of mechanical energy per unit area [14]. For a simple, straight crack the area can be simplified to a single dimension representing the crack extension, c. It can also be shown that the change in mechanical energy is independent of the loading configuration, and so U_{M} only depends on U_{E}. Thus, G can be considered as the strain energy release rate per unit crack length, given by

$$G = -\frac{\partial U_{\mathrm{E}}}{\partial c}. \tag{2.83}$$

The intrinsic work per unit area to separate the inter-surface forces, R_0, is

$$R_0 = +\frac{\mathrm{d}U_{\mathrm{S}}}{\mathrm{d}C}. \tag{2.84}$$

Similarly as with G, C can be reduced to c. Durpé showed that the work

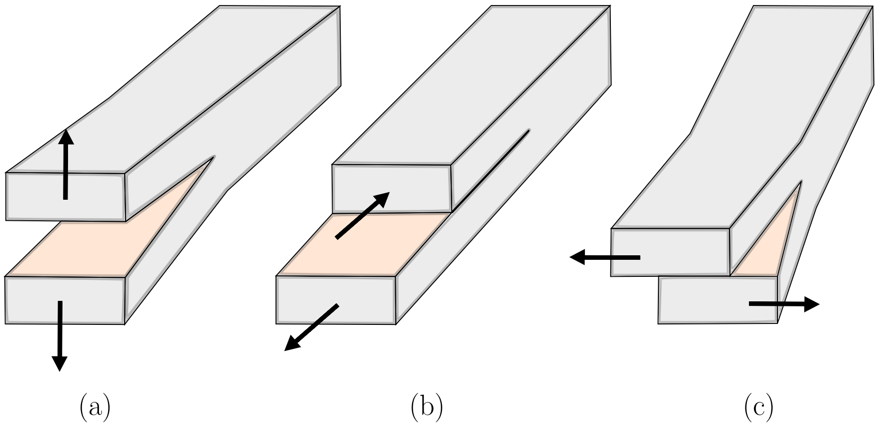
(a) (b) (c)

Figure 2.7: The three modes of fracture: a) mode I, *opening mode*; b) mode II, *sliding mode*; and c) mode III, *tearing mode* [14].

performed is twice the surface energy, given by

$$R_0 = 2\gamma, \tag{2.85}$$

where γ is the surface energy. This is similar to Griffith's intrinsic surface energy [14]. Thus, the equilibrium condition for energy balance of a crack extension can be rewritten as

$$\frac{\mathrm{d}U}{\mathrm{d}C} = \frac{\mathrm{d}U_\mathrm{M}}{\mathrm{d}C} + \frac{\mathrm{d}U_\mathrm{s}}{\mathrm{d}C}, \tag{2.86}$$

$$0 = -G_\mathrm{c} + R_0, \tag{2.87}$$

$$G_\mathrm{c} = 2\gamma, \tag{2.88}$$

where G_c is the critical mechanical energy release rate [14]. As such, for $G < G_\mathrm{c}$ the crack retracts and for $G > G_\mathrm{c}$ the crack extends.

2.9.2 Stress Intensity Factor

The stress intensity factor, K, encapsulates the magnitude of the stress within a system due to an applied load.

There are three *modes* of displacement that further extend fracture surfaces: mode I, *opening mode*, where the load is applied on either side of the crack, away from the crack; mode II, *sliding mode*, where the load is applied

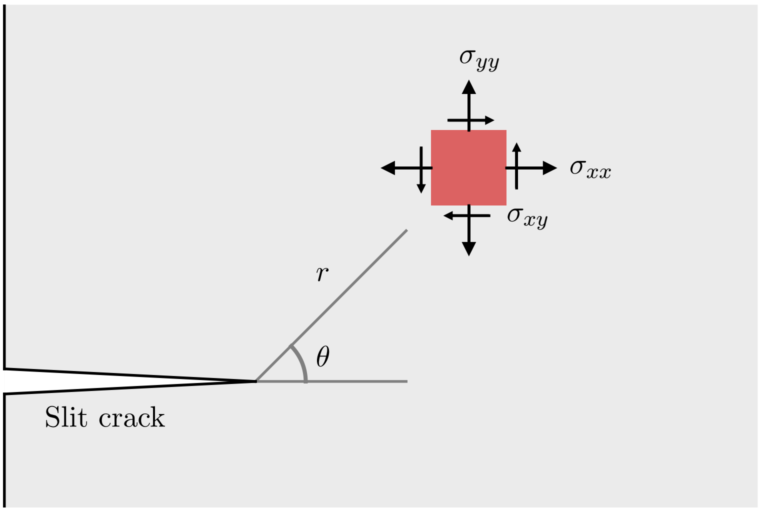

Figure 2.8: Schematic of Irwin's infinitesimal narrow slit crack geometry, with the stress, σ, components shown at position (r, θ) relative to the crack tip [14].

in opposite directions above and below the crack, with one in the direction of crack extension; and mode III, *tearing mode*, where the load is applied in opposite directions above and below the crack, perpendicular to the crack direction on the crack plane [14]. Schematics of the three modes are shown in Fig. 2.7.

For an infinitesimally narrow slit crack geometry, shown in Fig. 2.8, Irwin derived solutions for displacement and stress fields from principles of linear elasticity. The stress and displacement fields can be written as

$$\sigma_{ij} = \frac{K}{\sqrt{2\pi r}} f_{ij(\theta)}, \tag{2.89}$$

$$u_i = \frac{K}{2E}\sqrt{\frac{r}{2\pi}} f_i(\theta), \tag{2.90}$$

where σ are the Cauchy stresses, r is the distance from the crack tip, θ is the angle with respect to the crack plane, and f_{ij} are functions which depend on the type of mode loading and the geometry [14]. The stress intensity factor captures the applied loading, while the other term is dependent on relative spatial coordinates. The $\sqrt{r}$ term in Irwin's solutions implies that there is a singularity at the crack tip, as the initial geometry requires an infinitesimally small, and thus perfectly sharp, crack tip. To avoid this, and to match the boundary conditions, higher order terms are required. As such, the stress field does not necessarily hold for small or large r [14]. The sharp stress field near the crack tip can be mitigated through non-linear or inelastic behaviour around the crack tip. The solutions still maintain an adequate description provided the inelastic region is small compared to the length scales of the system and crack length.

The *fracture toughness*, K_c, is the critical stress intensity factor for which the crack propagates [14]. The Irwin fracture criterion is that for $K > K_\mathrm{c}$ the crack advances and for $K < K_\mathrm{c}$ the crack retreats.

By considering infinitesimal crack extension, Irwin showed that the integration of the strain energy release per unit crack extension can be shown to relate K and G as

$$G = \frac{K_\mathrm{I}^2}{E'} + \frac{K_\mathrm{II}^2}{E'} + \frac{K_\mathrm{III}^2(1+\nu)}{E}, \tag{2.91}$$

where E' is the effective Young's modulus [14]. Throughout this work only mode I cracks were investigated, so there are no loads applied to form mode II and mode III cracks. So K_I will now simply be K and G can be simplified to

$$G = \frac{K^2}{E'}. \tag{2.92}$$

The effective Young's modulus is different depending on the thickness of the system. For a thick plate *plane strain* applies, and for a thin plate *plane stress* applies. The effective Young's modulus is given by

$$E' = \begin{cases} E\left(1-\nu^2\right)^{-1} & \text{plane strain,} \\ E & \text{plane stress,} \end{cases} \tag{2.93}$$

where ν is the Poisson's ratio [14].

Thus, the critical stress intensity factor can be related to the surface energy of the material as

$$K_\mathrm{c} = \sqrt{G_\mathrm{c}E'}, \tag{2.94}$$

$$= \sqrt{2\gamma E'}. \tag{2.95}$$

This is particular useful as K_c can be estimated from the surface energy of a material, without any actual fracture simulations.

2.9.3 Mode I Fracture

Mode I fracture for the plain strain case was analysed throughout this work. Consider a geometry where the length in one dimension, z, is much greater than the other two dimensions, x and y, then an approximation to the strain tensor is

$$\epsilon = \begin{bmatrix} \epsilon_{11} & \epsilon_{12} & 0 \\ \epsilon_{21} & \epsilon_{22} & 0 \\ 0 & 0 & 0 \end{bmatrix} . \tag{2.96}$$

The components ϵ_{31}, ϵ_{32}, and ϵ_{33}, of the longer dimension are constrained by the nearby material and so are negligible compared to the cross-sectional strains in the other dimensions. Eq. 2.96 is considered as a plane strain tensor. For 2D materials, the z direction does not exist, and so there is no response in that direction. Thus, the plane strain case still applies.

The displacement solutions for a mode I system are

$$u = \begin{bmatrix} u_x \\ u_y \end{bmatrix} = \frac{K}{2E}\left(\frac{r}{2\pi}\right)^{\frac{1}{2}}(1+\nu)\begin{bmatrix} (2\kappa-1)\cos\left(\frac{\theta}{2}\right) - \cos\left(\frac{3\theta}{2}\right) \\ (2\kappa+1)\sin\left(\frac{\theta}{2}\right) - \sin\left(\frac{3\theta}{2}\right) \end{bmatrix} , \tag{2.97}$$

where $\kappa = 3 - 4\nu$ and applies for plane strain situations, K is the stress intensity factor, E is the Young's Modulus, r is the radial distance from the crack tip, ν is Poisson's ratio, and θ is the angle from measured from the normal vector of the crack front plane [14]. These displacements will often be referred to as the continuum linear elastic (CLE) displacements.

2.10 Materials

Fracture can occur in a vast number of different materials. The composition, manufacturing process, and environmental conditions all effect the structure, and thus affect the way it fractures. To gain a deeper understanding into the process, atomistic modelling of fracture was explored here with relatively simple and pristine materials.

2.10.1 Crystals

A crystalline solid is a solid with an ordered arrangement of atoms which have translational symmetry. Crystals are categorised into 14 *Bravais* lattices,

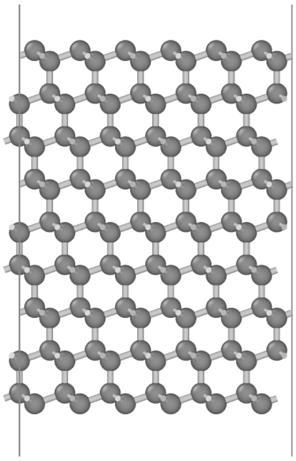

Figure 2.9: A diamond-structured carbon slab with exposed (111) surfaces. The box surrounding the atoms is the computational cell. The box extends well away from the surfaces to implement a vacuum.

which are 14 groups based on their symmetry. Crystallographic planes are noted using the Miller indices, with $[hkl]$ for directions and (hkl) for surfaces. For the case of hexagonal structures, the Bravais-Miller notation is used, with $[hkil]$ for directions and $(hkil)$ for surfaces [30].

A Fourier transform of the Bravais lattice leads to a reciprocal lattice. This allows for study of the lattice through momentum space, i.e. momentum vectors of particles which correspond to its motion. The reciprocal lattice is divided into *Brillouin zones*; the first Brillouin zone is a Wigner–Seitz cell, i.e. primitive cell, of the reciprocal lattice [77].

2.10.2 Carbon

Carbon is one of Earth's most abundant elements [78]. There are many allotropes of carbon, one of which is diamond. Naturally occurring diamond-structured carbon is formed under intense heat and pressure. These days, diamonds can be grown in a few different ways in laboratory conditions and at commercial scales [79]. Diamond is known to have the highest hardness of any natural material. This, coupled with a good thermal conductivity, makes diamond a popular material for cutting tools, coatings, and polishing. At the same time, diamond is brittle, and thus sensitive to flaws, such as defects or microstructural variations [13]. In this work, the atomistic properties of fracture in diamond-structured carbon were investigated.

In particular, fracture systems which were open along the (111) plane

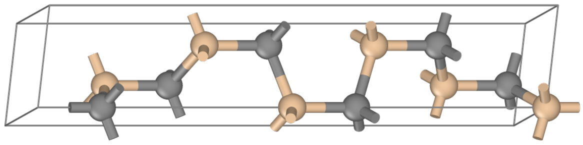

Figure 2.10: Unit cell of the SiC polytype 6H. The hexagonal Bravais lattice is approximately 3.08 Å×3.08 Å×15.12 Å. The carbon and silicon atoms are coloured grey and beige respectively.

were investigated. A slab system with exposed (111) surfaces is shown in Fig. 2.9. For the MM based calculations, the Tersoff screened potential was used to model diamond-structured carbon, as it has been shown to be accurate compared to DFT and experimental results [47]. For the DFT based calculations, the Perdew–Burke–Ernzerhof (PBE) parametrisation of the GGA to the exchange correlation functional was used [80], along with the standard set of ultrasoft pseudopotentials distributed with CASTEP [36].

2.10.3 Silicon Carbide

Ceramics often have a wide range of useful properties which enables them to be used in variety of applications. Ceramics can also be used with common materials to enhance their properties, such as carbon-based ceramics which are used in commercial steel to improve hardening and wear resistance, though at the cost of increased brittleness [12].

SiC is already used in cutting tools, heat exchangers, engine parts, and has potential use in high temperature electronics. A major issue with SiC is that is it extremely brittle and can break during installation [12, 81].

In particular, fracture systems of the SiC 6H polytype, which were open along the (0001) plane, were investigated. The SiC 6H unit cell is shown in Fig. 2.10. For the MM based calculations the Tersoff screened potential was used, as it has been shown to be accurate for modelling the equivalent 3C polytype [47]. For the DFT based calculations, the LDA and PBE parametrisation of the GGA to the exchange correlation functional were used [80], along with the standard set of ultrasoft pseudopotentials distributed with CASTEP [36].

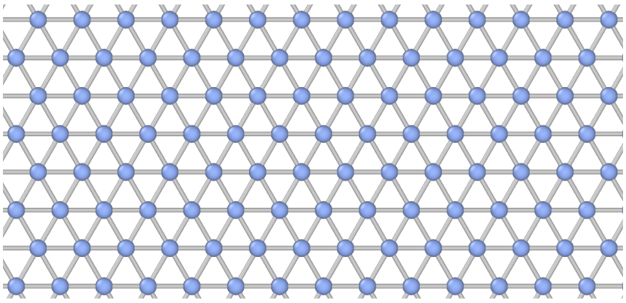

Figure 2.11: Visualisation of a 2D hexagonal lattice with triangular tessellation, with an equilibrium bond length of 1 Å.

2.10.4 Two Dimensional Hexagonal Lattice

A 2D hexagonal lattice with triangular tessellation was used as a simplified material to test methods shown in this work. The model follows the work of M. Marder [82]. The motion of the atoms were restricted to the $x - y$ plane. The lattice had an equilibrium bond length of 1 Å. A visualisation of the lattice is shown in Fig. 2.11. Throughout this work, this lattice will be simply referred to as a 2D hexagonal lattice.

For the MM based calculations three potentials were used, an ideal brittle solid (IBS), a linearised ideal brittle solid (L-IBS), and a LJ potential. The IBS potential produces a brittle response, the L-IBS projects any rotational forces back onto the vector of the atom pair. The LJ potential is a simple two body potential with a long range attractive term and a short range repulsive term [83], which also gives a brittle response. These potentials are described in more detail in Sec. 2.11.

The *edge energy* of this material was computed similarly to that of the surface energy for three dimensional (3D) materials, as described in Sec. 2.7. The energies of the bulk and slab systems are divided over a line segment forming a line energy, or edge energy. In this work, to compute the *surface* energy of this material the computational cells are given a nominal depth of 10 Å. This is to ensure the property maintains the appropriate dimensions for it to be simply used within other equations. In the context of this work, the surface energy for the 2D material will refer to the edge energy over a nominal depth.

2.11 Simple Potentials

In MM, potentials are used to govern the behaviour in which atoms interact. The basis of the potentials used here describe the relationship between the potential energy and the separation between a pair of atoms. In this work, three potentials were used model to the 2D hexagonal lattice.

First, the IBS potential, which is formulated from Hooke's Law, is given by

$$V_{\mathrm{IBS}}(r) = \begin{cases} \frac{1}{2}\kappa(r-a)^2 & \text{for } r < r_{\mathrm{c}}, \\ 0 & \text{for } r \geqslant r_{\mathrm{c}}, \end{cases} \tag{2.98}$$

where κ is the spring constant, a is the characteristic bond length, r is the separation distance between a pair of atoms, and r_{c} is the cutoff distance [82]. The parabolic potential is modified to have a potential energy of zero for distances greater than the cutoff distance. This potential describes a simple model where the atoms break sharply once the separation of a pair of atoms is greater than the cutoff distance. However, this model is non-physical due to the discontinuous change in the potential, and similarly the force, at the cutoff distance. The force is also singular at the cutoff distance. Throughout this work this potential was defined to have $\kappa = 1.0\,\mathrm{eV}\,\text{Å}^{-2}$, and $a = 1.0\,\text{Å}$, where a is the equilibrium bond length for the 2D hexagonal lattice.

While the force response is linear with respect to r, any force component not directly along the bond direction will introduce rotation and thus some non-linearity. The L-IBS potential projects those forces back onto the bond direction, and is given as

$$V_{\text{L-IBS}}(p_i, p_j) = \begin{cases} \frac{1}{2}\kappa\left[(u_j - u_i)\cdot\left(\frac{x_j - x_i}{a}\right)\right]^2 & \text{for } \|p_j - p_i\| < r_{\mathrm{c}}, \\ 0 & \text{for } \|p_j - p_i\| \geqslant r_{\mathrm{c}}, \end{cases} \tag{2.99}$$

where x are the crystal positions; u are the fracture displacements; $p = x + u$ are the positions of the atoms; i and j denote atom indices; a is the characteristic bond; and $\|p_j - p_i\|$ is the separation distance between a pair of atoms. Throughout this work this potential was defined to have $\kappa = 1.0\,\mathrm{eV}\,\text{Å}^{-2}$, and $a = 1.0\,\text{Å}$, where a is the equilibrium bond length for the 2D hexagonal lattice.

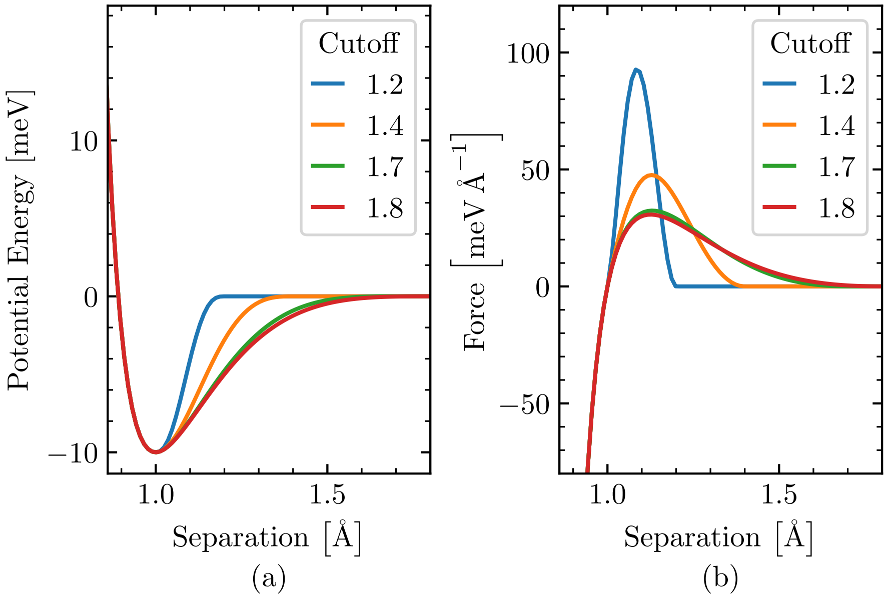

Figure 2.12: a) Potential energy and b) force of the LJ potential of varying cutoff distances with respect to the separation distance of a two atom system.

The LJ potential captures the smooth, continuous potential energy change when breaking a bond, as well as the repulsion of an interaction. The potential is given as

$$V_{\mathrm{LJ}}(r) = \begin{cases} 4\alpha\left[\left(\frac{\beta}{r}\right)^{12} - \left(\frac{\beta}{r}\right)^{6}\right] & \text{for } r < r_{\mathrm{c}}, \\ 0 & \text{for } r \geqslant r_{\mathrm{c}}, \end{cases} \tag{2.100}$$

where r is the separation distance between a pair of atoms, β is a length scale parameter, and α is the depth of the well, such that at a distance of $2^{\frac{1}{6}}$ the potential energy is equal to $-\alpha$. The r^{-12} term encapsulates repulsions at short ranges mimicking the Pauli exclusion principle, and the r^{-6} term describes the attractive forces, i.e. van der Waals forces.

The potential was modified to achieve zero energy at the cutoff distance, r_{c}. The functional form of the potential between the equilibrium length of 1.0 Å and the cutoff distance was modified with a fifth order polynomial. This altered the gradient of the slope at the tail end of the potential, resulting in a difference in stiffness depending on the cutoff distance. In particular, a piecewise quintic regular polynomial was used. The high order of the potential allows enough degrees of freedom to ensure: that the values of minimum point and cutoff point are satisfied; that the first gradient, i.e. the force, is smooth; and that the second gradient, i.e. the gradient of the force, is smooth. Throughout this work this potential was defined to have $\alpha = 0.01\,\mathrm{eV}$ and $\beta = r_\mathrm{c}/2^{(1/6)}$, where r_c has units of Å. A possible range of cutoff distances are shown in Fig. 2.12.

Practically, a cutoff distance should be chosen to reduce the computational expense of computing the energies for atoms at large distances, where the contribution to the overall potential energy is essentially zero.

Specific formulations of potentials are often categorised by the distance at which the potential energies of neighbouring atoms contribute to the potential energy of a single atom. Increasing the distance often increases the complexity of a potential as more atoms are able to influence surrounding atoms. For open fracture surfaces, the main considerations are surface reconstructions and interaction with the opposing surface. Thus, an increasing interaction distance increases the complexity of the model. Further considerations and complexities beyond a pair potential could include angle dependency, such as the SW potential [42].

The hexagonal lattice has an equilibrium bond length of 1.0 Å, and thus a cutoff distance of 1.2 Å would be sufficient to include first nearest neighbour interactions and exclude any second nearest neighbour interactions. This was done to limit the open surface interactions, produce a brittle response, and keep to a simplified model to show a proof of concept of the schemes introduced later.

The LJ potential appears to be smooth for different cutoffs, as shown in Fig. 2.12. However, analysis of how the potential changes with different choices of cutoffs shows a non-smooth functional form of the forces. The forces of the potential reveal the tight curvature needed to meet a cutoff of 1.2 Å, whereas longer cutoffs have smoother curvature, as shown in Fig. 2.12.

Taking the derivatives of the forces reveal even rougher behaviour at shorter cutoffs compared to higher cutoff distances. The first and second gradient of the force at cutoff distances of $r_\mathrm{c} = 1.2$ Å, 1.4 Å, and 2.0 Å are shown in Fig. 2.13.

The gradients display that unexpected behaviour can arise due to a short cutoff. Simulations ran using $r_\mathrm{c} = 1.2$ Å resulted in non-typical and inconsistent behaviour particularly during bond breaking processes. Ultimately,

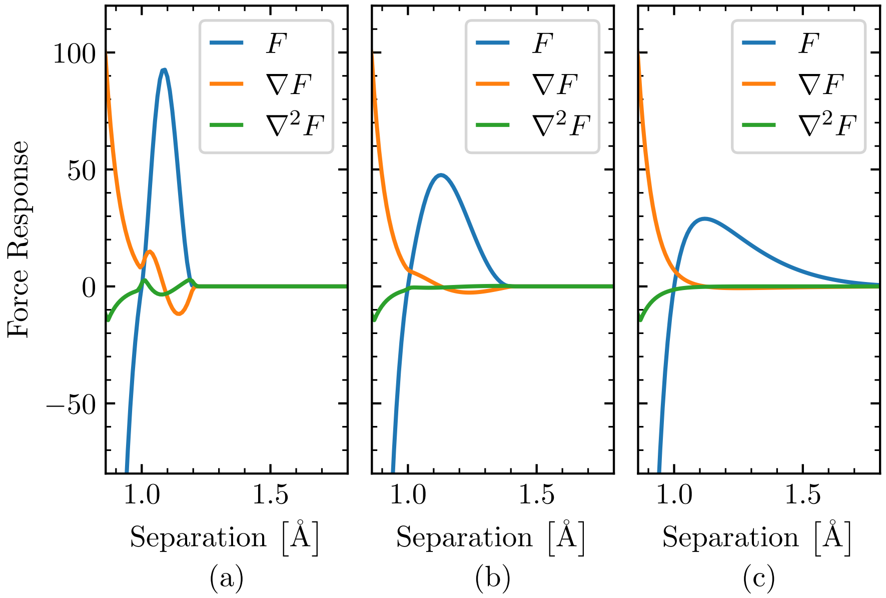

Figure 2.13: The force, F $\left[\mathrm{meV\,Å^{-1}}\right]$, the gradient of the forces, ∇F $\left[\mathrm{meV\,Å^{-2}}\right]$, and the second gradient of the forces, $\nabla^2 F$ $\left[\mathrm{meV\,Å^{-3}}\right]$, for the LJ potential at cutoff distances of r_c equal to a) 1.2 Å, b) 1.4 Å, and c) 2.0 Å.

a cut off distance of 1.4 Å was used, as a compromise to only include first nearest neighbours while achieving a relatively smooth gradient of the force. For reference, the second neighbour distance in the 2D hexagonal lattice is approximately 1.7 Å.

Short range, first nearest neighbour potentials can be problematic. While a continuous and smooth profile of the potential energy will lead to a continuous force profile, it does not guarantee that the profile of the forces are sensible in the context of forces felt on an atom pair. Particular care must be taken when generating and using short range potentials.

2.12 Force Locality

Theoretical potentials have infinite range. In practice, they are truncated because beyond a certain distance the magnitude of the effects are small and can be ignored. In the *ab initio* formulation the electron density is conceptually computed such that every particle is aware of the other. At 0 K a perturbation of one atom could be felt at some distance away. At a finite temperature the stochastic process of the movement of atoms blurs the effect of the force, and as a result shortens the distance at which an atom would feel the perturbation of another atom. Analysis on how a system responds to a small perturbation is key to understanding how properties and parameters may be affected and, more importantly, at what range these affects extend to.

The range of effects of the force on two materials, the 6H polytype of SiC and diamond-structured carbon, were tested. Configurations were sampled from MD simulations at a finite temperature. Individual atoms in the configurations were perturbed. The forces were computed using DFT based code. The forces of the perturbed and unperturbed configuration were then compared.

2.12.1 Molecular Dynamics

In order to simulate an ensemble of possible bulk configurations at finite temperature, a Langevin thermostat was used to moderate the temperature as it was important to sample the canonical ensemble. MD simulations were performed using the screened Tersoff potential [47]. A time step of 1 fs was used.

Each MD simulation started with a bulk crystal. The structure was produced by repeating the crystal unit cell to form a system with approximately 150 atoms. The size chosen was with respect to the computational resources available. The atoms were then given momenta, which were randomly sampled from a Maxwell-Boltzmann distribution of twice the final system temperature desired. The desired temperature was 300 K. The virial theorem relates the time average of the potential energy to the time average of the kinetic energy [39]. The equipartition theorem relates the average kinetic energy to the temperature [41]. Since all the energy is initialised as kinetic energy at the start of the simulation, twice the final temperature was used for the kinetic energy, as the energy was transferred into the potential energy over time.

As the dynamics ran, the system took time to equilibrate the potential energy and the kinetic energy. Once they were roughly equal to each other, then the system can be considered to be in a thermal equilibrium and thus at the desired temperature. The temperature evolution of one simulation is shown in Fig. 2.14. After the system had reached the desired temperature, configurations were sampled from the MD simulation. In total, a hundred different MD simulations were run, where each was initialised with a different seed for which to draw numbers from the normal distribution. For each MD simulation run, two configurations were sampled after 1000 fs had elapsed, with 500 fs between the first and second sample. This was done to ensure as little correlation between the samples.

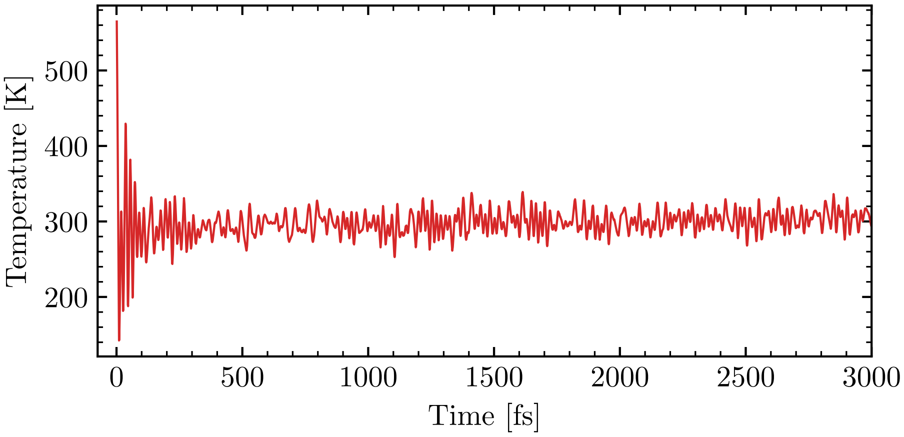

Figure 2.14: Temperature evolution of a MD simulation of a SiC 6H bulk system, modelled with the screened Tersoff potential [47], and using a Langevin thermostat. A time step of 1 fs was used for the Langevin dynamics.

2.12.2 Forces

Each sampled configuration was then run though a CASTEP *single point* calculation. These configurations will be referred to as the *reference configurations*. The single point calculation obtained the forces on each atom as a snapshot of that exact state. The PBE parametrisation of the GGA exchange correlation functional was used [80]. A plane wave cutoff energy of 600 eV with a self-consistent energy tolerance of 10^{-6} eV was adequate as no significant change of the total energy was observed compared to the higher plane wave cutoff energy. Plane wave cutoff energies of 400 eV, 600 eV and 800 eV were tested. The grid of k-points to sample the Brillouin zone was also tested. Tests for $1 \times 1 \times 3$, $2 \times 2 \times 5$, $2 \times 2 \times 8$, and $4 \times 4 \times 15$ showed

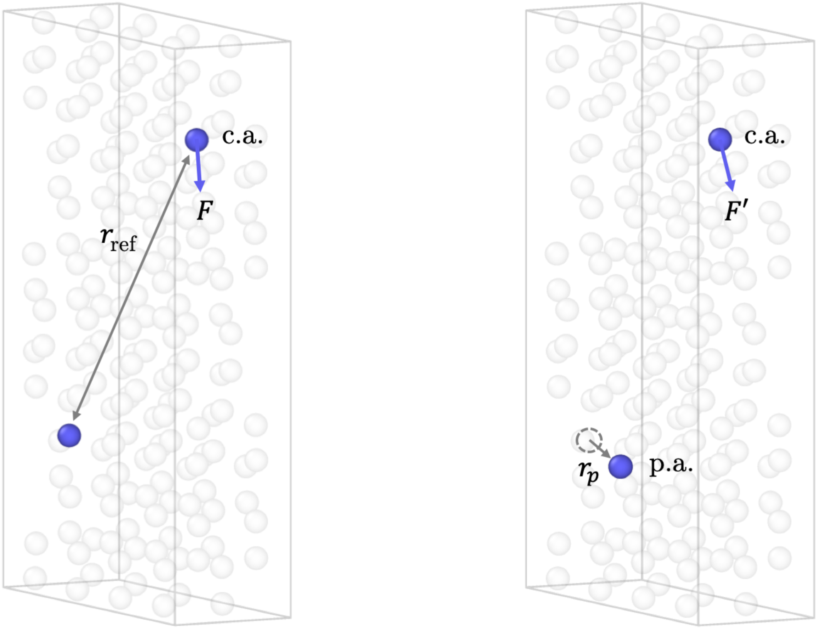

(a) (b)

Figure 2.15: Schematic of the a) reference configuration and the b) perturbed configuration, in which the forces, F and F', of a comparison atom, (c.a.), were compared with respect to the distance, r_{ref}, between the comparison atom's position and the original position of a perturbed atom, (p.a.). The p.a. was perturbed an amount r_p.

that $2 \times 2 \times 8$ was adequate as no significant change of the total energy was observed compared to the denser grid. The energy was converged to within 0.01 eV per atom. The forces were converged to within a tolerance of $0.1\,\text{eV}\,\text{Å}^{-1}$.

The perturbation process was carried out for each reference configuration. First, the configuration was duplicated. A randomly chosen atom in the duplicated configuration was perturbed in the x direction with a length, r_{p}, of 0.01 Å. This configuration will be referred to as the *perturbed configuration*. Each perturbed configuration is then run though the same CASTEP single point calculation. The perturbation process was repeated for another atom for each reference configuration.

The forces between the perturbed and reference configuration were computed. Within the two configurations, a comparison atom was chosen. The absolute force on the comparison atom in the reference configuration, $||F||$, and the perturbed configuration, $||F'||$, was calculated. The difference in the absolute forces, ΔF, acting on the comparison atom was calculated as

$\Delta F = ||F|| - ||F'||$. In the reference configuration, the distance between the comparison atom and original position of the perturbed atom was calculated, r_{ref}, using a minimum image convention to be mindful of the periodic cell. A schematic of the configurations and forces are shown in Fig. 2.15. This process was repeated for a set of comparison atoms, i.e. comparing the force difference of one perturbed atom to many surrounding atoms. The whole comparison process was repeated for each pair of perturbed and reference configurations.

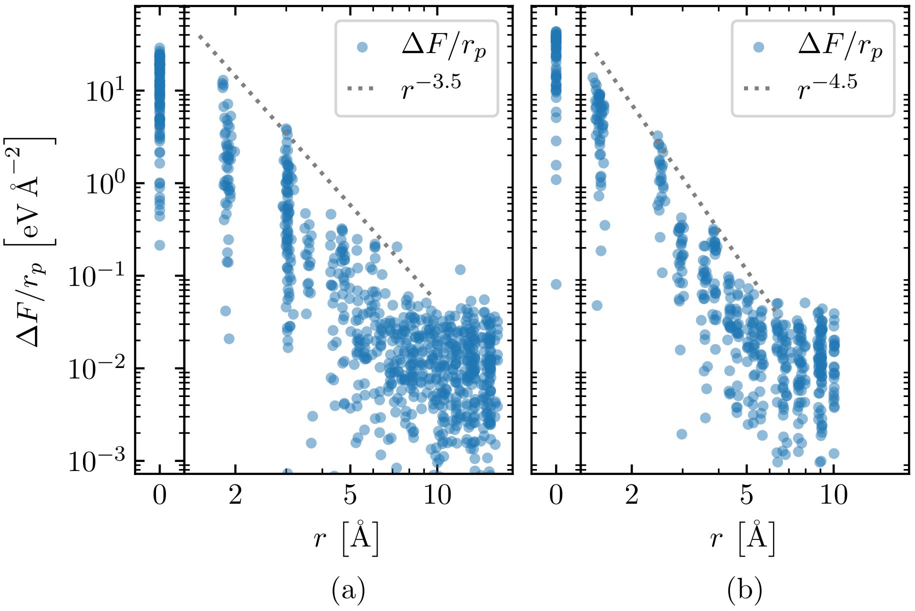

(a) (b)

Figure 2.16: Force locality graphs for both a) bulk SiC 6H and b) bulk diamond-structured carbon. The absolute difference in force, ΔF, between the comparison atom in the reference configuration and the perturbed configuration, normalised with respect to the perturbed length, r_p, is shown as a function of the distance, r, between the original position of the perturbed atom and the comparison atom in the reference configuration. The left panel, in a) and b), at a distance of 0 Å, show the normalised difference in force on the perturbed atom. Rate of decay lines are shown.

The plots in Fig. 2.16 show ΔF normalised with respect to the perturbed length, r_{p}, as a function of the distance from the perturbed atom. $\Delta F/r_{\text{p}}$ levels out beyond a certain radius, likely due to the finite precision of the DFT calculation of forces used here.

As shown in the figures, as the distance from the perturbed atom increases the effect of the perturbation felt by distant atoms decreases. $\Delta F/r_{\text{p}}$ decays, and thus has a form of

$$\frac{\Delta F(r)}{r_{\mathrm{p}}} = \alpha r^{-\beta} + \mu, \tag{2.101}$$

where r is the radial distance, β is the force decay constant, α and μ are constants. β represents the force change per unit length. Eq. 2.101 would allow for predictions on how far a change in an atom's original position would effect the surrounding system. The force decay could also be computed as a function of the perturbed length, r_{p}, or even as a function of a perturbed vector. These would be material dependent, as suggested by the analysis on two crystals examined here. The force is more localised in the diamond system, as shown by the steeper decay rate. The distances at which the perturbations were felt is comparable to the typical cutoff distance of the interatomic potentials used in this work, which was 6 Å.

This method enables a systematic approach to the force locality of a perturbation. The size of a quantum region necessary for QM-MM simulations [10] could be decided by using concepts of this method.

An improvement to this method would be to test the response of perturbing various groups of atoms. A possible limitation made here, was the size of the cell, an improvement could increase the size of the cell to reduce the effects of periodic images. This would modify the force decay rate, as the effects of the perturbation could be measured at greater distances without the influence of interacting with itself in the periodic image. A force locality decay as a function of temperature would also be of interest. Conceptually, this can be computed for different properties and larger length scales, to give insight to how those properties are localised within regions and how their effects begin to fade as the distance increases.

2.13 Summary

Fundamental concepts and the theory required to understand the following work have been outlined. Approaches in computational QM and MM which are used to compute the energies and forces of atomistic configurations were described. Mode I fracture with emphasis on brittle fracture for quasi-static systems was also described. A brief introduction to the materials studied was given, along with the simple potentials used to model the 2D hexagonal lattice. A simple test on the locality of forces within materials was described, with results suggesting that at finite temperature the effect of a perturbed atom is only felt within a finite range.

3 Brittle Fracture of Silicon Carbide

Parts of this chapter build upon the following published article: Sernicola, G., Giovannini, T., Patel, P., Kermode, J. R., Balint, D. S., Britton, T. B. & Giuliani, F. In situ stable crack growth at the micron scale. *Nature Communications* **8,** 108. doi:10.1038/s41467-017-00139-w (Dec. 2017). The experimental work was conducted by Sernicola, G., Giovannini, T., Balint, D. S., Britton, T. B., and Giuliani, F.

3.1 Introduction

Advanced engineering technologies have demanding physical and mechanical specifications, and improvements over today's generation are limited by the performance of available materials. Several applications such as gas turbines, atmospheric re-entry vehicles, and medical implants, require materials with high hardness, high thermal stability, high strength, and low density; ceramics exhibit these attributes [84–87]. However, ceramics are prone to failure via fracture mechanisms as they are generally brittle materials. Understanding these processes could lead to improved manufacturing techniques which allow better resistance to fracture, i.e. their fracture toughness is improved.

The material's strength, or lack thereof, is partly dictated by the grain boundary structure; understanding this would allow for the design of stronger materials. Grain boundaries are the interfaces of differently oriented crystals. Understanding the micro-structure requires experimental and computational tests of individual features to provide mechanistic insight into which grain boundaries are preferred and why.

Precise control during fabrication and manufacturing processes would allow for some control over the micro-structure. Successful manufacturing relies on understanding the processes involved during fabrication, such as preferred boundary orientations and interface chemistry. Then, preferred boundaries can be promoted to grow to tailor the micro-structure and in turn tailor the toughness.

Macroscopic experiments help to understand the limits of components and enable precise measurements of properties at that scale [88–90]. However, properties of individual grain boundaries are not attainable via these tests. Microscopic tests can provide understanding about grain boundaries, which are often attributed to the weakest boundary interfaces. Before studying these interfaces, it would be beneficial to gain a quantitative understanding of the mechanics within the crystal structures themselves.

Fracture toughness can be computed from both microscopic fracture experiments and atomistic simulations. In the work reported here, the experimental fracture toughness was computed via considering the elastic energy in the beams of the double cantilever beam (DCB). The computational fracture toughness was computed using the surface energy of the crystal. Given stable crack growth in the experiments, the static calculations of the surface energy can be compared to the strain energy release rate from the experiment.

Here, the SiC ceramic was investigated. Previous literature has shown that chemistry at the interfaces has a strong influence on the fracture toughness [91, 92]. To explore the mechanics within the crystal, microscale fracture experiments using a wedge nanoindenter to control loading across a long timescale were performed to achieve a slow and stable crack growth. Static DFT energy calculations were performed with considerations of surface termination, surface passivation, surface reconstruction, and MM finite temperature effects. A finite temperature MD simulation was also performed.

3.2 Background

3.2.1 Silicon Carbide

SiC is a relatively common ceramic, example uses include: cutting tools, composite armour, and brake disks [12, 93].

SiC is a bi-elemental crystal, containing silicon and carbon atoms. It is naturally occurring; however, it is extremely rare, and as such almost all

Polytype	Bravais Lattice	Stacking Sequence
3C	face-centred cubic	ABC
6H	hexagonal	ABCACB

Table 3.1: Lattice structure and the stacking sequence of the SiC polytypes 3C and 6H.

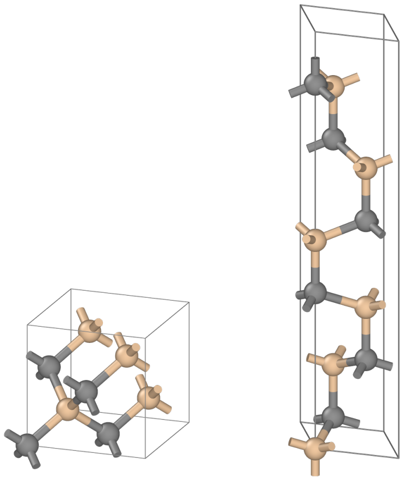
(a) (b)

Figure 3.1: Unit cells of SiC polytypes a) 3C and b) 6H. The cubic unit cell for 3C has a lattice constant of approximately 4.36 Å, and the 6H cell is a hexagonal Bravais lattice of approximately 3.08 Å × 3.08 Å × 15.12 Å. The face of the hexagonal lattice shaped as a rhombus has angles of 60° and 120°. The carbon and silicon atoms are coloured grey and beige respectively.

SiC used for commercial purposes is synthetically produced. SiC has many polytypes. The 6H and 3C are the most common stable polytypes. The unit cells are shown in Fig. 3.1, and the stacking sequences are shown in Table 3.1.

The stacking sequence of a SiC 6H crystal leads to three inequivalent low-index surfaces in the stacking direction. The SiC 6H crystal with a crystallographic surface (0001) was examined here, due to its brittle fracture dynamics, as the bonds are perpendicular to the crack surface. This ensures a straight fracture propagation path, with little to no deviation, or oscillations, as each bond along the fracture path breaks. Cleavage of a perfectly repeating crystal will create two surfaces. Each surface is entirely composed of a single element, where one surface terminates with silicon atoms and the

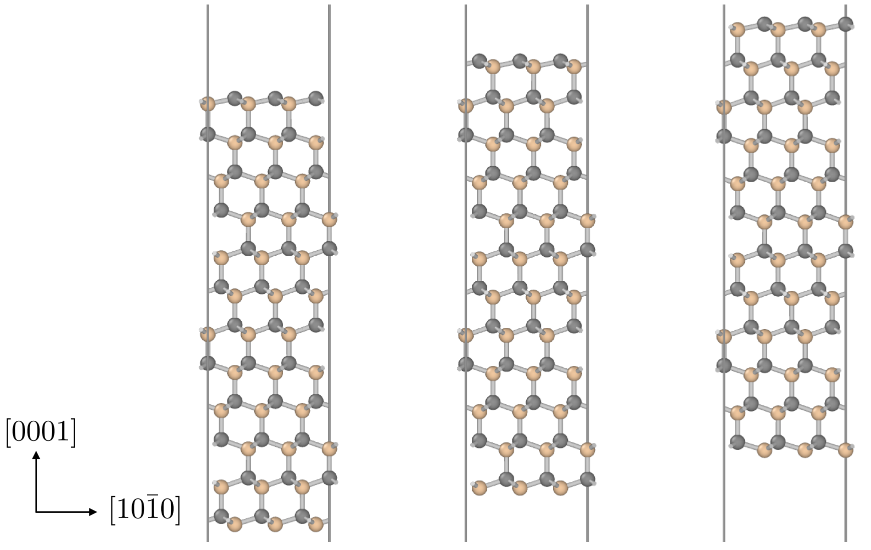

(a) (b) (c)

Figure 3.2: Energy minimised SiC 6H (0001) surface structures. The three inequivalent surface terminations: a), b), and c). The grey lines are the computational cell, which extend away from the surfaces to represent the vacuum required to model the surfaces. The height of the atomic system is approximately 30 Å, with an additional vacuum region of 10 Å on each side. The carbon and silicon atoms are coloured grey and beige, respectively.

other terminates with carbon atoms. For a (0001) surface there are three inequivalent terminations; where the created surfaces are shown at the top and bottom ends of the slab in Fig. 3.2.

3.2.2 Statistical Thermodynamics

In thermodynamics there are a few potentials that quantify the change in energy of a system as it evolves from its initial state to its final state [94].

The Helmholtz free energy, F, describes the energy of *work available* in a system at constant temperature, T, and constant volume, V, defined as

$$F = U - TS, \tag{3.1}$$

where U is the internal energy, T is the temperature, and S is the entropy of the system. The Gibbs free energy, G, similar to Helmholtz free energy, is for a system at constant temperature and constant pressure, p, defined as

$$G = U + pV - TS. \tag{3.2}$$

Both F and G are for systems in which the number of particles in that system remain fixed.

A system at constant temperature is kept at thermal equilibrium with an external *heat bath.* Systems at a finite temperature have many possible configurations and states. *Thermodynamic ensembles* represent the many possible microscopic states with macroscopic constraints. The *canonical ensemble*, or NVT ensemble, describes a system, i.e. fixed number of particles, N, at a constant volume, V, and at a constant temperature, T [95].

The entropy, S, of a system is related to the possible microstates of the system, and is given by

$$S = k_{\mathrm{B}}T \sum_i p_i \ln p_i, \tag{3.3}$$

where k_{B} is Boltzmann's constant, and p_i is the probability that a microstate occurs given by

$$p_i = \frac{1}{Z} e^{-\frac{E_i}{k_{\mathrm{B}}T}}, \tag{3.4}$$

where Z is the partition function. The partition function, Z, for a canonical ensemble is defined as

$$Z = \sum_i e^{-\frac{E_i}{k_{\mathrm{B}}T}}, \tag{3.5}$$

where E_i is the energy of the microstate and acts as a normalisation constant for p_i. It can be shown that Helmholtz free energy can be rewritten in terms of the partition function [95]

$$F = -k_{\mathrm{B}}T \ln Z. \tag{3.6}$$

3.2.3 Phonons

DFT calculations obtain the ground state energy, i.e. the energy at 0 K. For temperatures above 0 K, it is possible to obtain the energy of a system at a finite temperature by considering the dynamics of atoms at a finite temperature.

A phonon represents an excited state of an elastic structure; it is a collective excitation of oscillating atoms in a lattice. They are quantisations of the modes of vibrations of a lattice. Thermal energy, or external forces, causes the lattice to vibrate. This generates phonons, transferring mechanical energy through the material [96].

The energy, E, of the phonon is linked to its frequency, ω, and is given by

$$E = \hbar\omega, \tag{3.7}$$

and its momentum vector, p, is defined as

$$p = \hbar k, \tag{3.8}$$

where k is the wave vector. The relationship between the ω and k is the dispersion relation, $\omega(k)$. The dispersion relation shows all the possible energy states a phonon, and thus the lattice, can be in. The energy of a vibrating system, i.e. a system at a finite temperature, can be determined from the expected phonon states in which the system is vibrating in.

One method to calculate phonons is to use the *frozen phonon* method [97], which is outlined here. A system at the ground state energy has an energy of E_0. For small oscillations, it can be shown, that the energy of a system in which atoms move around their equilibrated positions is

$$\begin{aligned} E(u_{j,l}) = E_0(0) &+ \sum_{j,l} \frac{\partial E_0}{\partial u_{j,l}} \cdot u_{j,l} \\ &+ \frac{1}{2} \sum_{j,l,j',l'} u_{j,l}^T \cdot \frac{\partial^2 E_0}{\partial u_{j,l} \partial u_{j',l'}} \cdot u_{j',l'} + \ldots, \end{aligned} \tag{3.9}$$

where $u_{j,l}$ is a vector of displacements from the atoms' equilibrium positions, j is the atom index in the lth unit cell, and their respective primes denote the other atom in an atom pair [98]. The expansion up to the second order displacements is the harmonic approximation. The higher order terms are the anharmonic terms. The derivatives are computed at the equilibrium configuration. The first order derivative, $\partial E/\partial u$, is the force, and it is equal to zero, since at the equilibrium positions the potential energy of the atom is at a minimum. The second order derivative is an element of the force constant matrix, Φ, where each element is defined as

$$\Phi_{j,l,j',l'} = \frac{\partial^2 E_0}{\partial u_{j,l} \partial u_{j',l'}}. \tag{3.10}$$

Thus, Newton's equation of motion for the motion of the jth atom can be written as

$$m_j \ddot{u}_{j,l}(t) = -\sum_{j',l'} \Phi_{j,l,j',l'} \cdot u_{j',l'}(t). \tag{3.11}$$

Phonons can be described using a wave equation. A general solution to the wave equation is of the form

$$u(x,t) = f(x)e^{i\omega t}, \tag{3.12}$$

where t is time, x is the spatial variable, ω is the angular frequency, and $f(x)$ is a function. For a traveling phonon wave in a 3D lattice, a solution of the wave equation is of the form

$$u_{j,l}(t) = \sum_{k,\beta} U_{j,k,\beta} e^{i(k \cdot r_{j,l} - \omega_\beta(k)t)}, \tag{3.13}$$

where $r_{j,l}$ are the equilibrium positions, β is the dispersion branch index, $\omega_\beta(k)$ is the dispersion branch of index β of wave vector k, and $U_{j,k,\beta}$ is the *displacement vector* which is independent of l due to repeated unit cells that allow the description to be captured by the exponential phase factor [98]. Thus from Newton's equation of motion, the wave solution yields an eigenvalue problem, given by

$$\omega_\beta(k)^2 \epsilon_\beta(k) = D(k) \cdot \epsilon_\beta(k), \tag{3.14}$$

where $\epsilon_\beta(k)$ is the *polarisation vector*, and it combines the displacement vector and masses; and $D(k)$ is the dynamical matrix which is the mass reduced Fourier transform of the force constant matrix. The elements of $\epsilon_\beta(k)$ are

$$\epsilon_{j,\beta}(k) = \sqrt{m_j} U_{j,k,\beta}, \tag{3.15}$$

and the elements of $D(k)$ are

$$D_{j,\alpha,j',\alpha'}(k) = \left(\frac{1}{\sqrt{m_j m_{j'}}} \sum_{l'} \Phi_{j,0,\alpha,j',l',\alpha'} e^{-ik\cdot\left(r_{j',l'} - r_{j,0}\right)} \right). \tag{3.16}$$

The eigenvalues and eigenvectors of the dynamical matrix give the vibrational frequencies and the corresponding atomic motion, respectively [98].

The mean energy of each vibrational mode, $E_\beta(k)$, is

$$E_\beta(k) = \left(\frac{1}{2} + n_\beta(k) \right) \hbar\omega_\beta(k), \tag{3.17}$$

where $n_\beta(k)$ is the number of phonons in the dispersion branch of index β of wave vector k, also known as the *phonon number* [98]. From thermodynamics, the Bose-Einstein distribution gives the phonon number as

$$n_\beta(k) = n(\omega_\beta(k), T) = \frac{1}{\exp\left(\hbar\omega_\beta(k)/k_\mathrm{B}T\right) - 1}, \tag{3.18}$$

where k_B is Boltzmann's constant, and T is the temperature. Thus the expected energy is

$$E = \sum_{k,\beta} \hbar\omega_\beta(k) \left[\frac{1}{2} + \frac{1}{\exp\left(\hbar\omega_\beta(k)/k_\mathrm{B}T\right) - 1} \right]. \tag{3.19}$$

This energy can be substituted into the partition function, Z, and used to compute Helmholtz free energy, F, which provides a way to get the free energy of the system via phonon calculations.

The merits of the harmonic approximation are that it has an exact solution. The Helmholtz free energy is for a fixed volume and as such does not account for thermal expansion. The Gibbs free energy allows for a changing volume, while the pressure remains fixed. A transformation from the Helmholtz free energy to Gibbs free energy is

$$G(T, p) = \min_V [F(T; V) + pV], \tag{3.20}$$

where the Gibbs free energy is the energy that minimises the volume, V.

The Helmholtz free energy can be considered as the sum of the configurational energy, E_c, a vibrational term, F_phonon, and an electronic term,

$F_{\mathrm{electronic}}$ [99]; thus

$$F = E_{\mathrm{c}} + F_{\mathrm{phonon}} + F_{\mathrm{electronic}}. \tag{3.21}$$

E_{c} is the static contribution to the internal energy, i.e. the ground state energy at 0 K, and $F_{\mathrm{electronic}}$ captures the thermal electron contributions and electron-phonon coupling. The $F_{\mathrm{electronic}}$ term was neglected here, as is often done [99–102]. The aim of the investigation performed here was to provide an approximate insight into how the thermal effects can change the surface energy. Hence, only interatomic potentials were used. To compute the electronic contributions suitable electronic computational methods, such as DFT, would need to be used [101]. Furthermore, the temperatures considered here are well below the electronic energy scale, and as such the contribution of electronic excitations to the thermal expansion is negligible [102].

The vibrational term is then computed in terms of the partition function. Substituting the expected phonon energy into the partition function [103] gives

$$\begin{aligned} F_{\mathrm{phonon}} &= -k_{\mathrm{B}}T \ln Z \qquad (3.22)\\ &= \frac{1}{2}\sum_{k,j} \hbar\omega_j(k) + k_{\mathrm{B}}T \sum_{k,j} \ln\left[1 - \exp(-\hbar\omega_j(k)/k_{\mathrm{B}}T)\right]. \qquad (3.23) \end{aligned}$$

Thus $F(T;V)$ is approximately

$$F(T;V) \approx E_{\mathrm{c}}(V) + F_{\mathrm{phonon}}(T;V). \tag{3.24}$$

This calculation is repeated for each temperature at a fixed volume to provide the Helmholtz free energy as a function of temperature.

To account for the thermal expansion at a given temperature, the calculation of Eq. 3.24 is repeated for different volumes, where at each volume the harmonic approximation is held. The volume which minimises the energy is the Gibbs free energy at that temperature. This is the quasi-harmonic approximation [104]. The procedure is repeated for each temperature to provide the Gibbs free energy as a function of temperature.

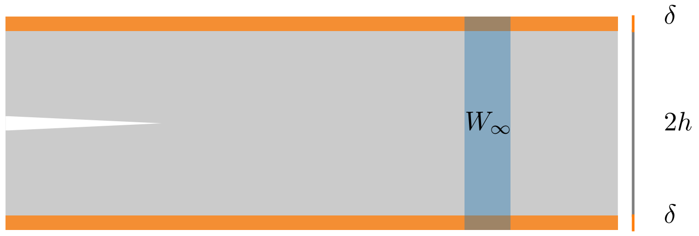

Figure 3.3: Schematic of the thin strip geometry. The geometry is loaded by displacing the top and bottom boundaries, coloured orange, by an amount δ. In simulations this region remains clamped. The energy density, W_∞, far ahead of the crack tip, within the blue coloured region, is independent of the crack length, with $W_\infty = \delta^2 E'/h$, where E' is the effective Young modulus, and h is half of the strip's height.

3.2.4 Finite Temperature Surface Energy

The surface energy at 0 K is calculated as

$$\gamma = \frac{E_{\mathrm{c,s}} - E_{\mathrm{c,b}}}{2A}, \tag{3.25}$$

where the subscripts s and b denote the slab and bulk systems respectively. The surface energy at a finite temperature is given by

$$\begin{aligned} \gamma(T) &= \frac{W_{\mathrm{s}} - W_{\mathrm{b}}}{2A} && (3.26) \\ &\approx \frac{\Big(E_{\mathrm{c,s}} + W_{\mathrm{s,phonon}}(T)\Big) - \Big(E_{\mathrm{c,b}} + W_{\mathrm{b,phonon}}(T)\Big)}{2A}, && (3.27) \end{aligned}$$

where $W(T)$ is either Helmholtz free energy, F, or Gibbs free energy, G, for the harmonic case and for the quasi-harmonic case, respectively.

3.2.5 Thin Strip Geometry

The thin strip geometry consists of a thin slab of material, with a narrow slit as the crack. The edges are clamped and displaced perpendicularly away from the crack tip. A schematic is shown in Fig. 3.3.

To obtain the strain energy release rate, G, the crack length is often required. The advantage of this geometry is that G is independent of the crack length. In an infinitely long slab crack extension is translationally invariant. Since the top and bottom edges are clamped, any change in the energy is through the extension of the crack. Elastic energy density, W_∞, far behind the crack is zero and the release of elastic energy density ahead the crack is equal to the energy release rate, which is

$$W_\infty = \frac{\delta^2 E'}{h} = G, \tag{3.28}$$

where δ is the size of the clamped regions, E' is the effective Young's modulus, and h is half the strip's height [105].

Irwin's solutions to the stress and displacement fields only apply to regions not too far from the crack tip. A modified solution involving higher order terms was achieved by Knauss [106].

3.3 Methodology

The experimental work described within this chapter was conducted by Sernicola, G., Giovannini, T., Balint, D. S., Britton, T. B., and Giuliani, F [1].

3.3.1 Experimental

The experiments loaded a DCB made from SiC to visualise stable crack growth and compute the fracture energy.

Fabrication

The SiC single crystals used for experimental characterisation were 5 mm × 5 mm × 0.5 mm in size and were supplied by the MTI Corporation. The crystals were milled into the DCB shape using focused ion beam (FIB) machining in a FEI Helios Nanolab 600 Dual-Beam, which used an automated path made in the Nano-Builder software. The DCB geometry is shown in Fig. 3.4.

The DCB was first modelled with the finite element method software Ansys. Elastic finite element analysis was used to optimise the initiation of the crack close to the fabricated notch. The final geometry achieved this as it magnified the stress near the notch. The final geometry had dimensions of

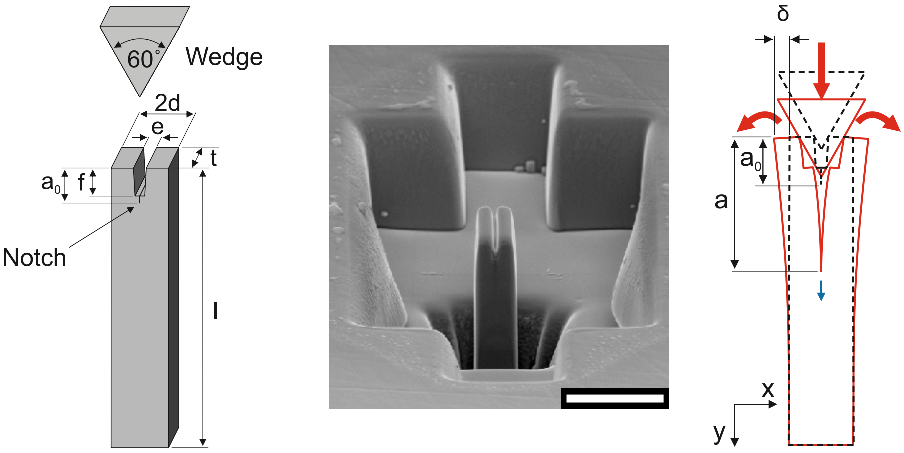

(a) (b) (c)

Figure 3.4: Schematic of the DCB geometry a) and c), where: a is the crack length, with a_0 as the original crack length; d is the beam width; e is the initial notch width; t is the beam depth; l is the beam length; f is the notch length; and δ is the beam displacement [1]. b) A micrograph with a scale bar of 5 µm of the sample is shown. The DCB schematic in c) shows the wedge being used to apply the load, consequently displacing the beams. The red coloured arrows demonstrated the direction of the load and displacements of the geometry. The blue coloured arrow shows the crack growth direction The black dashed lines form the undeformed geometry, and the red lines form the deformed geometry.

15 µm × 2 µm × 5 µm for the height, width, and thickness, respectively. The DCB was machined to align the fracture plane along the (0001) plane, with the notch face in the perpendicular plane leading into the fracture plane. The FIB machining was broken down into several stages; at the end of each stage the sample was realigned to correct for any shift that occurred in that stage. A total of four samples were made. Each sample was imaged using a Auriga Zeiss scanning electron microscope (SEM) and their exact dimensions were measured for use in further analysis.

In theory, the DCB and the alignment of the loading wedge is symmetric. Thus, loading the sample would result in equal strain energy stored in each of the beams. In practice, asymmetries in both structures arise during manufacturing and within the setup. Misalignment between the loading tip's central axis and the DCB central axis would lead to asymmetrical loading. Misalignment between the surface normal and the loading tip's displacement axis would lead to an asymmetrical load angle of each beam. Beam thickness can also vary during automated manufacturing.

Fracture Energy

From simple beam theory, it is possible to obtain the elastic strain energy and thus the strain energy release rate, G, for comparison with the Griffith criterion. The DCB can be modelled as two individual, clamped, end-loaded cantilevers, with the contact point between the beam and the wedge as the loading point. Beam theory can be extended to account for the initial short length of the beam, using the CLE solution for short crack configurations [1]. This is important for cases when the beam length and beam thickness are comparable, as the correction ensures a reliable calculation for a short variable crack length. Thus, the final strain energy release rate for each beam is

$$G = \frac{3Ed^3\delta^2}{8a^4} + \frac{3E(1+\nu)d^5\delta^2}{8a^6} \tag{3.29}$$

where E is the elastic modulus, d is the beam width, δ is the maximum displacement, a is the crack length, and ν is the Poisson's ratio. The first term is the derivative of the elastic strain energy, U_M, with respect to the area, which is given by Euler-Bernoulli beam theory, and the second term is the extension using the linear elasticity solutions for short crack configurations. More details are available in the supplementary information in the article by Sernicola *et al.* [1]. The fracture energy, G_c, is taken as the average strain energy release rate of the samples during the crack growth period.

Mechanical Tests

The mechanical tests were performed *in situ* in a SEM, which allowed for direct observations during the experiment. A wedge was pushed into the notch at the top of the crack in order to advance the crack. The beams split and bent away from the central axis, which drove the crack further.

The SEM provided imaging with a high spatial and temporal resolution, and the visual feedback allowed for good alignment between the loading tip and the sample. It also enabled continuous image capture of the sample during loading and through the slow fracture process. Using a 5 kV beam energy, at a working distance of roughly 5 mm, images were captured using an in-lens detector to measure secondary electrons.

The load was applied with a 60° diamond wedge nanoindenter made by Alemnis, with a nominal tip length of 10 µm. The wedge movement was controlled using a piezoelectric transducer, with control in three spatial dimensions. The indenter was modified to add rotational control, in order to control the angle between the tip of the indenter and notch in the sample. The indenter was moved at rates between $1\,\mathrm{nm\,s^{-1}}$ and $2\,\mathrm{nm\,s^{-1}}$. This helped achieve the slow propagation speed. The rate for each loading period was kept constant to achieve a overall linear displacement profile, with a time length of 6 min. Movement of the indenter was stopped, and the indenter retracted, before complete failure of the DCB. In order to observe the stability of the crack, the sample was loaded and the crack was propagated for a few microns. Then, the indenter was held in place for 2 min to 5 min. The indenter was then either immediately retracted or driven further into the crack to then be retracted later in time.

3.3.2 Computational

The initial crystal structure was obtained from experimental results by Capitani *et al.* via the Inorganic Crystal Structure Database (ICSD) [107]. The unit crystal was then oriented to the [0001] direction, such that any surface created would be along the basal (0001) plane, which matched the mechanical experiment.

Molecular Dynamics Simulation

Initial tests for fracture of SiC began with MD simulations using a thin strip geometry.

The simulations were performed by adapting code written by Kermode [105]. The code was extended to handle hexagonal cell structures. The thin strip system was created by multiplying the unit cell to approximately $290\,\text{Å} \times 90\,\text{Å} \times 12\,\text{Å}$, for its length, height, and depth, respectively. The length and height ratio of $3:1$ was used to mitigate effects from the unclamped boundary that may affect the crack tip during the simulation. An initial crack was formed in the slab, on the left hand side, at an initial length of approximately 40 Å to mitigate boundary effects from the left hand edge. The slab was then relaxed to simulate an initial steady state, i.e. an equilibrated fracture system. The screened Tersoff potential was used to simulate the dynamics. This potential is known to provide an accurate description of SiC [47]. The simulation was performed at a finite temperature of 300 K, with a time step of 1 fs, using the velocity Verlet algorithm. To simulate loading the system, the edges of the system were displaced further, outwards from the centre fracture line, with a strain rate of $10\,\mathrm{ns}^{-1}$. This rate is faster than the rates used in the experiments, which were approximately $1\,\mathrm{ns}^{-1}$. The differences in the strain rate used in these MD fracture simulations and the experiments are not pertinent to the comparison between the experimentally measured fracture energy and the DFT surface energy calculations, since the surface energy calculations have no dependence on a strain rate.

Surface Energy

To compute the surface energy, two systems were required: a bulk system, and a slab system. The oriented crystal unit cell was replicated to generate a bulk crystal. The slab system was created by duplicating the bulk crystal and adding vacuum in the [0001] direction, on either side creating two surfaces. The surfaces are either entirely silicon- or carbon-terminated. The stacking sequence leads to the choice of three possible inequivalent terminations. In practice, the slab system was created after a well converged bulk system was calculated, the process of which is described below.

To ensure a self-consistent well converged final surface energy, several convergence tests were performed with respect to the system's total energy and forces. These tests involved geometry optimisations through a DFT based scheme using CASTEP [36].

The computational cells for the bulk and slab systems were periodic in all directions. During the geometry optimisation, the atoms in the bulk system and the enclosing cell were free to move. In the slab system, the enclosing cell was kept fixed to maintain the vacuum.

The grid of k-points to sample the Brillouin zone was also converged. Tests for $4 \times 4 \times 4$, $6 \times 6 \times 6$, and $8 \times 8 \times 8$ for the bulk cell showed that $4 \times 4 \times 4$ was adequate, as no significant change in the total energy was observed compared to the denser grids. The energy was converged to within $0.01\,\mathrm{eV}$ per atom.

The plane wave basis set was converged. Tests for the plane wave cutoff energies of $200\,\mathrm{eV}$, $400\,\mathrm{eV}$, $600\,\mathrm{eV}$, and $800\,\mathrm{eV}$ were performed at the three different k-point densities, mentioned above. $600\,\mathrm{eV}$ was adequate as no significant change in the total energy or forces were observed compared to the higher energies. A plane wave basis set of 600 eV with a self-consistent energy tolerance of 10^{-6} eV was chosen, and a finite basis set correction was used to account for changes in the cell size during the geometry optimisation. The standard set of ultrasoft pseudopotentials distributed with CASTEP were used [36]. The geometry optimisation calculations were performed with the LDA and the PBE parametrisation of the GGA to the exchange correlation functional [80].

The bulk crystal was relaxed to within a force tolerance of $0.05\,\mathrm{eV\,\AA^{-1}}$ and a stress tolerance of 0.1 GPa. The slab system was tested with different vacuum spacings. This was to ensure the periodic images of the slab were decoupled from one another. A vacuum of 10.0 Å on each side was found to be sufficient, to have the energy of the system converged to within 0.01 eV per atom. This was compared to vacuum spacings of 20.0 Å and 30.0 Å. The number of layers, i.e. the height of the slab, was tested to remove any interaction effects of the two surfaces within the structure. Up to four repeat unit cells along the [0001] direction were tested, and it was found that two repeated unit cells were sufficient to have the energy of the system converged to within 0.05 eV per atom. This resulted in a system with 24 atoms.

Geometry optimisations were performed on both the bulk and slab systems. The optimisations were performed with the BFGS method. Then the surface energy was computed. In the slab system each surface is entirely composed of a single element, where one surface terminates with silicon atoms and the other terminates with carbon atoms. Thus, the surface energy is effectively averaged across both of the surfaces. Leung *et al.* used a similar approach for modelling the polytype SiC 3C [108]. The DFT calculations gave an energy minimised, zero temperature, surface energy in a perfectly clean environment.

Critical Stress Intensity Factor

The elastic constant matrix, C, was computed for both exchange correlation functionals. The 21 independent C_{ij} components were computed. For each C_{ij} component, a bulk system was strained for five points in the range of $-1.5\,\%$ to $1.5\,\%$ and, for each point, the stress was computed. The gradient of a straight line from a least squares fit of the points determined the elastic constant. The error of the elastic constants was the error of the least squares fit [109].

The Young's modulus was extracted from the compliance matrix, S, where $S = C^{-1}$ [76]. The error of the Young's modulus was propagated forwards using interval analysis from the errors on the fit of the strain-stress lines. Each elastic constant was represented as a range of values, with the errors forming the range for each constant, i.e. $[C_{ij} - \mathrm{err}_{ij}, C_{ij}, C_{ij} + \mathrm{err}_{ij}]$. The extrema of the ranges and median were used to build three elastic constant matrices. The Young's modulus was computed for each matrix. The maximum difference between the Young modulus of the median matrix and the Young's modulus of the extrema matrices was used as the error.

The surface energy and the Young's modulus was then used to compute the critical stress intensity factor, which is given by $K_\mathrm{c} = \sqrt{G_\mathrm{c} E'}$.

Surface Passivation

Bare and perfectly cleaved surfaces are not common in nature. The surface structure can change due to exposure to the atmosphere. The experiment was performed in a vacuum. However, the vacuum within the chamber is not perfect and some atoms may interact with the material. Exposure to an atmosphere can lead to the surface reacting and becoming passive, which reduces the surface energy.

Two methods to obtain the surface energy were considered: the standard method, where the surface energy is an average surface energy across both surfaces in a slab system; and the *isolated* method, where the surface energy was computed for individual surfaces in a slab system. The effects of surface passivation were considered by passivating the surfaces with hydrogen. For each method, the surfaces were passivated and the passivated surface energy was computed.

The approach used here is built upon an approach used by Abavare *et al.* [110], where the surface energy was computed with chemical potentials. The surface energy using chemical potentials, γ_s, is defined as

$$\gamma_\mathrm{s} = \frac{1}{2A} \left(E_\mathrm{slab} - \mu_\mathrm{SiC} N_\mathrm{SiC} \right), \tag{3.30}$$

where A is the surface area, E_slab is the energy of the SiC slab system, μ_SiC is the SiC chemical potential of bulk SiC, and N_SiC is the number of atoms in the slab system. Since $\mu_\mathrm{SiC} N_\mathrm{SiC} = E_\mathrm{bulk}$, this equation is equivalent to the previous surface energy definition in Eq. 2.71. Both surfaces of the slab system are considered; thus the surface energy is effectively the average across the two surfaces. This surface energy definition will be referred to as the standard surface energy and the standard method.

Abavare *et al.* proposed hydrogen termination of either surface to investigate the surface energy of a single surface. In general, the surface energy can be considered as the energy increase due to the formation of dangling bonds along the newly created surface. In a slab system, hydrogen termination of one surface removes the dangling bonds along that surface. This leaves the non-terminated surface clean for surface energy investigation [110]. Using chemical potentials, the surface energy of the unterminated surface, γ_{i}, is defined as

$$\gamma_{\mathrm{i}} = \frac{1}{A}\Big(E_{\mathrm{slab,\,t}} - (\mu_{\mathrm{SiC}} N_{\mathrm{SiC}} + \mu_{\mathrm{H},X} N_{\mathrm{H},X})\Big), \tag{3.31}$$

where $E_{\mathrm{slab,\,t}}$ is the energy of the slab system with one terminated surface, $N_{\mathrm{H},X}$ is the number of hydrogen atoms used to terminate one surface, $\mu_{\mathrm{H},X}$ is the hydrogen chemical potential, and X denotes the molecule used to compute the hydrogen chemical potential for the hydrogen atoms which terminate the surface. This surface energy definition will be referred to as the isolated surface energy and the isolated method.

In Eq. 3.30 the factor of 2 accounts for the two surfaces in a slab system. In Eq. 3.31 there is no factor of 2, as only one surface in the slab system is investigated. The sum of the two isolated surface energies can be shown to equal twice the standard surface energy. The energies of the terminated systems used to compute the isolated surface energies are $E_{\mathrm{slab,\,t}}$ and $E_{\mathrm{slab,\,t'}}$, where t and t′ denote termination on opposites sides of a slab. The sum of these energies can be considered as the combination of: the energy of a non-terminated slab, E_{slab}; the energy of an additional set of bulk SiC atoms, as the sum involves two slab systems; and the energy of two sets of hydrogen atoms, to account for the hydrogen termination of a surface on each slab system. This can be written as

$$E_{\mathrm{slab,\,t}} + E_{\mathrm{slab,\,t'}} = E_{\mathrm{slab}} + \mu_{\mathrm{SiC}} N_{\mathrm{SiC}} + \mu_{\mathrm{H},X} N_{\mathrm{H},X} + \mu_{\mathrm{H},X'} N_{\mathrm{H},X'}, \tag{3.32}$$

where X and X' denote the molecules used for the terminated surfaces.

The sum of the two isolated surface energies, $\gamma_{\text{i, t}}$ and $\gamma_{\text{i, t}'}$, using Eq. 3.31, is

$$
\begin{aligned}
2\gamma &= \gamma_{\text{i, t}} + \gamma_{\text{i, t}'} && (3.33)\\
&= \frac{1}{A}\Big(E_{\text{slab, t}} - (\mu_{\text{SiC}}N_{\text{SiC}} + \mu_{\text{H},X}N_{\text{H},X})\Big)\\
&\qquad + \frac{1}{A}\Big(E_{\text{slab, t}'} - (\mu_{\text{SiC}}N_{\text{SiC}} + \mu_{\text{H},X'}N_{\text{H},X'})\Big) && (3.34)\\
&= \frac{1}{A}\Big(E_{\text{slab, t}} + E_{\text{slab, t}'} - 2\mu_{\text{SiC}}N_{\text{SiC}} - \mu_{\text{H},X}N_{\text{H},X} - \mu_{\text{H},X'}N_{\text{H},X'}\Big). && (3.35)
\end{aligned}
$$

Then, substituting in Eq. 3.32 gives

$$2\gamma = \frac{1}{A}\Big(E_{\text{slab}} - \mu_{\text{SiC}}N_{\text{SiC}}\Big), \tag{3.36}$$

which is twice the standard surface energy, and thus

$$\gamma = \frac{1}{2A}\Big(E_{\text{slab}} - \mu_{\text{SiC}}N_{\text{SiC}}\Big), \tag{3.37}$$

which is the standard surface energy as defined in Eq. 3.30. Thus, Eq. 3.31 calculates the surface energy of a single surface, and therefore no factor of 2 is required.

The isolated surface energy was computed using reference chemical potentials from silane and methane molecules. Different molecules are used for the hydrogen chemical potential, $\mu_{\text{H},X}$, as the hydrogen atoms are either attached to the carbon-rich surface or the silicon-rich surface. Thus, $\mu_{\text{H},X}$ is given by either

$$\mu_{\text{H,CH}_4} = \frac{1}{4}(\mu_{\text{CH}_4} - \mu_{\text{C}}), \tag{3.38}$$

or

$$\mu_{\text{H,SiH}_4} = \frac{1}{4}(\mu_{\text{SiH}_4} - \mu_{\text{Si}}), \tag{3.39}$$

where μ_{CH_4}, μ_{SiH_4}, μ_{C}, and μ_{Si} are the chemical potentials for methane, silane, carbon, and silicon respectively [110].

Methane and silane were used as reference chemical potentials as they are simple, stable molecules of carbon with hydrogen and silicon with hydrogen, respectively. In particular, all the free electrons of the carbon atom and silicon atom are covalently bonded with the electrons of the hydrogen atoms. Similarly, diamond cubic forms of carbon and silicon were used as all the free electrons are covalently bonded with electrons from the other carbon atoms and silicon atoms, respectively. This maintained a consistent bonding environment to obtain a reasonable hydrogen-carbon and hydrogen-silicon chemical potential. The chemical potentials were computed and converged using CASTEP, using a similar approach to the method used for the SiC systems.

The isolated method is useful for systems where the two surfaces are inequivalent, as it does not average over the chemically different surfaces. Abavare *et al.* took this approach with the 3C polytype, since the surfaces are inequivalent. The surfaces of the polytypes 3C and 6H are similar, which gives confidence in using this approach for the 6H polytype. They also noted that large system sizes are required for polar surfaces in order to mitigate long range interactions. This makes convergence with respect to system size slow [110].

The effects of environmental hydrogen passivation was computed by considering H_2 molecules which dissociate and combine with the surface or surfaces. The standard surface energy under environmental hydrogen passivation, $\gamma_{\mathrm{s,\ p}}$, was calculated as

$$\gamma_{\mathrm{s,\ p}} = \frac{1}{2A}\left(E_{\mathrm{slab,\ 2t}} - \mu_{\mathrm{SiC}}N_{\mathrm{SiC}} - \mu_{\mathrm{H}}N_{\mathrm{H}}\right), \tag{3.40}$$

where $E_{\mathrm{slab,\ 2t}}$ is the energy of the slab system where both surfaces have hydrogen attached to them; μ_{H} is the hydrogen chemical potential, which was computed using H_2 as the reference molecule; and N_{H} is the number of hydrogen atoms used for environmental passivation. The isolated surface energy under environmental hydrogen passivation, $\gamma_{\mathrm{i,\ p}}$, was calculated as

$$\gamma_{\mathrm{i,\ p}} = \frac{1}{A}\big(E_{\mathrm{slab,\ 2t}} - (\mu_{\mathrm{SiC}}N_{\mathrm{SiC}} + \mu_{\mathrm{H},X}N_{\mathrm{H},X}) - \mu_{\mathrm{H}}N_{\mathrm{H}}\big). \tag{3.41}$$

The surface energies using chemical potentials were calculated for the SiC 6H (0001) surfaces. Two surfaces are created during fracture propagation. Thus, twice the surface energy, 2γ, is an appropriate quantity to compute. The surface energy with no terminated surfaces is equivalent to the definition of surface energy in Eq. 2.71. The system was hydrogen passivated and the passivated surface energy was computed. The systems used for these calculations are shown in Fig. 3.5.

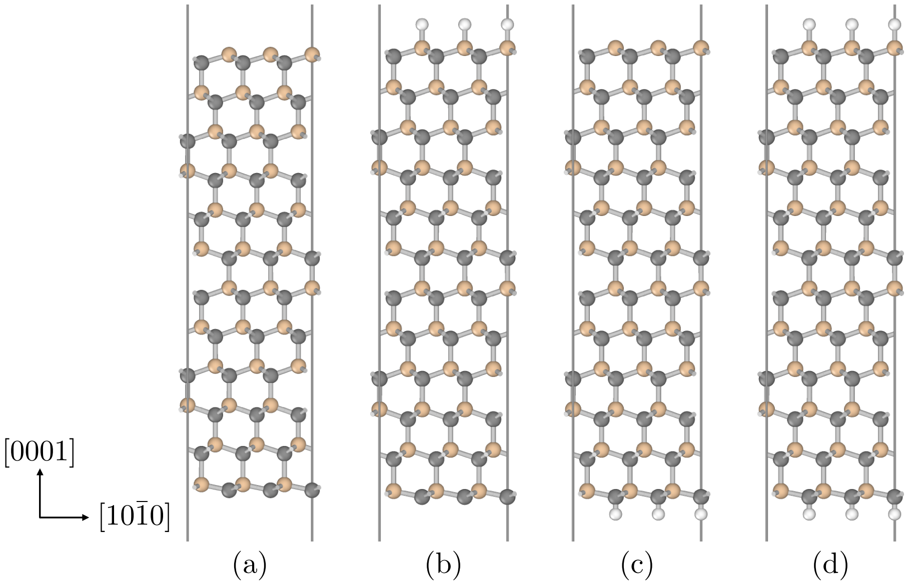

(a) (b) (c) (d)

Figure 3.5: SiC 6H slab systems where the (0001) surfaces are passivated, or terminated, with hydrogen. In system: a) no surfaces are terminated, b) the silicon-rich surface is terminated, c) the carbon-rich surface is terminated, and d) both the silicon-rich and carbon-rich surfaces are passivated, or terminated. The carbon, silicon, and hydrogen atoms are coloured grey, beige, and white respectively. The grey lines are the computational cell, which extend away from the surfaces to represent the vacuum required to model the surfaces. The height of the atomic system was approximately 30 Å, with an additional vacuum region of 10 Å on each side.

The isolated surface energies were computed, and 2γ was computed as the addition of the silicon-rich surface energy and the carbon-rich surface energy. Similarly, the systems were hydrogen passivated and the passivated surface energies were computed. Twice the passivated surface energy was computed as the addition of the passivated silicon-rich isolated surface energy and the passivated carbon-rich isolated surface energy. The systems used for these calculations are shown in Fig. 3.5.

The isolated surface energies for the SiC 3C (111) surfaces were also calculated. This allowed comparison of the method used here and the method used by Abavare *et al.* The SiC 3C bulk and surface systems were generated in a similar manner to the SiC 6H systems.

Surface Reconstructions

The surface structure can deform and reconstruct along the surface of the crack. A dynamically created surface can reconstruct into different arrangements due to new free electrons from the process of breaking bonds, as well as extra energy to overcome reconstruction barriers. The atoms can reconstruct to form a lower energy state.

The more widely studied 3C (111) surface, which is structurally related to the 6H (0001) surface, has a number of known surface reconstructions. Previous literature shows that these reconstructions require additional atoms, such as: silicon atoms [111], or environmental molecules such as H_2 or O_2 [112].

Brittle cleavage follows Griffith's energy balance, and so it usually argued that the relevant surface energy is the as-cleaved surface energy [14]. Thus, for surface reconstruction to have an effect on the surface energy for creating new surfaces the process must happen instantaneously at the propagating crack tip [113]. In other words, the energy required to reconstruct must be smaller in comparison to the energy barrier of the propagating crack.

The energy of the systems were calculated from a geometry optimised relaxed configuration and thus allow for the exclusion of barrierless surface reconstructions.

Temperature Effects

The DFT geometry optimisations performed here were at 0 K. The experiment was performed at room temperature. Thermal excitations can propagate the crack by allowing the system to more easily overcome energy barriers, which in turn reduces the surface energy. For the similar polytype 3C at 300 K Leung *et al.* saw up to a 15 % decrease in surface energies [108].

Temperature effects can be measured via phonon-based methods. DFT-based phonon methods are computationally expensive. Since earlier MD simulations produced qualitative results that match more accurate methods, the effects of temperature on the surface energy were assessed using empirical interatomic potentials. The Tersoff and Erhart screened interatomic potential and the Albe screened interatomic potential were used, as they are known to provide accurate descriptions of SiC [47]. Static surface energies using the interatomic potentials were computed to use as reference points. The systems were minimised using the FIRE algorithm.

The entropic contributions were computed via the frozen phonon method using the *phonopy* code [114]. The force constant matrix, Φ of Eq. 3.10, of the system was computed using a modified Parlinski-Li-Kawazoe method [115]. The phonon dispersions, $\omega_\beta(k)$, were calculated by solving the eigenvalue problem, Eq. 3.14, of the wave equation and the dynamical matrix constructed from the force constants, Eq. 3.16. The phonon dispersions were calculated under both the harmonic approximation and the quasi-harmonic approximation.

Convergence tests were performed with respect to the supercell, i.e. repeat number of cells, and the k-point mesh. A supercell of $2 \times 2 \times 2$ and a k-point mesh of $20 \times 20 \times 20$ was found to be adequate.

The Helmholtz and Gibbs free energies were computed, to then compute the finite temperature surface energy for the harmonic and quasi-harmonic schema respectively, where the surface energy is given by Eq. 3.27.

3.4 Results and Discussion

The experimental work described within this chapter was conducted by Sernicola, G., Giovannini, T., Balint, D. S., Britton, T. B., and Giuliani, F [1].

3.4.1 Experimental

Measurements were taken from the SEM images of the sample. In total four samples were loaded and fractured with slightly different displacement profiles of the loading wedge. A selection of SEM images from one of the samples is shown in Fig. 3.6.

During the measurements, some of the asymmetries listed earlier were observed, such as differences in beam thickness. When the samples were loaded, the cracks did not form in line with the central axis. Instead, they were offset by tens of nanometres to the side of the milled notch. This was as a result of asymmetries in the loading of the sample, and this required the beams to be treated independently for the analysis and measurements. The energies calculated take into account the discrepancies in the beams and so do not under- or over-estimate the final energy.

The loading wedge's tip displacement was controlled using a piezoelectric transducer. Measurements of the cantilever width, crack length, and each

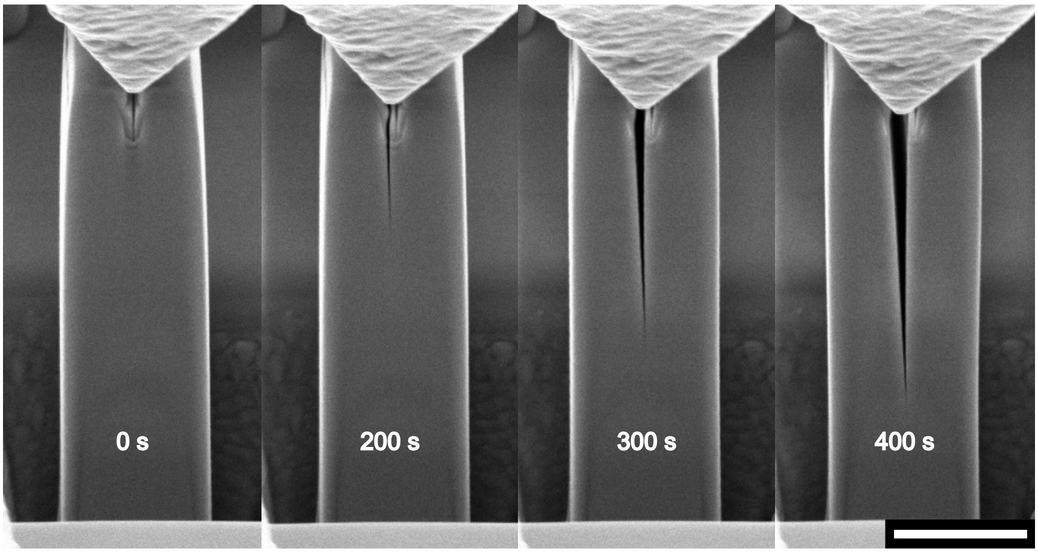

Figure 3.6: Selection of frames extracted from the video recorded of a loaded SiC DCB sample inside an SEM [1]. The time elapsed from the initial loading of each image from left to right is 0 s, 200 s, 300 s, and 400 s. The wedge, at the top, loads the DCB, as it advances downwards, further splitting the sample. Scale bar: 2 µm.

beam's displacement were extracted from the SEM images by hand. A Monte Carlo error analysis was used to compute the errors on these properties. Variables with known errors were independently adjusted to have a Gaussian distribution, with the measurement as the mean and the measurement error as the standard deviation.

The data analysis steps, for one sample, S3, are shown in Fig. 3.7. The figure shows the following all as a function of time: the displacement profile of the loading wedge, the independent beam displacements obtained from the SEM images, and the crack length. The displacement profiles with respect to time for each sample, along with the computed fracture energy as a function of crack length are shown in Fig. 3.8.

When loaded, three samples formed a crack, approximately 100 nm in length, slightly to the left, which is indicative of a slight asymmetry in the loading geometry. The crack in the fourth sample grew without any bursts for the whole test period.

For one sample, the deflection of the beams over time is shown in Fig. 3.7 b). The measurements were done from the SEM images, and thus pixel counts were converted into distance measures. The beams initially did not move under an increasing load, i.e. tip displacement remained constant for some time, which indicated the sample was absorbing the energy. The bend-

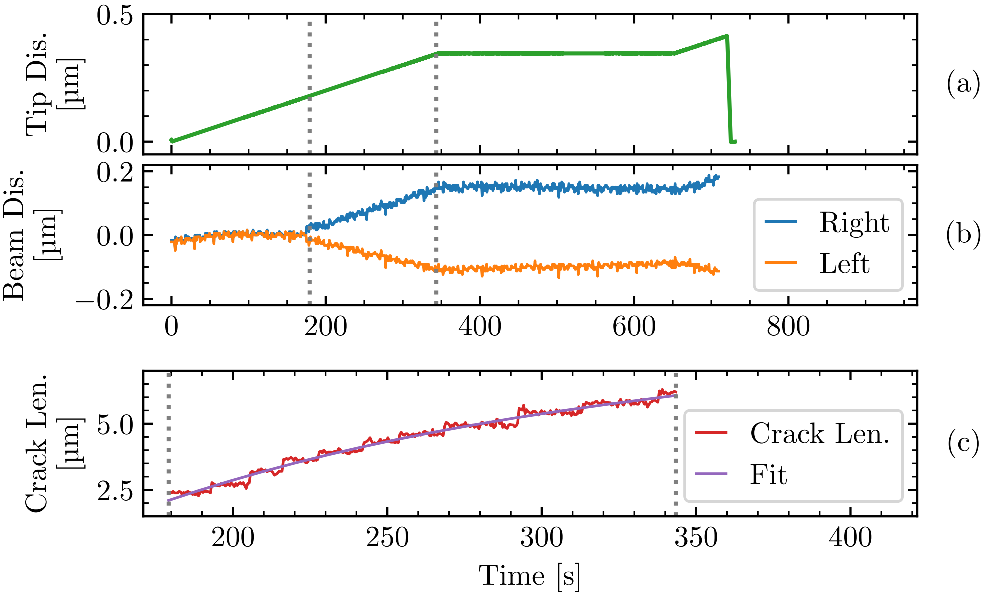

Figure 3.7: Data analysis of a SiC 6H DCB sample, which was open along the (0001) plane, where the crack within the sample was driven forward by driving a wedge into the sample [1]. a) The displacement profile of the loading wedge with respect to time. b) The beam displacement with respect to time, which shows displacement of the left beam and the right beam independently. c) Crack length measured from the nucleation point of the sample, with respect to time. A fit through the crack length was used for the fracture energy calculations. The period in which crack growth was measured is marked with grey coloured dashed lines in a), b), and c). In particular, this data is from sample 3, S3 as labelled in the text and other figures.

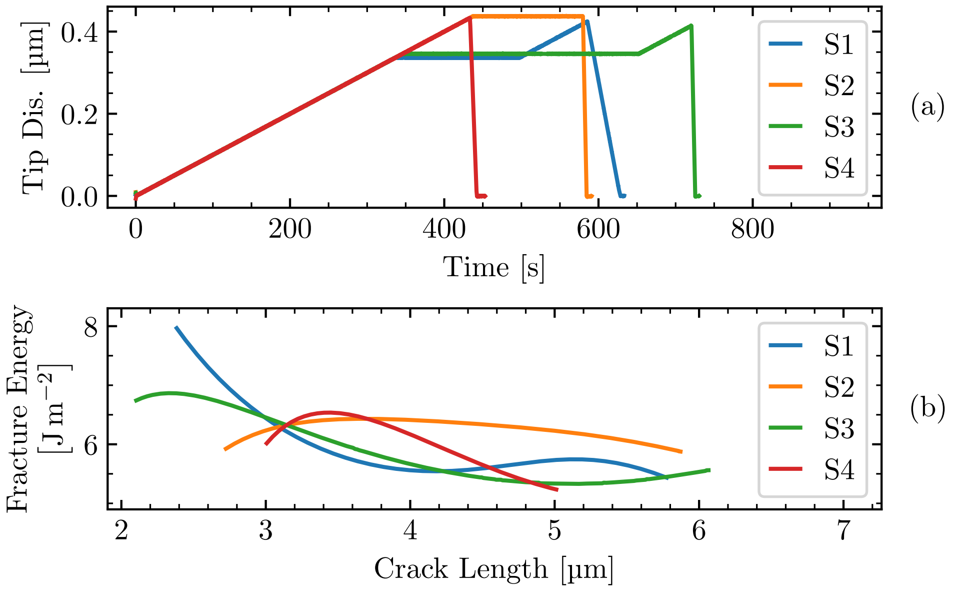

Figure 3.8: Fracture energies of the SiC 6H (0001) surface, which were obtained through loading of DCB samples [1]. a) The displacement profile of the loading wedge for each of the four DCB samples, labelled S1 to S4. SEM images were taken and the crack length was extracted. A fit of the crack length was used to compute the fracture energy, which is shown in b).

ing started at around 200 s and continued for 100 s, during which the crack grew linearly.

The fracture energy measurements were performed during the linear displacement period of the beams. The fracture paths of the DCBs in the SEM images showed a linear crack propagation with a sharp tip, and so no plastic deformation was expected [1]. These measurements were taken at a distance well away from the notch, and it is expected that the energy would not be affected by the crack initiation process or ion penetration damage which is found to be <100 nm from the surface [116, 117].

For each frame during the crack growth period the crack length was measured. The crack length, as shown for one sample in Fig. 3.7 c), jolts in small increments. Over a period of roughly 10 s the jolts are relatively small compared to the total time period of almost approximately 200 s. The crack tip data was fitted to a third-order polynomial to reduce noise for the fracture energy calculation. The fracture energy was computed using the smoothed crack length data. The Poisson's ratio and elastic modulus were calculated from Landolt-Börnstein values for the (0001) plane [1]. The fracture energy was then calculated for each sample. The average fracture energy was $(5.95 \pm 1.79)\,\mathrm{J\,m^{-2}}$. The energies are shown in Fig. 3.9, alongside the DFT results and previous literature. The experimental fracture energy values are also summarised in Table 3.5.

The stability of the crack was demonstrated by holding the wedge for 5 min, which showed no advancement of the crack tip. Only when the tip was further displaced into the sample did the crack tip progress.

The fracture toughness, K_c, was also calculated. The Poisson's ratio was computed to be 0.08 [1]. Thus, the difference in the effective Young's modulus between the plane stress and the plane strain cases is small. Therefore, the plane stress case was used to compute the fracture toughness. The average fracture toughness was found to be $(1.80 \pm 0.26)\,\mathrm{MPa}\sqrt{\mathrm{m}}$ [1].

3.4.2 Computational

Molecular Dynamics Simulation

The results of the MD simulations show a brittle response in a thin strip geometry, as shown in Fig. 3.10, which agrees with experimental results [1]. While the potential was adequately able to capture the dynamics for a pure

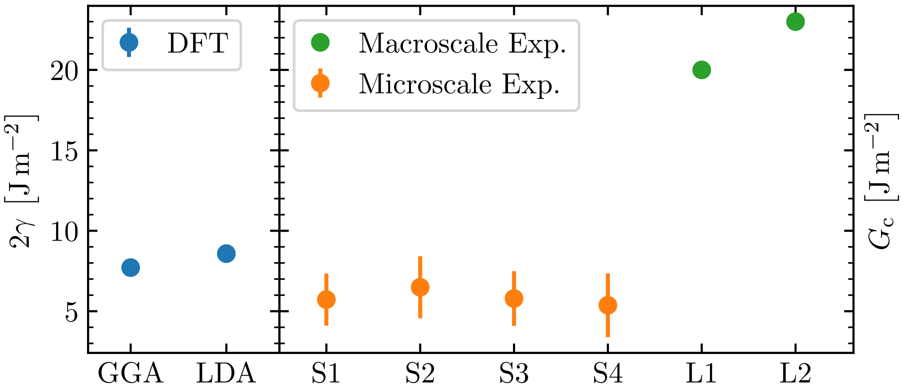

Figure 3.9: Fracture energies, G_c, of the SiC 6H (0001) surface, obtained from microscale tests of loading a DCB; four samples are shown labelled S1 to S4 [1]. Twice the surface energies values, 2γ, from DFT simulations, of two exchange correlations, PBE and LDA [1]. Fracture energies from macroscopic tests in literature by McColm [118] and Henshall *et al.* [119], labelled L1 and L2 respectively.

crystal, the potential is not expected to be transferable, e.g. to a system with environmental chemistry such as stress corrosion cracking.

The system was considered to be large enough to be self-thermostatic, as the temperature throughout the simulation was monitored and found to roughly maintain 300 K, and thus it did not require an external thermostat.

The surface energy with the Tersoff potential of two surfaces gives $2\gamma = 3.7\,\mathrm{J\,m^{-2}}$. The Young's modulus was computed to be 509.0 GPa and the Poisson ratio was 0.047. The fracture toughness, using the plane stress case for the effective Young's modulus, was calculated to be $1.37\,\mathrm{MPa}\sqrt{\mathrm{m}}$.

Simple MD was found to be adequate for simulating brittle fracture in SiC. However, it did not provide accurate quantitative values on the process or structure. Instead, DFT was used to provide more accurate energies, at a cost of reduced simulation size and reduced timescales.

Surface Passivation

Exposure of the surfaces to an atmosphere can lead to the surface reacting and becoming passive, which reduces the surface energy. The effects of surface passivation were considered by passivating the silicon-rich and carbon-rich surfaces with hydrogen.

The surface energy was calculated using two methods: the standard

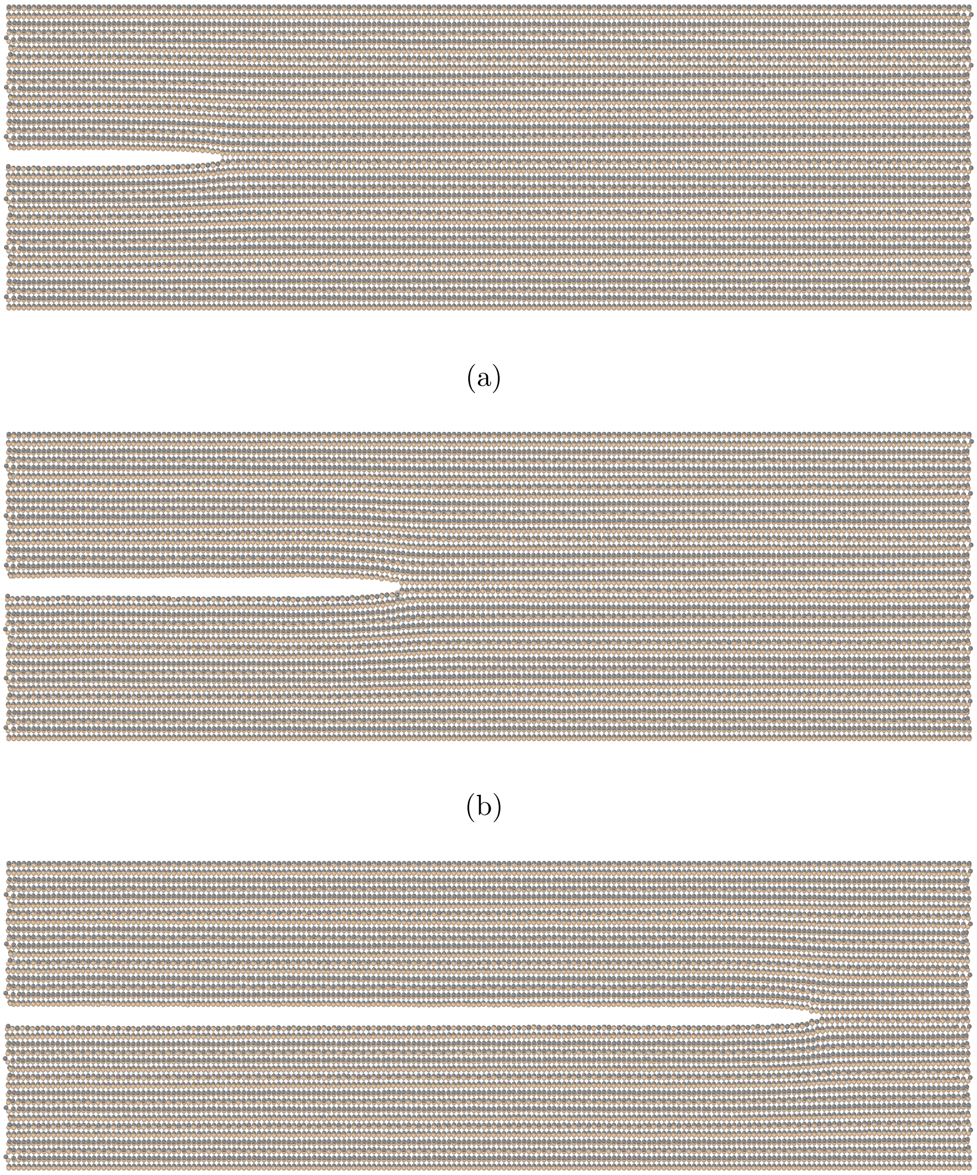

(a)

(b)

(c)

Figure 3.10: Frames taken from a SiC 6H MD crack simulation, with the times at a) 200 fs, b) 1600 fs, and c) 4000 fs. The system had an approximate height of 90 Å and an approximate length of 290 Å. The slab had a cleavage plane along the (0001) plane, and it was modelled with the screened Tersoff potential [47], near 300 K within the *NVE* ensemble using velocity Verlet dynamics. The dynamics showed a brittle response as seen in the experiments by Sernicola *et al.* [1].

Polytype	Method	Environmental Passivation	2γ [$\mathrm{J\,m^{-2}}$]
3C*	Isolated		4.55
3C	Isolated		8.42
6H	Standard		7.68
6H	Standard	Yes	-
6H	Isolated		7.26
6H	Isolated	Yes	0.35

Table 3.2: Surface energy values for two surfaces, 2γ, from DFT using the PBE exchange correlation functional, for the SiC 3C (111) surface and SiC 6H (0001) surface. Two methods to obtain the surface energy were used: the standard method, where the surface energy is an average surface energy across both surfaces in a slab system; and the *isolated* method, where the surface energy was computed for individual surfaces in a slab system. For the standard method, 2γ is simply two times the standard surface energy. For the isolated method, 2γ was computed as the sum of the two isolated surface energies. For each method, the surfaces were also passivated with hydrogen. The 3C surface energy of $4.55\,\mathrm{J\,m^{-2}}$, labelled 3C*, was computed by Abavare *et al.* [110].

method, where the surface energy is an average surface energy across both surfaces in a slab system; and the isolated method, where the surface energy was computed for individual surfaces in a slab system. Since two surfaces are created during fracture propagation, twice the surface energy, 2γ, was considered. For the standard method, 2γ is simply two times the standard surface energy. For the isolated method, 2γ was computed as the sum of the two isolated surface energies. For each method, the surfaces were then passivated with hydrogen, in order to computed the passivated surface energies. The surface energies are summarised in Table 3.2.

Abavare *et al.* computed the isolated surface energies for the SiC 3C (111) surfaces. In order to compare the method used by Abavare *et al.* with the method used here, the isolated surface energy for the 3C polytype was calculated with the method used here. It was not possible to reproduce the $2\gamma = 4.55\,\mathrm{J\,m^{-2}}$ obtained by Abavare *et al.* for the 3C polytype. The method used here produced a $2\gamma = 8.42\,\mathrm{J\,m^{-2}}$. The differences between the calculation by Abavare *et al.* and the ones conducted here could be due to differences in the parameters used in the DFT simulations, such as the exchange correlation functions and the pseudopotentials. However, alternate studies showed similar energies for the 3C polytype compared to the values reported here, giving reassurance on this method [47, 108].

Twice the isolated surface energy of $2\gamma = 7.26\,\mathrm{J\,m^{-2}}$ was found to be in good agreement with twice the standard surface energy of $2\gamma = 7.68\,\mathrm{J\,m^{-2}}$. This agreement shows that the isolated method works and that it is reasonably accurate for calculating the surface energies of individual isolated surfaces. This gives confidence that the method can be used for calculating the surface energy of environmentally passivated isolated surfaces. Environmental passivation of the systems yielded significantly lower surface energies compared to the non-passivated surface energies. For the standard method, the difference in the systems' energies was smaller than the achieved energy convergence tolerance. In other words, the energies were not converged enough to produce a sensible result. Therefore, this result was excluded from the comparison. The environmental passivation of the isolated systems found a $2\gamma = 0.35\,\mathrm{J\,m^{-2}}$. This is significantly lower than that of non-passivated surfaces. A surface energy at this value would significantly lower the fracture energy. This would allow the crack to propagate much more easily compared to propagation near non-passivated surfaces.

Surface Termination

When creating a surface in the [0001] direction, the stacking sequence of the 6H crystal gives rise to three inequivalent terminations. The surface energies for each plane, for two exchange correlations are tabulated in Table. 3.3. The mean surface energy and its standard error for two surfaces, for the LDA exchange correlation is $2\gamma = (8.58 \pm 0.04)\,\mathrm{J\,m^{-2}}$ and for the PBE exchange correlation is $2\gamma = (7.71 \pm 0.04)\,\mathrm{J\,m^{-2}}$. The three planes are close to degenerate in regards to the surface energy, and both exchange correlation functionals have a standard error less than $0.05\,\mathrm{J\,m^{-2}}$.

Temperature Effects

The effects of temperature were calculated using empirical force fields to calculate the temperature dependent contributions to the ground state surface energy using the frozen phonon method. Results from both the harmonic approximation and quasi-harmonic approximation, for each potential, are shown in Fig. 3.11. There was less than 4 % decrease at 1000 K compared to

Termination	2γ [$\mathrm{J\,m^{-2}}$] LDA	2γ [$\mathrm{J\,m^{-2}}$] PBE
a	8.51	7.65
b	8.68	7.81
c	8.55	7.68
Mean	8.58	7.71
Standard Error	0.04	0.04

Table 3.3: DFT surface energy values for two surfaces 2γ for the SiC 6H (0001) surface, of two exchange correlation functionals LDA and PBE. Due to the SiC 6H stacking sequence, there are three inequivalent termination surfaces, that can arise when creating a surface in the [0001] direction. The mean surface energy and its standard error are also tabulated.

the zero temperature surface energy and thus a marginal decrease at 300 K. This is a smaller change in the surface free energy than what Leung *et al.* reported for the 3C polytype [108].

While computing a DFT-level accurate free energy would be possible [101], the results of the empirical force fields show that there was not a significant decrease in the surface energy at 300 K and therefore there is unlikely to be a significant decrease with DFT. Thus, for this work, the temperature of the system was expected to only have a marginal effect on the surface energy.

Surface Energy

The computed surface energy for two surfaces was $2\gamma = (8.15 \pm 0.44)\,\mathrm{J\,m^{-2}}$. This is an average of the two DFT results across the two exchange correlations. The error estimate includes: a deviation of $\pm 0.43\,\mathrm{J\,m^{-2}}$ between the two exchange correlations, an uncertainty of $\pm 0.04\,\mathrm{J\,m^{-2}}$ in the exact termination surface, and a numerical convergence error of $\pm 0.1\,\mathrm{J\,m^{-2}}$. The error shown here is an underestimate of the actual error that could be possible with a DFT based result. Different exchange correlation functionals will likely give different energies. The aggregate error from testing many of them would lead to a better error estimate. The MM accuracy temperature effects could not be added to the DFT calculated surface energy. DFT accuracy temperature effects is possible and would provide another source of error.

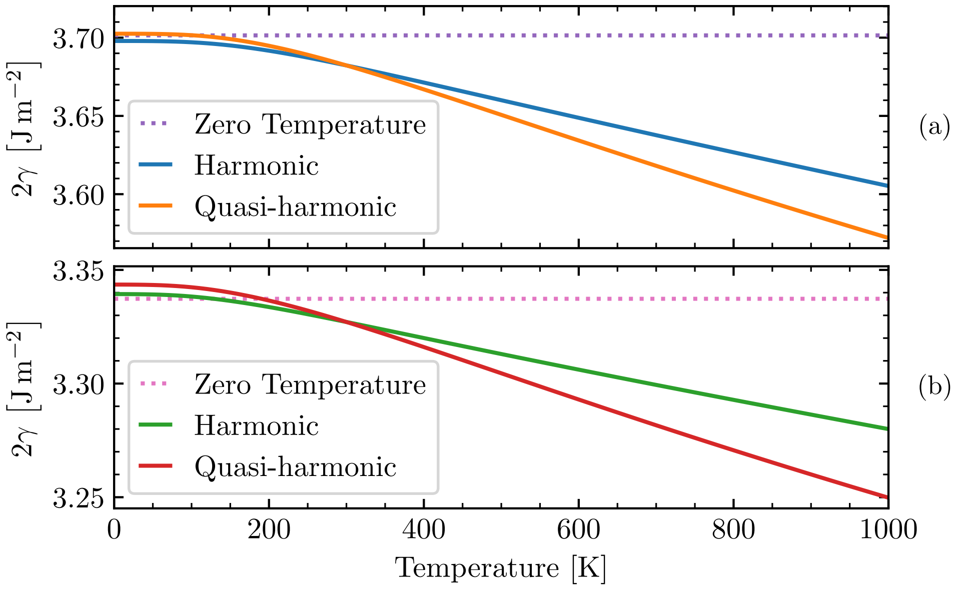

Figure 3.11: Finite temperature surface energies for two surfaces, 2γ, for the SiC 6H (0001) surface, which was computed via the frozen phonon method. The systems were modelled with empirical potentials, which were a) the Tersoff screened potential, and b) the Erhart and Albe screened potential [47]. The zero temperature surface energy, along with the the *harmonic* and the *quasi-harmonic* approximations of the surface energy are shown.

Method	Polytype	Description	Lattice Constant a [Å]	Lattice Constant c [Å]	Reference
DFT	6H	LDA	3.05	15.02	[1]
DFT	6H	PBE	3.09	15.19	[1]
DFT	3C	LDA	4.34		[47]
MM	6H	Tersoff S.	3.06	14.97	
MM	3C	Tersoff S.	4.32		[47]

Table 3.4: Computed lattice constants, a and c, for the SiC 6H unit cell and SiC 3C unit cell. Results from the DFT and MM methods are shown. *Tersoff S.* is the Tersoff screened potential. LDA and PBE are the DFT exchange correlation functionals.

The computational results for twice the surface energy, 2γ, are tabulated in Table 3.5, and visually shown with the experimental results in Fig. 3.9. The lattice constants are tabulated in Table 3.4.

Fracture Toughness

The elastic constant matrix was computed for both exchange correlation functionals, and they were

$$\begin{aligned} C_{\text{LDA}} = &\begin{bmatrix} 523.38 & 104.64 & 59.32 & 0.01 & 0.00 & 1.70 \\ & 525.15 & 61.46 & 0.01 & -0.01 & 0.05 \\ & & 565.24 & 0.01 & -0.01 & 1.85 \\ & & & 166.22 & 1.00 & 0.01 \\ & & & & 164.87 & 0.00 \\ & & & & & 208.41 \end{bmatrix} \\ &\pm \begin{bmatrix} 7.95 & 2.48 & 1.86 & 0.21 & 0.46 & 0.58 \\ & 5.54 & 1.41 & 0.93 & 0.30 & 0.79 \\ & & 7.68 & 1.13 & 1.13 & 0.69 \\ & & & 0.01 & 0.05 & 0.42 \\ & & & & 0.05 & 0.43 \\ & & & & & 0.59 \end{bmatrix} \end{aligned} \tag{3.42}$$

and

$$
\begin{aligned}
C_{\mathrm{PBE}} = &\begin{bmatrix}
494.68 & 92.49 & 50.79 & -0.01 & -0.01 & 1.64 \\
 & 496.17 & 52.67 & 0.49 & -0.02 & -0.07 \\
 & & 533.39 & -0.14 & -0.01 & 1.62 \\
 & & & 165.1 & 1.07 & 0.18 \\
 & & & & 167.69 & 0.00 \\
 & & & & & 199.99
\end{bmatrix} \\
&\pm \begin{bmatrix}
7.91 & 2.46 & 1.64 & 0.31 & 0.16 & 0.39 \\
 & 5.68 & 1.25 & 0.28 & 0.20 & 0.91 \\
 & & 7.39 & 0.79 & 0.67 & 0.48 \\
 & & & 2.31 & 0.04 & 0.20 \\
 & & & & 0.05 & 0.07 \\
 & & & & & 0.49
\end{bmatrix}
\end{aligned}
\tag{3.43}
$$

for LDA and PBE respectively. The values are given in GPa and the matrix after the ± are the errors associated with each component. The Young's modulus was calculated for both exchange correlations, and they were $(553.00 \pm 7.21)\,\mathrm{GPa}$ for LDA and $(524.00 \pm 7.02)\,\mathrm{GPa}$ for PBE.

In this stable fracture growth, $G_c = 2\gamma$ and thus the fracture toughness, $K_c = \sqrt{G_c E'}$, was calculated. The Poisson's ratio was computed and found to be small, it was 0.094 and 0.086 for LDA and PBE respectively. Thus, the difference in the effective Young's modulus between the plane stress and the plane strain cases was small. Therefore, the plane stress case was used to compute the fracture toughness. The fracture toughness was calculated to be $K_c = (2.10 \pm 0.08)\,\mathrm{MPa}\sqrt{\mathrm{m}}$. This is similar to the reported value for the polytype 3C, a $K_c = 2.0\,\mathrm{MPa}\sqrt{\mathrm{m}}$, by Leung *et al.* [120]. The fracture toughness values are displayed in Table 3.5.

3.4.3 Discussion: Experimental and Computational

This section compares the methods and results obtained from the *in situ* fracture experiments with that of the computational surface energy calculations.

The experimental fracture energy, G_{c}, is lower than that of twice the computational surface energy, 2γ, $(5.95 \pm 1.79)\,\mathrm{J\,m^{-2}}$ and $(8.15 \pm 0.44)\,\mathrm{J\,m^{-2}}$ respectively. The DFT based error is an underestimate as it only includes a

Method	Polytype	Description	2γ or G_c $[\mathrm{J\,m^{-2}}]$	K_c $[\mathrm{MPa}\sqrt{\mathrm{m}}]$	Reference
Experiment	6H	Microscale	5.95 ± 1.79	1.80 ± 0.26	[1]
Experiment	6H	Macroscale	16–25	3.3 ± 0.2	[118, 119, 121]
DFT	6H	LDA	8.58 ± 0.04	2.18 ± 0.03	[1]
DFT	6H	PBE	7.71 ± 0.04	2.01 ± 0.03	[1]
DFT	6H	Combined	8.51 ± 0.44	2.10 ± 0.08	[1]
DFT	3C	LDA	8.34		[47]
DFT	3C	PBE	8.40	2.00	[108]
MM	6H	Tersoff S.	3.71	1.37	
MM	3C	Tersoff S.	3.70	1.36	
MM	3C	Tersoff S.	3.70		[47]

Table 3.5: Fracture energy, G_c, twice the surface energy, 2γ, and fracture toughness, K_c, of the SiC 6H (0001) surface and the equivalent SiC 3C (111) surface. Results from different experimental methods and different computational methods are shown. *Tersoff S.* is the Tersoff screened potential. LDA and PBE are the DFT exchange correlation functionals.

few sources. Further sources of error could arise from the slight asymmetrical loading seen in the experiments and stress due to surrounding material which was not present as strain or stress in the computational cells.

Growth of a crack due to corrosion is referred to as stress-corrosion cracking. The process of corrosion takes finite time. In the case of brittle fracture, fracture propagation is relatively fast, and thus it is unlikely that there would be sufficient time for the reaction to take place and effect further propagation or play a significant role. The experimental chamber was not expected to have a significant concentration of hydrogen, due to the vacuum required for SEM studies. To confirm the lack of hydrogen and dismiss a slower process of stress-corrosion, the loading wedge was held still for up to five minutes and no observable increase in the crack length was observed. Thus, no stress-corrosion cracking was observed.

The closely related 3C polytype is known to have some surface reconstructions in the presence of additional molecules such as H_2 or O_2. For surface reconstruction to affect the fracture energy it must occur near instantaneously, i.e. the barrier to creation should be much smaller than $k_\mathrm{B}T$. However, due to the lack of environmental particles in the experimental chamber, as well as surface geometry optimisations showing no reconstructions, the surface energy is taken to be that of the as-cleaved surface.

Furthermore, upon resuming the displacement of the loading wedge, there was no significant change to the fracture energy. Therefore, the effects of hydrogen termination, or surface reconstruction, are not relevant and can be dismissed as the energies are significantly lower than that of the fracture energy measured from the experiments or the computational results.

The effects of temperature on the computational system were marginal. If appropriate DFT studies were performed, the difference due to temperature would likely be of a similar magnitude and account for a few percentage drop of the surface energy. The change in the surface energy due to temperature alone is not enough to be able to match the experiment with the computational results.

The difference in energies could partly be due to surface imperfections, which was not considered here. Further work into a fully dynamical fracture propagation simulation at a quantum-mechanical level may provide further insight into the bond breaking process revealing further differences which are not apparent in the static method employed here.

3.5 Conclusion

Fracture propagation of the SiC 6H polytype along the (0001) plane was performed computationally and experimentally. Fracture energies and surface energies were computed from dynamical experiments and static DFT computations, respectively.

Fracture experiments and MD fracture simulations showed brittle cleavage. The experiment involved *in situ* wedging of a DCB with a controlled displacement profile, which showed crack extension over a substantial time. This resulted in a relative slow and stable crack growth, with extension in the order of a few micrometres over hundreds of seconds. This allowed the comparison of the experimentally measured fracture energy to static DFT calculations of the surface energy. DFT ground state energies were computed for a slab and bulk system. The DFT calculations also accounted for surface reconstruction, surface termination, and surface passivation.

The experimental fracture energy is lower than that of twice the computational surface energy, $(5.95 \pm 1.79)\,\mathrm{J\,m^{-2}}$ and $(8.15 \pm 0.44)\,\mathrm{J\,m^{-2}}$, respectively. Although not exactly the same, the values shown here are in much greater agreement than previous literature.

The method employed in the experiments improved upon previous studies of fracture. It allows for the study of fracture at the micro-structural length scale, which leads towards the possibility of optimisation of materials with specific boundaries and microstructures. Static DFT calculations produced similar results. This provides confidence in DFT simulations, as well as confidence to move investigations towards larger timescales and length scales, such as simulations of dynamical fracture systems and surface energies of geometries with interfaces.

4 Energy Paths for Crack Propagation

Parts of this chapter are in preparation for publication in the following article: Patel, P., Buze, M., Pastewka, L., Braun, J., Ortner, C. & Kermode, J. R. *Atomistic Modelling of Fracture with Nonlinear Elastic Boundary Conditions (In prep.)*

4.1 Introduction

The inherent process of fracture propagation requires an input of energy into the system in order to overcome the electronic bonding of atoms. A large enough external load applied to a fractured system will drive the crack forward [122].

At the continuum scale, Griffith showed that a crack will propagate given that the strain energy release rate is greater than the energy required to create the surfaces [6]. However, the discrete nature of atomistic sites within a material modifies the barrier for fracture propagation. At the continuum scale the crack tip can be stable for any crack length. At the atomistic scale the crack tip can not simply advance in a continuous manner. Instead, the crack tip is stable only at discrete sites, and as such it advances in discrete steps as bonds ahead of the crack tip are broken. This effect is referred to as *lattice trapping* [123, 124]. Within the regime of lattice trapping, these discrete sites are separated by an energy barrier. The energy barrier to crack advancement is the minimum energy required to break the bonds ahead of the crack tip and advance to the next stable site.

Practically all systems have complex energy landscapes, with many local minima and saddle points across the landscape. Further complexity can arise when considering the temperature, pressure, interaction environments, etc. Thermal excitations can cause a crack system to overcome the barrier. Environmental conditions can modify the barrier, such as oxygen molecules inducing stress corrosion cracking in silicon [63].

A previous study on silicon required a method using two modelling techniques of different length scales to accurately predict lattice trapping [125]. In this chapter two approaches to obtain energy barriers and explore the lattice trapping range are described. Here, single scale atomistic methods are developed in an attempt to reduce the complexity and simplify the process to investigate lattice trapping. The methods compute ground state energies with the use of interatomic potentials. The ground state energy is used because the results can be considered as the minimum energy required for fracture propagation. The idea is that future work could be performed with more accurate ground state energy methods, such as DFT, to provide details of the energy landscape. Temperature effects could also be investigated, with the use of kinetic Monte Carlo (KMC) methods using the barriers to simulate larger timescales [126].

4.2 Background

4.2.1 Energy Barriers

A system under internal or external forces can undergo a change, which causes the system to go from one stable state to another. A system typically sits in one energy minimum, the additional energy moves the system into another minimum. The energy required to move from one minimum to another minimum is the *energy barrier*. The reverse process is sometimes called the *healing barrier*. A schematic of the energy profile is shown in Fig. 4.1.

The critical points of an energy path are the energy barrier, E_{b}; the difference in energy minima, ΔE; and the healing barrier, E_{h}. These are given by

$$\begin{aligned} E_{\mathrm{b}} &= E_{\mathrm{s}} \quad - E_{\mathrm{m}_1}, && (4.1) \\ \Delta E &= E_{\mathrm{m}_1} - E_{\mathrm{m}_2}, && (4.2) \\ E_{\mathrm{h}} &= E_{\mathrm{s}} \quad - E_{\mathrm{m}_2}, && (4.3) \end{aligned}$$

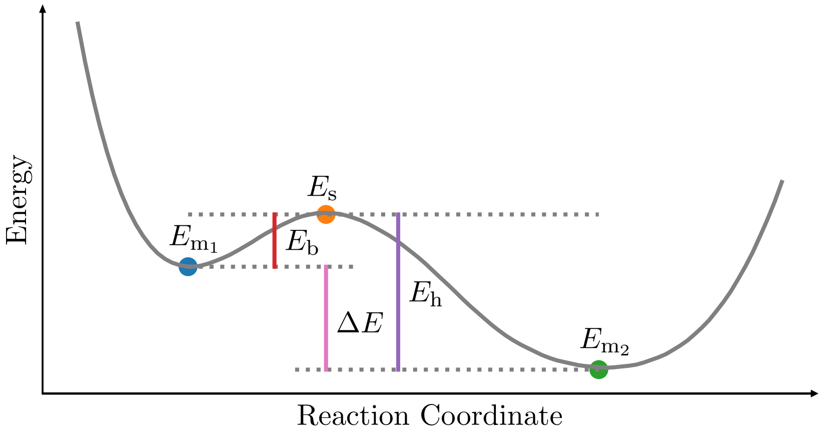

Figure 4.1: Schematic of an energy profile with respect to a reaction coordinate. The minima, E_{m_1} and E_{m_2}, and the saddle point, E_{s}, of the energy profile are labelled. The energy barrier, E_{b}, is the minimum amount of energy required to move the system into the next minimum and is defined as $E_{\mathrm{s}} - E_{\mathrm{m}_1}$. The difference in energy minima, ΔE, is defined as $E_{\mathrm{m}_1} - E_{\mathrm{m}_2}$. The healing barrier, E_{h}, is defined as $E_{\mathrm{s}} - E_{\mathrm{m}_2}$.

where E_{m_1} and E_{m_2} are the initial and final state minima; and E_{s} is the saddle point of the energy profile. The energy barrier represents the minimum amount of energy required to transition into the next minimum, with respect to a reaction coordinate or collective variable. A reaction coordinate, or collective variable, represents the system as a single variable, and it helps describe the transition the system undergoes. The difference between energy minima represents the energy lost, or gained, by the system during the transition.

E_{m_1} and E_{m_2} are the minimum energy of the system at which atoms at the crack tip can be considered bonded and unbonded, respectively. Therefore, E_{b} is the minimum input energy required to allow the system to transition into its next minimum, i.e. minimum energy required to break the bond.

For a sufficiently large system under load at the critical stress intensity factor, K_{c}, the minima in the energy barrier profile to progress a crack are equal in energy. This signifies that within the system there is translational symmetry regarding fracture propagation.

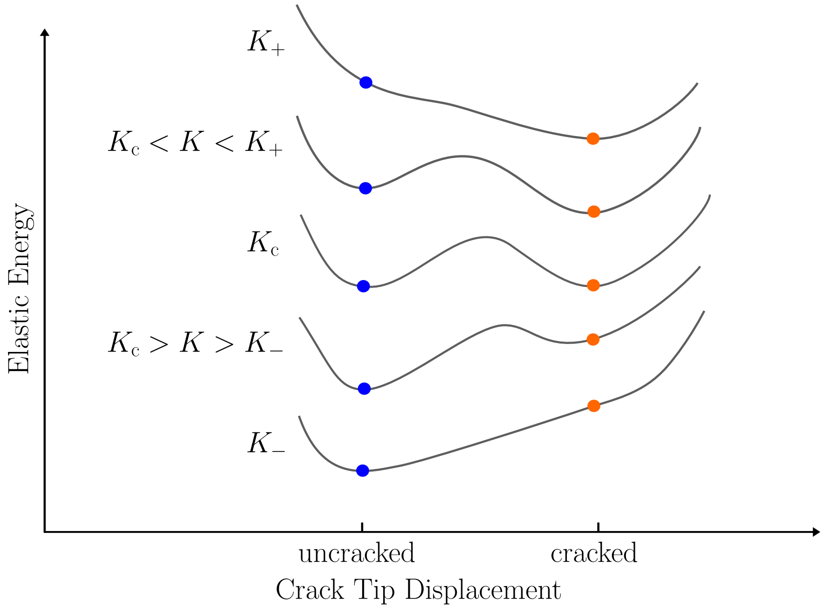

Figure 4.2: Schematic of the lattice trapping range [124]. Multiple energy profiles as a function of crack advancement for different K values are shown. For high K, $K > K_+$, the cracked state is globally stable and the crack opens. For low K, $K < K_-$, the uncracked state is globally stable and the crack closes. At $K = K_c$ the states are of equal energy and is separated by a finite barrier.

4.2.2 Lattice Trapping

Griffith's criteria demonstrates that there exists a critical stress intensity factor, K_c, for which the crack system is stable. As such, for $K < K_c$ the crack retreats and for $K > K_c$ the crack advances, where K is the stress intensity factor of the system. However, Griffith's approach applies to the continuum description of fracture where the crack can continuously advance through the material.

Fracture systems with an atomistic description have atoms at particular, discrete sites. Bulk materials are periodic in nature; thus, crack advancement can be considered as advancing through a grid of discrete points. This gives rise to a range of stress intensity factors for which the system is stable [123]. This effect is known as *lattice trapping*. The system gets trapped, which results in no advancement until enough energy is provided. The range for which K is trapped is represented as

$$K_- < K_\mathrm{c} < K_+, \tag{4.4}$$

where K_- and K_+ are the lower and upper bounds respectively. Beyond the trapping range, for $K < K_-$ the system retracts and for $K > K_+$ the system advances [124]. A schematic of the energy profiles of a system at different K values is shown in Fig. 4.2. Since the lattice trapping range arises from the periodicity of the the potential, the potential itself affects the range. For short ranged potentials the lattice trapping range is larger than those of longer ranged potentials [124]. The lattice trapping for fracture is analogous to the Peierls barriers for dislocations [127].

4.2.3 Pseudo Arc-length Continuation Method

The energy landscape of a fractured system is complex, with many minima and saddle points. It is possible to obtain the configurations of these stationary points without the need to simulate overcoming energy barriers.

The solutions to a system of nonlinear equations can often not be found analytically. Instead, numerical approaches are used to compute solutions. Here, a numerical continuation method is used to compute the family of solutions of the system, the method is known as the *pseudo arc-length continuation* method. An overview of the scheme is outlined below [128, 129]. A schematic of the pseudo arc-length continuation scheme is shown in Fig. 4.3.

Consider a system of nonlinear equations, $G(x)$, with solutions of the form

$$G(x^*) = 0, \tag{4.5}$$

where $G : \mathbb{R}^N$ and is sufficiently smooth; x is a vector of length N; and x^* is a solution. Computing the solutions to G can be complicated and can be simplified via the introduction of a real parameter, λ, which forms a system of parameter-dependent, or parametrised, nonlinear equations. Subsequently, the solutions to G are of the form

$$G(x^*, \lambda^*) = 0, \tag{4.6}$$

where (x^*, λ^*) is a solution. It can be shown that if (x^*, λ^*) is a solution then

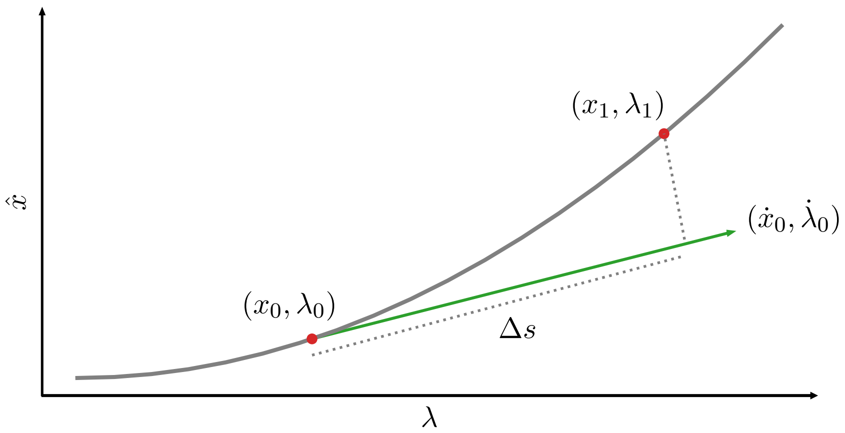

Figure 4.3: Schematic of the pseudo arc-length continuation method [128]. Suppose (x_0, λ_0) is a solution to the nonlinear system of equations, $G(x)$. It is possible to find a nearby solution (x_1, λ_1). Computing the direction vector, $(\dot{x}_0, \dot{\lambda}_0)$, and taking a step, Δs, in the direction of the direction vector achieves an approximation to (x_1, λ_1). The approximation is then iteratively solved to find the actual solution (x_1, λ_1).

there exists a unique solution family that pass through (x^*, λ^*) [128].

Suppose a solution, (x_0, λ_0), to $G = 0$ is already computed. To perform a continuation method a direction vector is required. A *natural continuation* method can be used to find more solutions of G. However, there are several issues with this method, one of which is that it fails to continue at *limit points* [129], which are also known as *fold bifurcations* [130]. A fold bifurcation is when a stable solution and unstable solution *collide* and disappear [130]. This occurs when the solutions cross over from being stable to unstable and from unstable to stable; the overlap is the fold bifurcation.

In the context of this work fold bifurcations were expected [131, 132]. This is due to the periodic nature of the lattice and thus the periodic nature of the real parameter that is chosen, K. For a sufficiently large system, the lattice trapping range does not vary as the crack advances, and thus K remains within a bounded region. This results in folds within the set of solutions, and thus overlapping sets of solutions in K space, of the nonlinear system of equations. Therefore, the solutions remain bounded with respect to K space. The pseudo arc-length continuation method is used as it overcomes some shortcomings of the natural continuation method [129].

Consider parametrising the solution with an arc-length parameter, s, and an arc-length condition

$$||\dot{x}_n||^2 + ||\dot{\lambda}_n||^2 - 1 = 0, \tag{4.7}$$

where $\dot{x}$ and $\dot{\lambda}$ are the derivatives with respect to s of x and λ respectively [129]. The index n denotes the iteration step. The derivative of $G(x,\lambda) = 0$ with respect to the arc-length parameter is

$$\frac{\mathrm{d}}{\mathrm{d}s} G(x_n, \lambda_n) = G_{x_n}\dot{x}_n + \dot{\lambda}_n G_{\lambda_n} = 0, \tag{4.8}$$

where the subscript, x or λ, on G denotes the partial derivative of G with respect to that subscript at the location of (x_n, λ_n). The derivatives $\dot{x}$ and $\dot{\lambda}$ can then be written as

$$\dot{x}_n = -G_{x_n}^{-1} G_{\lambda_n} \dot{\lambda}_n, \tag{4.9}$$

$$\dot{\lambda}_n = \pm \frac{1}{\sqrt{||G_{x_n}^{-1} G_{\lambda_n}||^2 + 1}}. \tag{4.10}$$

This forms the first direction vector, i.e. when $n = 0$.

The pseudo arc-length continuation method solves the following equations

$$G(x_n, \lambda_n) = 0, \tag{4.11}$$

$$(x_n - x_{n-1})^* \dot{x}_{n-1} + (\lambda_n - \lambda_{n-1})\dot{\lambda}_{n-1} - \Delta s = 0, \tag{4.12}$$

for $n \geqslant 1$. This is solved using Newton's method, such that

$$\begin{pmatrix} G_{x_n} & G_{\lambda_n} \\ \dot{x}_{n-1}^T & \dot{\lambda}_{n-1} \end{pmatrix} \begin{pmatrix} \Delta x_n \\ \Delta \lambda_n \end{pmatrix} = - \begin{pmatrix} G(x_n, \lambda_n) \\ (x_n - x_{n-1})^* \dot{x}_{n-1} + (\lambda_n - \lambda_{n-1})\dot{\lambda}_{n-1} - \Delta s \end{pmatrix}, \tag{4.13}$$

where Δs can be considered as the step size. Since x_n and λ_n are required, they are first estimated using

$$x_n \approx x_{n,k=0} = x_{n-1} + \dot{x}_{n-1}\Delta s, \tag{4.14}$$

$$\lambda_n \approx \lambda_{n,k=0} = \lambda_{n-1} + \dot{\lambda}_{n-1}\Delta s, \tag{4.15}$$

where $(x_{n,0}, \lambda_{n,0})$ is the approximate solution, and k is the Newton's method iteration step. The arc length system of equations, Eq. 4.13, is then solved iteratively to find (x_n, λ_n). The estimates $x_{n,k}$ and $\lambda_{n,k}$ are updated for each iteration by adding $\Delta x_{n,k}$ and $\Delta\lambda_{n,k}$ to the respective estimate. The iterative algorithm is considered converged when all components of the gradient of the right-hand-side of Eq. 4.13 are below a tolerance. Once converged, this Newton minimisation gives the solution (x_n, λ_n).

For $n \geqslant 1$ the direction vector, $(\dot{x}_n, \dot{\lambda}_n)$, can be obtained via a computationally cheaper method, by solving

$$\begin{pmatrix} G_{x_n} & G_{\lambda_n} \\ \dot{x}_{n-1}^T & \dot{\lambda}_{n-1} \end{pmatrix} \begin{pmatrix} \dot{x}_n \\ \dot{\lambda}_n \end{pmatrix} = \begin{pmatrix} 0 \\ 1 \end{pmatrix} \tag{4.16}$$

which is formed by the derivative of G and the arc length condition [128]. This can not be used to compute the first, $n = 0$, direction vector since it requires the previous, $n - 1$, direction vector. The direction vector is then used to estimate the next solution using Eq. 4.14 and Eq. 4.15. The estimates are then used to start solving Eq. 4.13, for which the actual solution is computed iteratively. The process using Eq. 4.16 can be repeated for all $n \geqslant 1$. This algorithm forms the basis of the pseudo arc-length continuation method. Given an initial starting solution, repeating the continuation scheme for many steps produces the stationary solutions to the given system of equations.

4.2.4 Hausdoff Distance

The Hausdoff distance, d_{H}, is a measure of how far two sets, X and Y, are from each other; in other words, it is measure of how similar, or dissimilar, the sets are [133]. The directed Hausdoff distance, $d_{\bar{\mathrm{H}}}$, is defined as

$$d_{\bar{\mathrm{H}}}(X, Y) = \max_{x \in X} \Big\{ \min_{y \in Y} \{ d(x, y) \} \Big\}, \tag{4.17}$$

where $d(x, y)$ is the Euclidean distance, which is defined as

$$d(x, y) = \sqrt{\sum_{i=1}^{n} (x_i - y_i)^2}. \tag{4.18}$$

The Hausdoff distance is then defined as

$$d_{\mathrm{H}} = \max\Big\{ d_{\bar{\mathrm{H}}}(X,Y), d_{\bar{\mathrm{H}}}(Y,X) \Big\}. \tag{4.19}$$

Here, the Hausdoff distance was used as a measure to determine how similar one continuation path is to another.

4.3 Methodology

Two different approaches were used to compute the energy barrier of breaking a single bond ahead of the crack tip. The first approach constrained the bond at various lengths, that were expected as the bond went from a bonded to an unbonded state. The energy of the atoms that formed the bond were computed at each length to form an energy profile. The stationary points were calculated, to then obtain the energy barrier. The second approach computed the family of stationary points of the system. The energy barrier was then computed using the stationary points.

4.3.1 Static and Flexible Boundaries

The energy barrier to break the next bond along in the direction of the advancement of the crack was computed on a fractured diamond-structured carbon lattice using a constrained bond approach. In a fracture system, the bond nearest to the crack tip along the crack advancement direction was constrained at various lengths, and then the energy profile was calculated. The screened Tersoff potential was used to model the system as it is known to provide an accurate description of diamond-structured carbon [47].

A carbon crystal of diamond cubic structure was made by repeating the unit cell. The crystal was then orientated to expose (111) surfaces when fractured. The elastic constant matrix was computed, from which the Poisson's ratio, ν, and the Young's modulus, E, were extracted. Twice the ground state surface energy, 2γ, of the (111) cleavage plane was computed. The critical stress intensity factor, K_{c}, was computed using $K_{\mathrm{c}} = \sqrt{G_{\mathrm{c}} E'}$, where $G_{\mathrm{c}} = 2\gamma$. The CLE displacements were generated using ν, E, and K_{c}, and the displacements were applied to the bulk system which created the fractured system. A visualisation of the system is shown in Fig. 4.4. The *boundary* of the system was formed of a region of atoms with a width approximately 4.4 Å measured inwards from the outer edge. The atoms within the boundary region are spatially clamped. The system was then energy minimised to obtain a stable crack configuration.

The next bond, and the corresponding pair of atoms, along the crack advancement direction was found. The separation distance of the atom pair is what was constrained during the procedure. The energy barrier was computed by constraining the separation length, s_i, for a set, S, of varying magnitudes to obtain the energy profile. The bond length of a carbon-carbon pair in a ground state crystal system, using the Tersoff potential, was approximately 1.7 Å. The set of separations, S, had a range of 1.6 Å to 3.2 Å, which translates to approximately 95 % to 188 % of the relaxed bond length.

The potential energy, E, between the atom pair over S can be computed by integrating the force, F, over the separation distance, and this is given by

$$E(s) = -\int_{s_{\text{initial}}}^{s_{\text{final}}} F(s)\, \mathrm{d}s, \tag{4.20}$$

where s_{initial} and s_{final} are the initial and final separation magnitudes, respectively.

The energy profile was computed for two cases: the *static boundary* case, where the boundary atoms remains fixed for each constraint; and the *flexible boundary* case, where the boundary atoms are spatially adjusted for each constraint.

Static Boundary

For each constraint, s_i, the atoms of the selected bond were initially placed to satisfy the constraint. The system was then minimised while maintaining this constraint. The minimisation was performed with the LBFGS method. The forces on this atom pair were calculated. The process was repeated for each separation length. Then the integral of the forces was calculated to obtain the energy. The boundary of this approach remains fixed for all constraints and minimisations. This will be referred as the *static boundary* case.

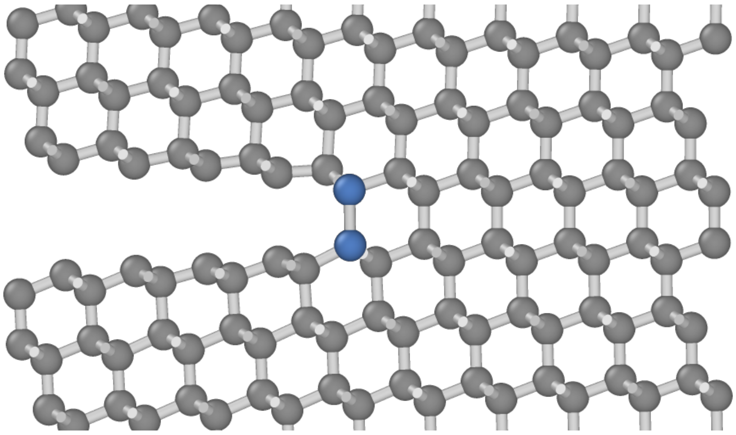

Figure 4.4: A mode I fractured diamond-structured carbon system, which is open along the (111) plane. The size of the system is approximately 20 Å by 30 Å or the system has a radial size of approximately 10 Å. The pair of atoms that form the bond ahead of the crack tip are highlighted in blue. These atoms were constrained at multiple distances to be able to compute the energy profile and thus the energy barrier of the process of breaking a single bond.

Flexible Boundary

A variation to the static boundary was also computed. Here, the boundary was adjusted for each separation length, compared to the static boundary case where the boundary remained fixed. The idea here is that a moving boundary better simulates the advancement of the crack tip. This was expected to result in a faster size convergence when compared to the static case, especially for small systems.

For each constraint, s_i, the atoms were initially placed to satisfy the constraint. The system was then minimised while maintaining the constraint. The minimisation was performed with the LBFGS method. The minimisation caused the abstract crack tip to move. A change in the crack tip suggests that the crack is receding or advancing. This causes extra strain on surrounding atoms which may not be present in larger systems. Thus, to reduce this extra strain, the boundary was updated self-consistently via a fit of the crack tip. The crack tip was fitted using a least squares fit between the actual displacements and a new set of CLE displacements. The fit minimises the difference between a new set of CLE displacements with a new crack tip and the target displacements. The boundary was updated in an iterative approach. First, a crack tip position was fitted to the minimised constrained configuration. The boundary of the minimised constrained configuration was adjusted such that it matched the boundary of the fitted CLE displacements. The process was repeated until the difference between the current fitted crack tip and the fitted crack tip of the last iteration was below a tolerance.

The whole process was repeated for each separation length. The integral of the forces was calculated to obtain the energy. This will be referred as the *flexible boundary* case.

Energy Barrier

Once the potential energy profile was computed the barrier was extracted. A seventh order polynomial was fitted to the energy points; seventh order polynomials were found to best match the energy profiles. The high order of the polynomial allowed enough degrees of freedom to ensure: that the values of minima and saddle points were satisfied; and that the gradients were also satisfied.

The critical points were computed, and the local minima, E_m, and saddle point, E_s, were found. The energy barrier, E_b, and change in the energy minima, ΔE, were calculated.

Varying Stress Intensity Factor

The procedures of computing the energy profile for breaking a single bond along the crack advancement direction was repeated for a range of stress intensity factors. Increasing the stress intensity factor, K, and computing the energy barrier should reveal the load at which the barrier goes to zero, K_+.

In theory, $K_\pm$ are points along a continuous range of K. In practice, it is only possible to compute with discrete values of K. This led to unusable energy profiles. For $K > K_+$ or $K < K_-$, i.e. the load being too high or too low, multiple bonds can break, or heal. At $K = K_+$ or $K = K_-$ there is only one minimum and thus no saddle point to be found between the two minima. As K approaches K_+ or K_- from within the lattice trapping range, one of the minima and the saddle point turn into inflection points at K_+ and K_-. In other words, for K_+ the energy barrier is zero and the healing barrier exists, and for K_- the reverse is true. Further issues arise, for K close to $K_\pm$ and beyond the lattice trapping range, i.e. $K + \epsilon > K_+$ and $K - \epsilon < K_-$,

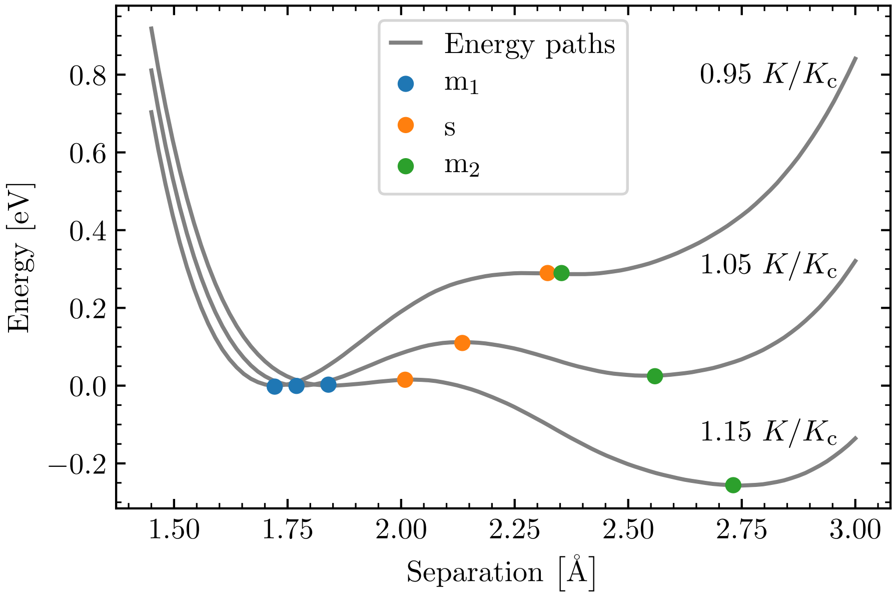

Figure 4.5: The critical points for different energy paths, for breaking a single bond ahead of the crack tip are shown. The critical points were computed by finding the stationary solutions to a seventh order polynomial which was fitted to the energy profiles. The first minimum, m$_1$, the saddle point, s, and the second minimum, m$_2$, are coloured blue, orange, and green respectively. The energy profiles, coloured grey, are of a bond breaking process in a fracture system of diamond-structured carbon which was open along the (111) plane. The system had a size of approximately 20 Å by 30 Å and was periodic in the third dimension. It was modelled with the Tersoff potential. The different curves are for different stress intensity factors, which are labelled normalised with respect to K_c, where K_c is the critical stress intensity factor computed via surface energy calculations.

where ϵ is small. The inflection point is shifted, in comparison to K_+ and K_-, or simply cease to exist.

Profiles that had multiple broken, or healed, bonds were removed, since the energy profile of a single bond is the target of this method. Profiles that exhibited the other issues were filtered out, as it was not possible to obtain reliable stationary points. Smaller increments, or decrements, of K would increase the number of reliable profiles and help to further explore the lattice trapping range; however, this would increase the computational cost.

Each suitable profile was fitted with a seventh order polynomial to obtained the energy barriers. The stationary points of the suitable energy profiles were calculated. The energy barrier, E_b, and the change in energy minima, ΔE, were calculated for each energy profile, i.e. for several K values. The set of energy barriers essentially gives the energy barrier of the system as a function of the stress intensity factor, $E_{\mathrm{b}}(K)$. Example profiles and stationary points are shown in Fig. 4.5.

The solution at which $E_{\mathrm{b}}(K) = 0$ is K'_{+}. The prime superscript is used to denote the value of K obtained via the energy profiles. Similarly, the solution at which $\Delta E(K) = 0$ is K'_{c}. The prime superscript is used to distinguish between the value of K obtained via the energy profiles compared to the non-prime K_{c} which is computed via surface energy calculations. In theory $K'_{\mathrm{c}} = K_{\mathrm{c}}$. $\Delta E(K)$ was fit with a linear function, and $E_{\mathrm{b}}(K)$ was fit with a quadratic function; their respective solutions were then computed. For the quadratic case the relevant solution was chosen. K'_{+} existed beyond the range of calculated K values, and thus the K'_{+} was an extrapolated value.

System Size Convergence

As with any simulation with a finite system size, a convergence test of the property of interest with respect to system size is crucial, and it is particularly important given the long range stress fields found in fractured systems.

The objective is to identify the minimum system size required for a precise calculation without excessive computation. Here, the convergence of the energy barrier and difference in the energy of the minima were calculated.

Since the energy was computed from the force on the atom pair alone, the energy could be compared across system sizes, regardless to the changing number of atoms across different systems size or varying boundaries. The energy barrier of breaking a single bond is a local property. This is in contrast to methods which compare total energy, in which the number of atoms need to be accounted for. Systems with varying boundaries are not comparable since the total energy varies too much to see small energy changes such as breakage of a single bond.

Therefore, the computed energy profiles were easily compared across system sizes. $\Delta E(K)$ was fit using a linear function and $E_{\mathrm{b}}(K)$ was fit using a quadratic function to find K'_{c} and K'_{+}, respectively. This was repeated for several system sizes.

4.3.2 Strained Surface Energy

K_c was computed via $K_\mathrm{c} = \sqrt{2\gamma E'}$, where 2γ is twice the surface energy. The surface energy has been computed on unstrained systems. A fracture system is under strain, and thus local differences in the strain at the exposed surface could lead to differences in K_c. Thus, the surface energy as a function of strain was computed.

To gain a better understanding a simplified model was used. Here, a 2D hexagonal lattice was used. A stable crack system with a radial size of 25 Å was generated, such that the crack tip was stabilised at the centre of the system. An IBS potential with a cutoff of 1.4 Å was used to model the system.

Atomistic Strain Components

The Young's modulus is a measure of the constant of proportionality between the stress and the strain of a system under uniaxial deformation. Stress is inherently a continuum concept since it is a force per unit area. However, Zimmerman *et al.* showed that it is possible to consider stress as an atomistic concept [134]. While it is possible to compute atomistic stresses, it is relatively difficult to compute compared to the computation of atomistic strain. Strain is easier to compute; thus, to gain an understanding on the effect of uniaxial deformation, the atomistic strain was investigated.

Local atomistic strain components were computed to investigate the strain profile experienced by atoms as a function of distance from the crack tip.

The strain tensor was computed by comparing the deformed positions of the system under uniform strain with the non-deformed positions. The local strain on each atom is then calculated by minimising the mean-square difference between the displacements of neighbouring atoms relative to the atom itself and the relative displacements that they would have if they were uniformly strained. This process was originally described by Falk and Langer [135]. The local strain of each atom along the crack surfaces were computed.

Strained Surface Energy

The local surface energy as a function of strain along the crack face was computed. First, the local strain of each atom along the crack surface was computed as detailed above. For surface energy calculations two systems are required, the bulk and slab system. A unstrained surface energy was computed. Then the strained surface energies were computed. Each local strain value from the crack system was applied to both bulk and slab systems, where all atoms and the enclosing cell were deformed. The surface energy as a function of strain was computed. The strain varies as a function of distance from the crack tip, and as such the surface energy as a function of strain along the crack surface was computed.

The effect of energy minimisation was also considered. The minimisations were performed with the FIRE algorithm. An unstrained, energy minimised surface energy was computed. Then, the bulk system was strained and then minimised. The minimised bulk system was used to make the surface system, which was then strained and then minimised. The shape and size of the cell were not geometrical optimised, in order to maintain the strain on the system. Only the atomic positions were energy minimised. This was repeated for all strains along the crack surface.

4.3.3 Pseudo Arc-length Continuation Scheme

The pseudo arc-length continuation method was used to extract configurations of the stationary points of the fracture system. These configurations were then used to compute an energy path for different stress intensity factors. The method can obtain a family of stationary points and thus obtain configurations which were within the lattice trapping range $K_- \leqslant K \leqslant K_+$.

The continuation scheme constantly changes the boundary of the system. Thus, the commonly calculated fracture system properties such as the strain and the total energy of a system can no longer be compared across different system sizes. The energy barriers are somewhat local, i.e. independent from the boundary, and thus they can be compared and converged with respect to system size.

Continuation Path

The continuation method is described in Sec. 4.2.3. In the context of a fracture system and the stationary points of interest, the nonlinear system $G(x, \lambda)$ was formulated to be: G as the gradient of the energy, E, of the fracture system, i.e. $G = \nabla E$; λ as the stress intensity factor, K; and x as a modification to the positions of a fracture system, Δu.

The energy of the system is dependent on the positions of the atoms. A fracture system with CLE displacements is formed of the lattice positions, a, and the CLE displacements, u_{CLE}, with the atomic positions written as $a + u_{\text{CLE}}$.

Here, K has been introduced as an explicit variable of the energy and so the energy is now also a function of K. Hence, the CLE displacements are rewritten as a function of K, $u_{\text{CLE}}(K)$. For simplicity of notation, let $u_{\text{CLE}}(K) = u_K$. The atomistic positions of a fractured system with CLE displacements can be written as $a+u_K$, and any modification to those positions can be written as $a + u_K + \Delta u$.

The solutions to ∇E are of the form

$$\nabla E(\Delta u^*, K^*) = 0, \tag{4.21}$$

where $(\Delta u^*, K^*)$ is a solution. Thus, atomistic positions for a solution, which are the energy minimised positions, will be written as $a + u_{K^*} + \Delta u^*$. For simplicity of notation, let the energy minimised displacements be written as $u_{K^*} + \Delta u^* = \hat{u}_K$.

The continuation path is formed of a set of the solutions of Eq. 4.21. To test the method, a simple fractured 2D hexagonal lattice was used. The lattice had an equilibrium bond length of 1.0 Å. The atoms were modelled using a LJ potential, with a cutoff of 1.4 Å. The unit cell was repeated until a circular system of a particular radius, with an additional region of two and a half times the potential cutoff, was generated. The additional region acts as the clamped boundary, i.e. was fixed during minimisations, to mitigate finite size and surface effects. The CLE displacements were calculated and applied to the circular crystal; a schematic diagram is shown in Fig. 4.6. The stress intensity factor, K, Young's modulus, E, and Poisson's ratio, ν, were computationally chosen to ensure an equilibrated stable crack system, such that the crack tip is at the centre of the domain. The system was also

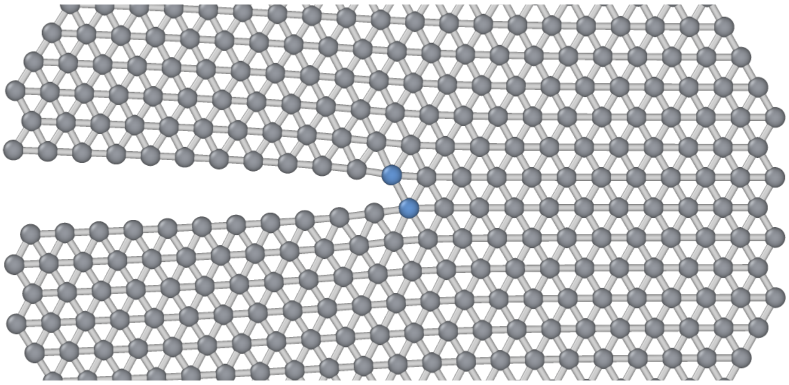

Figure 4.6: A 2D hexagonal lattice, with an equilibrium bond length of 1.0 Å, which has the CLE displacements applied producing a mode I fracture system. The pair of atoms that form the bond ahead of the crack tip are highlighted in blue.

restricted to movement of positions in the $x - y$ plane. The crack tip was initially positioned halfway between two layers of atoms, i.e. midway along the vertical bond perpendicular to the crack propagation direction.

The continuation path was calculated. The pseudo arc-length procedure was repeated for many iterations to obtain several families of stationary points such that the periodic nature of the path could be seen. To compute an energy barrier a minimum of a set of stable, unstable, and stable segments are required. A visualisation of a path is shown in Fig. 4.7, with the solid lines representing the stable solutions and the dashed lines representing the unstable solutions. The system undergoes a fold bifurcation as it transitions from the stable segment to the unstable segment, and similarly from the unstable segment to the stable segment.

The stable segment corresponds to the range of K at which the system is at an energy minimum. The unstable segment corresponds to the range of K at which the system is at a saddle point in the energy landscape. The fold bifurcation characterises that the different segments overlap one another in the K dimension. Thus for a particular K, the points on the stable and unstable segments represent the energy landscape for fracture propagation for a given load applied to the system.

For each step, i.e. computation of a new solution, in the continuation path a crack tip was fitted to the corresponding configuration. The fit generated new sets of displacements while adjusting the tip position to match the configuration's displacements. Only atoms within an annular region around

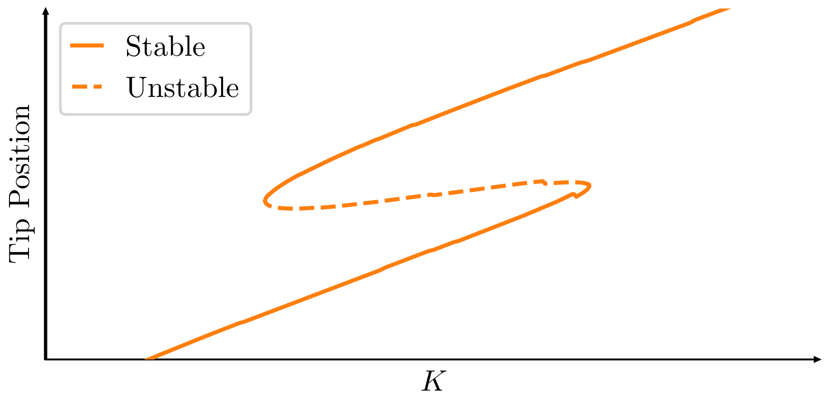

Figure 4.7: Schematic of a continuation path of a fracture system using the pseudo arc-length continuation scheme. The *stable* segment and *unstable* segment represents the minima and the saddle points of the system respectively. The system undergoes a fold bifurcation as it transitions from the stable segment to the unstable segment, and similarly from the unstable segment to the stable segment. Discontinuities near the junction of the stable and unstable segments can exist in this visualisation as the crack tip position is fitted.

the crack tip position were used. Further description on the fitting of the crack tip is given in Sec. 4.3.4.

Lattice Trapping

The range of K for which the unstable and stable segments overlap represents the lattice trapping regimes of fracture propagation. The K at the transition from a stable segment to an unstable segment is the K_+ bound, and the K at the transition from an unstable segment to a stable segment is the K_- bound. If the extrema of the range of K translates to the K_- and K_+ properties, then K_c is likely to exist within this range.

The range of stationary solutions of an unstable segment represents the range of K for which there is a forward, or backward, energy barrier that involves that particular bond along the crack front. For a given configuration extracted from the continuation path, any K outside the range of the K_- and K_+ of the nearest unstable segment could lead to several bonds breaking, or healing.

Extract a Configuration

A configuration's energy is largely determined by the load applied to the system. The larger the load, the larger the displacements and thus the higher the energy. Furthermore, the outer regions of the system contain more atoms and thus changes to them influence a greater change in energy, compared to changes within the inner regions.

A bond breaking process near the crack tip leads to small energy differences between atoms near the crack tip. These differences lead to a small change in the total energy of the systems. In order to detect these small energy differences, through computation of the total energy, the boundaries of the configurations should be the same. This requires a constant K across the configurations.

In practice, the continuation path was computed on discrete points which resulted in a finite set of K points. These points were not necessarily the same across all segments. A configuration within a segment for a particular K was approximated using a nearby configuration that existed within the continuation path.

To extract a single configuration with a target K, K_t, along a particular segment along the continuation path, the configuration with the most similar K to K_t, K_s, was chosen as a starting point. The changes in the positions during that configuration's energy minimisation, $\hat{u}_{K_\mathrm{s}} - u_{K_\mathrm{s}} = \Delta u^*_{K_\mathrm{s}}$, were extracted. New CLE displacements were generated using K_t, and the changes due to minimisation for the K_s system were added on. Thus, the target configuration's minimised displacements, $\hat{u}_{K_t}$, were approximately

$$\hat{u}_{K_t} \approx u_{K_\mathrm{t}} + \Delta u^*_{K_\mathrm{s}}. \tag{4.22}$$

This was an adequate approximation, as the step size in the pseudo arc-length continuation scheme was small.

Energy Barrier

The energy barrier of breaking a single bond was calculated and compared across the systems.

The energy barrier of a single bond breaking process was extracted from the continuation path. The stationary solutions represent the local minima

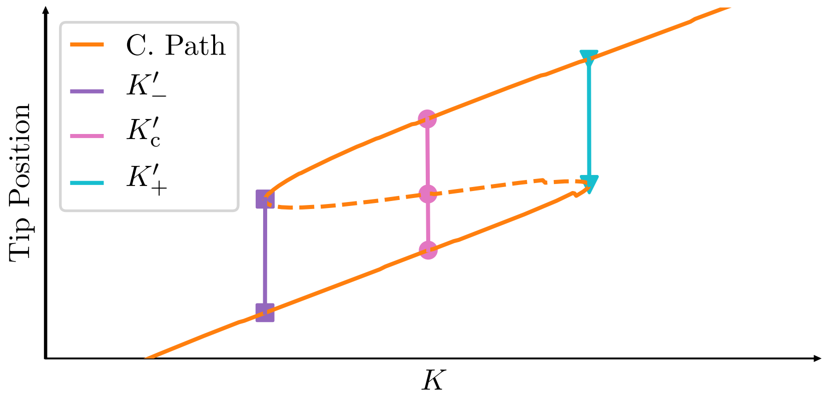

Figure 4.8: Continuation path of a fracture system using the pseudo arc-length continuation scheme, coloured orange. For select stress intensity factors, K, the continuation path is marked with the configurations required to compute the energy path to break a single bond ahead of the crack tip. The markers denote the configurations extracted from the continuation path. The lines between the markers represent configurations between the nodes, which in practice are interpolated.

and the saddle points of the system for different K. In other words, given a particular K, it represents the key points of the energy landscape that a crack will propagate through or near. An energy barrier requires two minima and a saddle point, where the saddle point exists between the two minima. Thus, three configurations of a particular K were extracted from the continuation path. The configurations were from a continuous set of stable-unstable-stable segments.

A schematic of the solutions used to generate the configurations are shown as nodes in Fig. 4.8, which have been overlaid onto a continuation path. K'_c is the value of K at which the configurations corresponding to the two minima are expected to be of equal energy. The prime superscript is used to distinguish between the value of K obtained via the energy profiles compared to the non-prime K_c which is computed via surface energy calculations. The K'_c pathway is shown with nodes marked as circles in Fig. 4.8.

Then, a pathway of configurations was generated. The configurations extracted from the continuation path form the start, middle, and end of the pathway. The intermediate configurations were linearly interpolated using the extracted configurations. A schematic pathway is shown as a solid line connecting the nodes in Fig. 4.8.

The energy of each configuration along the path was calculated, which gave the energy path. A crack tip was also fitted to each configuration. While the configurations from the continuation path are at their minimal energies, the interpolated configurations are not minimised before computing the energy. Thus, the energy pathway can not be considered as a minimal energy pathway. This approach gave an upper bound on the energy pathway. The energy barrier, healing barrier, and the energy difference between the two minima were calculated from the energy pathway, and are noted as E_{b}, E_{h}, and ΔE respectively. The full energy path was not needed to calculate the barriers. However, inspection of the fully calculated pathway can show that the path has the expected profile for an energy barrier, as well as provide overall information about the path.

Energy paths and associated properties were computed for a range of K values within the interval of $K_{-} \leqslant K \leqslant K_{+}$. A schematic of the expected K_{-} path and the K_{+} path are shown in Fig. 4.8, which are labelled as K'_{-} and K'_{+} respectively. The paths appear to only have two configurations that have been extracted from the path. However, close to the region where the segments change from the stable to unstable, and vice versa, the nodes are very close together and visually overlap one another.

E_{h} and E_{b} do not exist for K_{-} and K_{+} respectively. Near K_{-} the second minimum is at a higher energy than the first minimum. Near K_{+} the second minimum is at a lower energy than the first minimum. Thus, for some K within the interval of $K_{-} \leqslant K \leqslant K_{+}$ the energy difference between the minima is zero, $\Delta E = 0$.

K'_{c} was expected to be near the midway point along the unstable segment. Since the lattice trapping range does not have to be symmetric, K'_{c} is interpolated using nearby pathways. The pathway which crosses the midway point along the unstable segment is an approximate K'_{c}, which is hereafter referred to as $\tilde{K}'_{\mathrm{c}}$.

The exact K at which the energy difference is zero, K'_{c}, was linearly interpolated between the two paths whose $\Delta E = +\epsilon$ and $\Delta E = -\epsilon$, where ϵ is small. Since the minima at K'_{c} are equal, then $E_{\mathrm{h}} = E_{\mathrm{b}}$. Then, similar to how ΔE was computed, the E_{b} at K'_{c} was linearly interpolated from the closest two paths.

System Size Convergence

The errors on the system properties were compared to a reference system with a radial size of 128 Å. The boundary region of this system extended beyond the given radius, and thus the stated radial sizes are of the region in which atoms were free to move.

The reference system was initialised with CLE displacements which had a crack tip in the centre of its domain. The same parameters were used to generate the displacements for the smaller systems. However, for the smaller radii systems, the K was not optimal for that particular radius. Thus, the smaller minimised systems where initialised with crack tips that were not localised in the centre of their systems. Continuation paths for system sizes of 8 Å, 16 Å, 32 Å, and 128 Å were computed.

E_{b}, K'_{c}, and the bounds $K'_{\pm}$ were computed for each system size. The error computed of these properties were with respect to the respective values computed on the reference system. The Hausdoff distance was also computed with respect to the reference system; the distance is a measure of the similarity of the continuation paths.

4.3.4 Fitting the Crack Tip

The crack tip is a point in space, which in general is not located on any atom. During the construction of a fracture system a crack tip is specified. It defines the central radial point to form the CLE displacements. During minimisations or dynamics, the crack propagates through the material. In order to track its progress the CLE displacements are used to estimate the new crack tip position as if the system where to be constructed at that location. A schematic of a fitted crack tip is shown in Fig. 4.9.

Atomistic CLE displacements require: the stress intensity factor, K; the Young's modulus, E; the Poisson ratio, ν; and the radial positions and angles of the atomic positions. The radial positions require a centre point. This centre point is the crack tip.

As a crack system is minimised, or propagates, a new crack tip is formed. The fit is a *least squares* regression which fits a new set of CLE displacements using a new centre point, i.e. crack tip, onto the target displacements. The fit was performed on an annular, or radially small, domain of atoms around a guess of the crack tip. This was done to avoid biases in the fit. The number

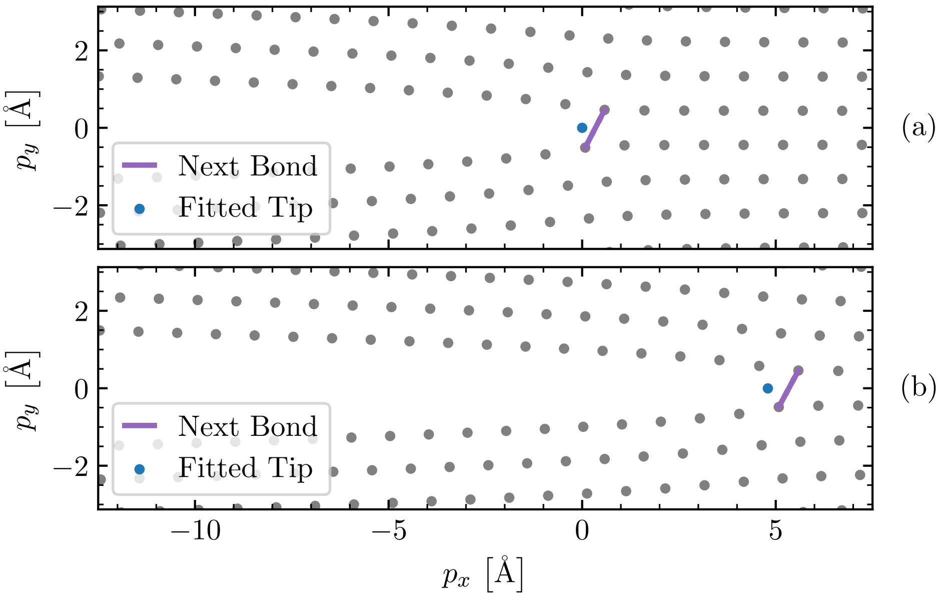

Figure 4.9: An example of a crack system which has advanced from its starting position, a), to a position further along, b). Here, a 2D hexagonal lattice is shown. The positions are plotted relative to the centre point used to generate the CLE displacements. The atoms are coloured grey. The crack tip was fitted by comparing the system's displacements to that of similar CLE displacements. The next bond along the crack advancement direction can be automatically selected. The bond is coloured purple and labelled *next bond*. p_x and p_y are the components of the atomic positions in x and y respectively, which are plotted relative to the position of the crack tip in a).

of atoms scales with r^2, and so there are many more atoms at further radii than radii closer to the centre point. The displacements of those atoms is also larger compared to those closer to the centre point. These attributes can skew the fit resulting in a crack tip much further ahead than expected. An annulus can be used to avoid atoms close to the centre as their displacements are not so easily captured by the CLE displacements, including these atoms can lead to skews in the fit.

A propagating crack can cause the guess of the crack tip to move beyond the region to which the fit was originally performed on. To accommodate this, the fit was performed twice. The first fit provided a reasonable guess for the crack tip. The fit domain was updated and centred around the first guess. The second fit uses the updated domain for the final fit of the crack tip.

4.3.5 Initial Stress Intensity Factor

The load required, i.e. the stress intensity factor, K, to initialise a stable crack system can be computed using surface energy calculations. An alternative approach is through an iterative approach.

The bulk system was generated by repeating the crystal unit cell. A set of CLE displacements were computed. Atomistic CLE displacements require: the stress intensity factor, K; the Young's modulus, E; the Poisson ratio, ν; and the radial positions and angles of the atomic positions. The radial positions require a centre point. This centre point is the crack tip.

E and ν are material properties. K and the crack tip are the properties related to the crack configuration. The stress intensity factor scales the displacements to produce a wide, or narrow, crack opening. The crack tip dictates the position of the crack.

Simulation domains are finite in size. To avoid edge effects, large system sizes are required. Furthermore, the region of interest, such as defects, should be surrounded by bulk-like material. This is to ensure that the edges do not interact with the defect itself, as it may alter its behaviour. Since most crack systems are not periodic in all directions, it is not possible to use common supercell methods to tackle simulation domain size. Thus, it would be ideal for the crack tip to be positioned well away from the boundary of the system.

In the geometries used here, the centre of the system was used as the location for the crack tip. This meant that any boundary effects were equal on both sides. This was particularly required for small systems, as edge effects are better mitigated in large systems.

Stabilisation of the crack configuration at the crack tip was performed using a trial and error approach. The objective was to find a suitable K for an initial crack tip, such that when the system was energy minimised, the fitted crack tip position remained approximately equal to the initial crack tip, given some tolerance. The minimisations were performed with the LBFGS method.

An initial K was given to determine whether the crack configuration propagated forwards or backwards. Depending on the outcome, the K value was modified and a new attempt was made. Once a bounded region of K existed, the algorithm performed a bisection search within the bounded values of K to find the K value which satisfied the objective. This value of

K was then used in the formulation of the CLE displacements for the crack configuration.

4.4 Results and Discussion

4.4.1 Static and Flexible Boundaries

Energy Barriers

The energy profiles were calculated for several K values around K_c, where K_c was obtained from computing the surface energy of the crystal. The energy profiles of a system are shown in Fig. 4.10 with respect to the separation distance, s, between the atom pair ahead of the crack tip. The energy barrier, E_b, difference in energy minima, ΔE, were calculated for each of the profiles. Their values as a function of a normalised stress intensity factor, K/K_c, are plotted in Fig. 4.10.

The energy profiles and computed energy barriers of Fig. 4.10 show a clear trend that as the stress intensity factor, K, increases, i.e. with an increasing load, the energy barrier reduces to zero. The location of the first minimum shifts in the positive s direction as K increases, as does the second minimum. The saddle point shifts in the negative s direction. The linear fit and quadratic fit are suitable for ΔE and E_b, respectively. The fit functions are shown in Fig. 4.10.

System Size Convergence

For each system size, the fitted functions were used to calculate K'_c and K'_+. K'_c was calculated at the point where $\Delta E(K) = 0$, and K'_+ was calculated at the point where $E_\mathrm{b}(K) = 0$. Two models were used: the static boundary case, where the boundaries were fixed; and the flexible boundary case, where the boundaries were adjusted to compensate for the moving crack tip. Both properties and models are shown in Fig. 4.11.

For an infinite system, at the critical stress intensity factor, K_c, where $K_\mathrm{c} = \sqrt{G_\mathrm{c}E'} = \sqrt{2\gamma E'}$, the difference in energy of the minima should be zero. E' is the effective Young's modulus. The convergence of K'_c with respect to system size shows: for the static boundary case, this condition is met close to K_c; and for the flexible boundary case, the condition is not met.

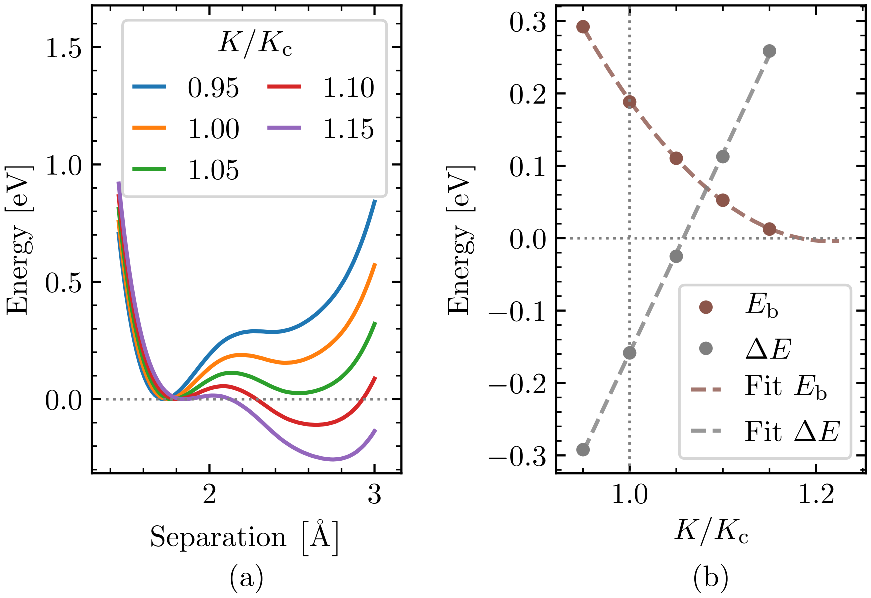

Figure 4.10: Energy properties for breaking a single bond of a fractured diamond-structured carbon system, approximately 20 Å by 30 Å and periodic in the third dimension. It was modelled with the Tersoff potential [47]. The open surfaces were along the (111) plane. These profiles used the *static boundary* method. a) Minimal energy profiles were constructed by computing the energy of the bond while constraining the separation distance between a pair of atoms which formed the bond ahead of the crack tip. The energy profiles for several stress intensity factors, which are shown normalised to K_c, where K_c is the critical stress intensity factor computed via surface energy calculations. b) Energy barriers, E_b, and the difference in the energy of the minima, ΔE, of the energy profiles in a) against the respective normalised K. A linear fit through ΔE and a quadratic fit through E_b are shown.

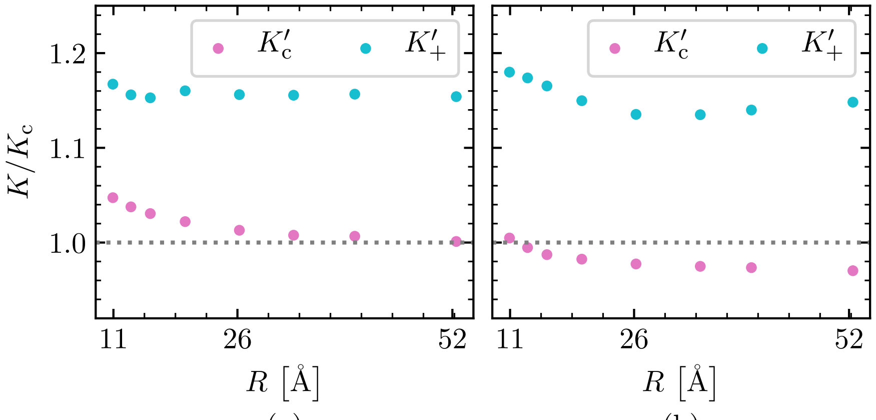

(a)

(b)

Figure 4.11: Convergence of the critical stress intensity factor, K'_c, and the upper bound of the lattice trapping range, K'_+, with respect to radial system size, R. K'_c and K'_+ were computed from energy profiles of breaking a single bond ahead of the crack tip of a fractured diamond-structured carbon system which was open along the (111) plane. The atomic interactions were modelled with the Tersoff potential [47]. The system was modelled with two methods: a) the *static boundary* case and b) *flexible boundary* case. K'_c and K'_+ are shown normalised with respect to K_c, where K_c is the critical stress intensity factor computed via surface energy calculations.

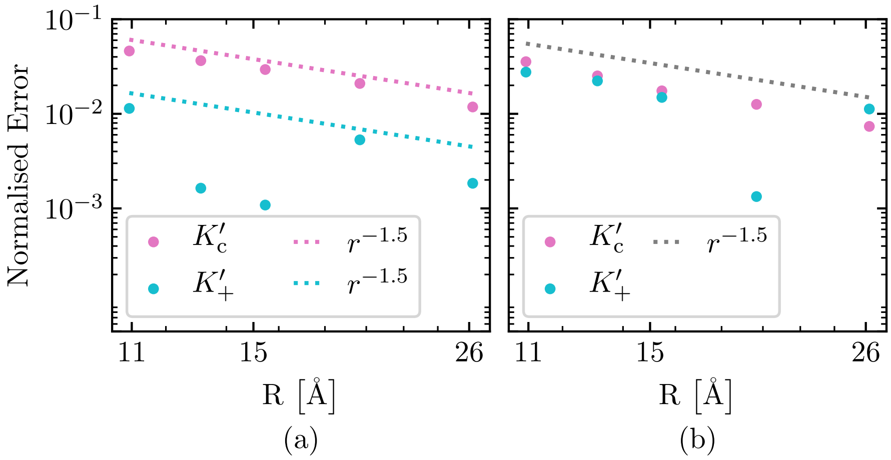

Figure 4.12: Convergence of errors for the critical stress intensity factor, K_c', and the upper bound of the lattice trapping range, K_+', with respect to a reference system with a radial size of approximately 52 Å. The errors have been normalised with respect to the value of that property found in the reference system. K_c' and K_+' were computed from energy profiles of breaking a single bond ahead of the crack tip of a fractured diamond-structured carbon system which was open along the (111) plane. The atomic interactions were modelled with the Tersoff potential [47]. The system was modelled with two methods: a) the *static boundary* case and b) *flexible boundary* case. R is the radial size of the system.

Conceptually the flexible boundary case should be a more realistic model of a fracture system. The boundary was updated to take into account that the surrounding atoms should be displaced further as the crack tip progresses. The finite system size and boundary edge effects may have skewed the energy of the minima compared to larger systems.

The errors of these properties with respect to a reference system is shown in Fig. 4.12. The errors have been normalised with respect to the values obtained from the reference system, which had a radial size of approximately 52 Å. K'_c decays in both boundary methods. The upper bound of K'_+ decays, however the values themselves are less consistent compared to K'_c. Thus, the decay of K'_+ is questionable, particularly for the static boundary case. K'_+ for the flexible boundary case is more consistent; however, the reference system does not resemble an infinite system as K'_c does not equal K_c. In other words, it is not converging to the expected theoretical value.

K_c was computed via $K_\mathrm{c} = \sqrt{2\gamma E'}$, and so the errors could arise from the surface energy or the Young's modulus components. The Tersoff screened potential does accurately describe diamond-structured carbon [47], and so a qualitative description of a fracture system in MM could be feasible. Other errors could be a result of the small finite system size, of which the errors are not evident in the limited size convergence tests performed here. Small system sizes are particularly an issue for longer range potentials, as the effects of interactions are felt over greater distances compared to shorter range potentials. Furthermore, even larger systems are required to mitigate the longer ranged finite edge effects. The limitations in the accuracy of the CLE displacements to represent discrete points is another source of error; this is explored in Chapter 5.

The discrepancy in K_c and K'_c prompted further investigation into K_c, by looking into the surface energy and strain components of E.

4.4.2 Strained Surface Energy

Initial simulations to compute the energy barrier of breaking a single bond in a fractured diamond-structured carbon system, with (111) crack surfaces, displayed a disparity between the critical stress intensity factor, K_c, and the K at which the difference in energy minima was zero, K'_c. Griffith's energy balance for an infinite system states that at a stress intensity factor of K_c

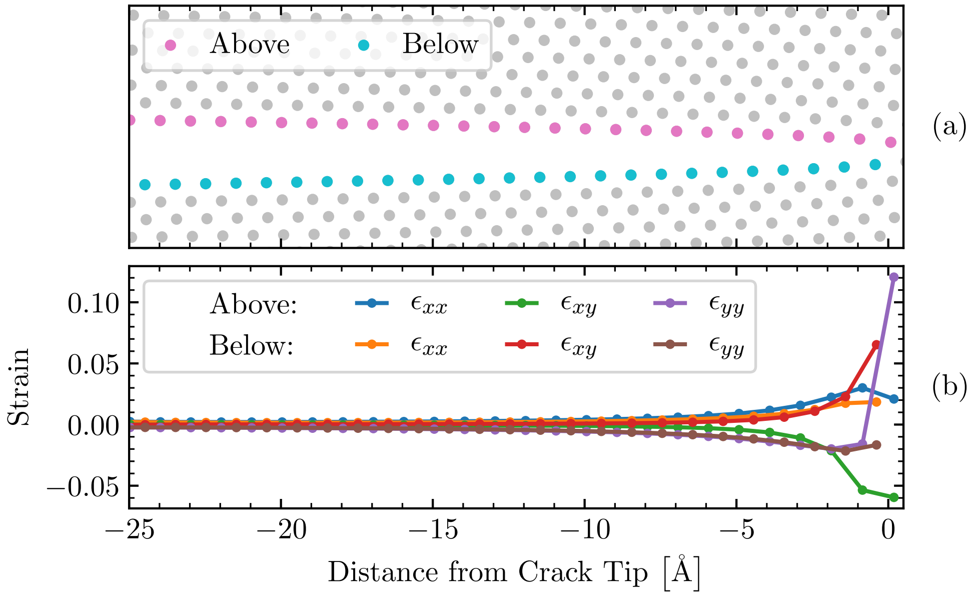

Figure 4.13: Strain components ϵ_{xx}, ϵ_{xy}, and ϵ_{yy} of individual atoms along the two surfaces of a fractured 2D hexagonal lattice modelled with an IBS potential with a cutoff of 1.4 Å are shown in b) with respect to distance from the crack tip. The atoms are categorised by the surface they are apart of, labelled *above* and *below*, as shown in a).

the difference in energy minima is zero.

K_c was computed via $K_\mathrm{c} = \sqrt{2\gamma E'}$ where 2γ is twice the surface energy of unstrained systems. The surface energy as a function of strain was computed. To gain a better understanding the model was simplified to a 2D hexagonal lattice modelled with an IBS potential with a cutoff of 1.4 Å.

Atomistic Strain Components

Fig. 4.13 shows the strain components, ϵ_{xx}, ϵ_{xy}, and ϵ_{yy}, of the atoms on the top and bottom crack surfaces, labelled *above* and *below* respectively. As expected, the strain decays with distance from the crack tip, with the greatest strain found on the bonded atoms near the crack tip, and greater strain in the y direction. The strains with y components are not equal; this is likely due to the asymmetry in the bonds, as they are not parallel to the y axis.

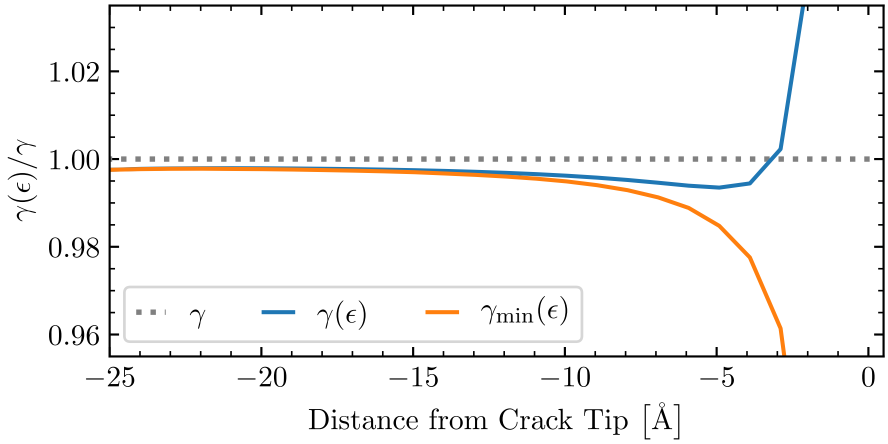

Figure 4.14: Surface energy as a function of the strain tensor, ϵ, as seen along the surface of the crack, with respect to distance from the crack tip. The surface energy of an unstrained configuration, γ, is shown as the dashed line. $\gamma(\epsilon)$ and $\gamma_{\mathrm{min}}(\epsilon)$ are computed with strained configurations where the atomic positions have not been energy minimised and where the atomic positions have been energy minimised, respectively. The strained computational cells remain fixed for both cases. The energies are shown normalised with respect to the unconstrained surface energy, γ.

Strained Surface Energy

The local strain of each atom along the crack surfaces were then used to compute the strained surface energies, for both non-minimised and minimised systems. Unstrained surface energies for both non-minimised and minimised systems were also computed. The computed unstrained surface energies were essentially identical.

The surface energy as a function of strain, or as labelled distance from the crack tip, is plotted in Fig. 4.14. The strain of the system had little affect on the surface energy. Thus, the change in elastic response of the system was deemed to have a small effect on K_{c}. However, it could effect local properties computed near the crack tip, such as energy barriers.

4.4.3 Pseudo Arc-length Continuation Scheme

The pseudo arc-length continuation scheme provided a way to obtain the stationary points of a system given an initial starting condition as a function of the stress intensity factor, K. From the continuation path, energy barriers for specific K were computed. The convergence of the energy barrier at K'_c with respect to system size was calculated.

Continuation Paths

Continuation paths for system sizes of 8 Å, 16 Å, 32 Å, and 128 Å were calculated and are shown in Fig. 4.15. The fitted crack tip position of the reference system at the midpoint of the unstable segment of a particular bond was used as a zero line. The crack tip positions, of all points for all systems, are plotted relative to that value. The continuation parameter, K, was normalised with respect to K_c, which was obtained from a calculation of its surface energy. The fitted crack tip position in the x direction against continuation parameter, K, are plotted for each system size.

The continuation paths show a differing range of the unstable segments overlapping with the stable segment with respect to system size. The larger systems have unstable segments that span a similar range in K as the stable segments, whereas the range in K of the unstable segments in the smaller systems are smaller. This results in the larger systems having an overall smaller range of K for the whole path compared to the smaller systems; the ranges observed were $[0.98K_\mathrm{c}, 1.03K_\mathrm{c}]$ and $[0.99K_\mathrm{c}, 1.47K_\mathrm{c}]$ respectively. This suggests that for small systems, the bounds of the lattice trapping range are overestimated and the size of the lattice trapping range is underestimated. Thus, the error on the lattice trapping range for consecutive bonds gets increasing worse.

In an infinite system, the range of K experienced is expected to be small and around the K_c value indefinitely. The lattice trapping range of the largest system here is only a few percent around K_c, this resembles behaviour expected in an infinite system.

It can be seen that as the system size increases the range of K experienced decreases, suggesting that further increasing the system size would lead to the expected infinite size behaviour. The repeating structure of the continuation path shows the path of stable and unstable regions as the crack advances, with each unstable segment representing another bond along the crack advancement direction.

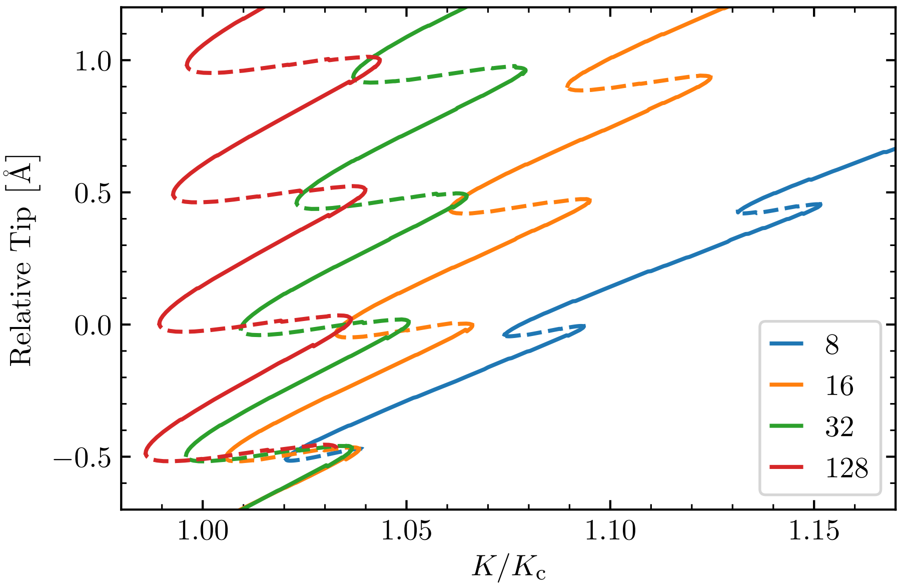

Figure 4.15: Pseudo arc-length continuation paths for a fractured 2D hexagonal lattice, which was modelled with a LJ potential with a cutoff of 1.4 Å. Multiple system sizes defined by their radius are shown and labelled. Each path is plotted as the x component of the fitted crack tip position, relative to the centre of one of the unstable segments in the reference system with a radial size of 128 Å. This unstable segment represents the bond at the centre of the domain. The path is plotted as a function of the normalised stress intensity factor, K/K_c, where K_c was computed with surface energy calculations. The *stable* segments, solid lines, and *unstable* segments, dashed lines, represents the minima and the saddle points of the system respectively.

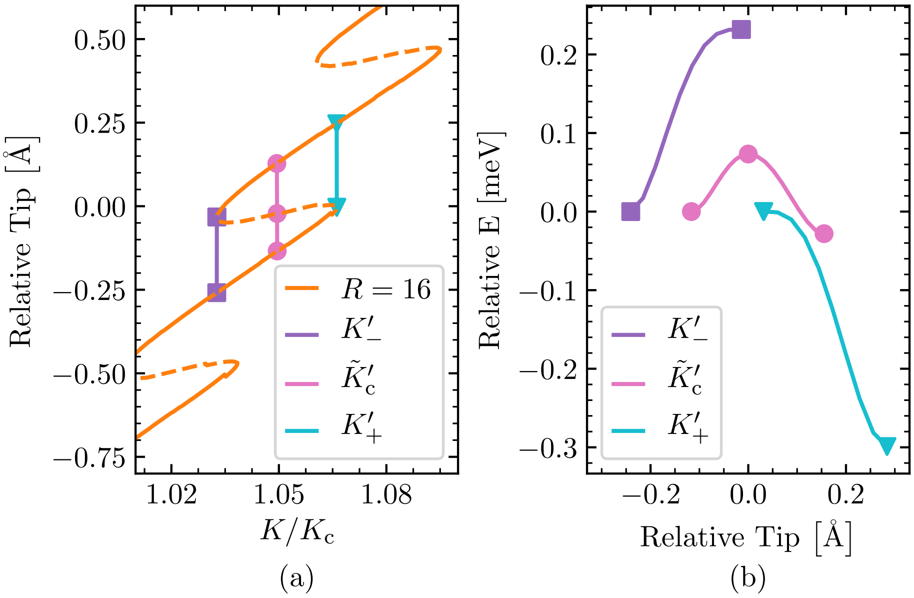

(a) (b)

Figure 4.16: a) Pseudo arc-length continuation path for a fractured 2D hexagonal lattice, modelled with a LJ potential with a cutoff of 1.4 Å. The system had a radial size of 16 Å. The path is plotted with respect to the fitted crack tip positions relative to the same location in the reference system and as a function of normalised stress intensity factor, K/K_c, where K_c was computed using surface energy calculations. The continuation path is marked with the configurations used to compute the energy path to break a single bond ahead of the crack tip, showing select K: K'_-, $\tilde{K}'_c$, and K'_+, which form the lattice trapping range. The solid markers denote the configurations extracted from the continuation path. The lines between the markers represent the interpolated configurations between the nodes. b) The energy profiles as computed using the extracted configurations, plotted as the energy as a function of the relative fitted crack tip position.

Energy Barriers

The energy barrier of a single bond breaking process was extracted from the continuation paths. A bond at a locally similar position across all systems was selected; then the energy barrier of that bond was computed. In Fig. 4.16 a close up of continuation paths around the selected bond, for the system with a radius of 16 Å is shown. Overlaid are a few pathways used to compute the energy barriers. The target K shown are specifically the K'_-, $\tilde{K}'_c$, and K'_+, viewing them left to right on the plot for a single continuation path. The K'_- and K'_+ pathway only have two visible stationary points while the $\tilde{K}'_c$ has three.

In Fig. 4.16 the energy pathways computed from the configurations extracted from the stationary solutions of the target K are shown. The energies for each pathway were adjusted such that the energy of the first minimum is zero. In other words, the energies are relative to that first minimum. In reality, since the boundaries are different the absolute energies were different too. The fitted crack tip positions for each pathway are relative to the fitted crack tip of the configuration extracted from the saddle point of the $\tilde{K}'_{\mathrm{c}}$ path. The tip position of the first minimum for paths were different, with the tip for K'_{-} behind the tip for $\tilde{K}'_{\mathrm{c}}$ and the tip for K'_{+} ahead of the tip for $\tilde{K}'_{\mathrm{c}}$. This is similar behaviour that was seen with the static and flexible boundary methods.

K'_{c} and the energy barrier at K'_{c}, $E_{\mathrm{b}}(K'_{\mathrm{c}})$, were computed for each system. Both the energy barrier errors and the K errors with respect to system size were computed. The system with a radial size of 128 Å was used as the reference system. The errors were also normalised with respect to the values calculated from the reference system and are shown in Fig. 4.17. They both converge with a rate close to R^{-1}. The rates for K'_{-}, K'_{c}, and K'_{+} seen here are slower compared to the error convergence rates for the static and flexible boundary cases seen in Fig. 4.12. However, the values are more consistent and the reference system resembles behaviour expected in an infinite system. Thus, for larger system sizes it is expected that K'_{c} will tend towards K_{c}.

The Hausdoff distance, which obtains the greatest distance from one set to the other, shows that the continuation paths converge to the reference continuation path. The distance in shown in Fig. 4.18.

4.5 Conclusion

Energy profiles and energy barriers, E_{b}, for breaking a single bond along the crack advancement direction were computed for both the diamond-structured carbon (111) plane and the 2D hexagonal lattice. Two methods were used to obtain energy profiles: the static and flexible boundary method, and the pseudo arc-length continuation scheme.

The static and flexible boundary method demonstrated that with a changing stress intensity factor, K, the range of profiles within the lattice trapping range was seen in a fracture model of diamond-structured carbon. Convergence with respect to system size showed that at the critical load, where the

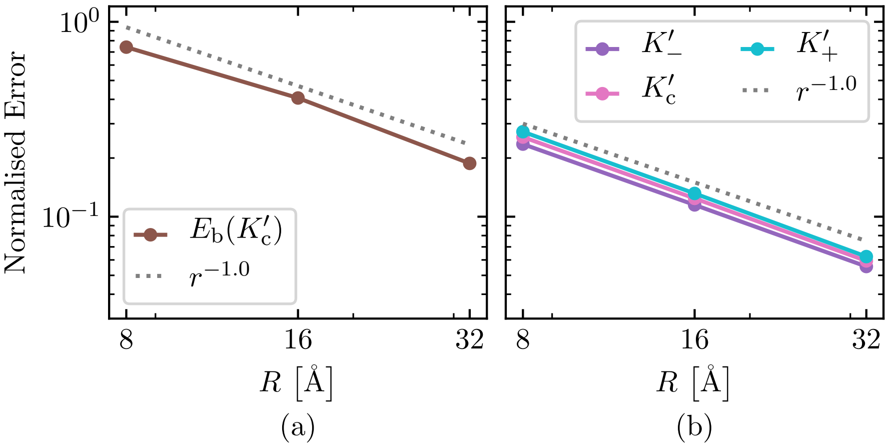

Figure 4.17: a) Normalised energy barriers error at K'_c, and b) normalised errors of key stress intensity factors: K'_-, K'_c, and K'_+. Both a) and b) are converged with respect to system size. The reference system had a radial size of 128 Å. The errors have been normalised with respect to the values calculated for the reference system.

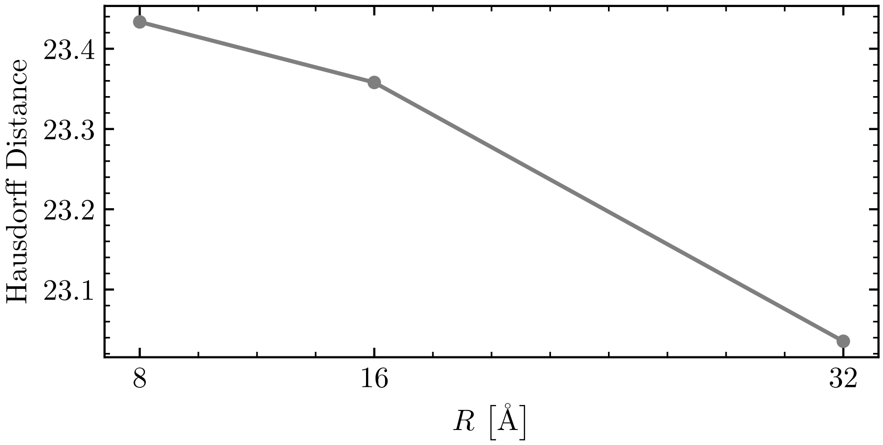

Figure 4.18: Hausdorff distance between the continuation paths of the radially smaller systems and the continuation path of the reference system. The reference system had a radial size 128 Å.

stress intensity factor is equal to K_c, the difference between the energy minima was not zero. This does not match the expected theoretical result. An investigation into the surface energy as a function of strain was performed in an attempt to find the cause of the discrepancy. However, it was found that the elastic response to surface energy has little effect on K_c.

Another method was developed using the pseudo arc-length continuation scheme as a way to obtain the stationary states of the fracture system. The collection of stable and unstable points as a function of the stress intensity factor were computed. These continuation paths showed a glimpse of the complicated energy landscape for fracture propagation given an initial starting point. It was shown that energy profiles can be extracted from the paths, as well as the lattice trapping range. Convergence with respect to system size showed that with increasing system size both the lattice trapping range and E_b at K'_c were converging. Furthermore, the difference between the energy minima at K'_c was tending to zero.

While the continuation scheme allows for computation of the E_b at K_c as well as obtaining the lattice trapping range, the convergence with respect to system size, R, is R^{-1}, and the cost of this method is computational expensive. The cost could be reduced through use of an adaptive step size in the pseudo arc-length continuation method. The next chapter attempts to address the issues of slow system size convergence.

5 Nonlinear Elastic Boundary Conditions

Parts of this chapter are in preparation for publication in the following article: Patel, P., Buze, M., Pastewka, L., Braun, J., Ortner, C. & Kermode, J. R. *Atomistic Modelling of Fracture with Nonlinear Elastic Boundary Conditions (In prep.)*

5.1 Introduction

Fracture propagation processes in materials are ultimately driven by the long range stress field and breakage of chemical bonds near the crack tip. Modelling this requires large and highly accurate atomistic systems to sufficiently capture the processes involved, and thus these simulations are computational expensive.

The continuum fracture theory proposed by Griffith in 1921 [6], is what sets the boundary for atomistic fracture simulations. This continuum model is not entirely adequate for atomistic simulations, and thus introduces an error when describing the atomistic system. The CLE displacements are insufficient when mapped onto atomic positions, particularly in the region near the crack tip where the important chemistry of atomic bonds are involved.

The ultimate goal of atomistic fracture modelling would be to model an infinite atomistic domain. However, that is not possible and so the boundary is matched to the continuum description. In order to match the atomistic and continuum descriptions, the atoms along the boundary of an atomistic simulation are spatially fixed to the continuum description, i.e. the lattice positions plus the CLE displacements, while the other atoms are free to move during a simulation. The energy of a system initialised with atomic positions set according to CLE displacements is not at a minimum. Thus, an energy minimisation must be performed to obtain a stable system in which the crack tip is stationary. If the initial displacements are not close to a minimum, this step can be computationally expensive. This initial minimisation is only the starting point for various fracture simulations, such as computation of barriers and phonon calculations.

The idea presented here pertains to the concept that the atomistic description obtained with the CLE displacements can be improved upon by improving the match between the atomistic and continuum models. Here, the continuum model was modified with information from an atomistic model. This was achieved by a nonlinear continuum model. This approach was tested on a 2D hexagonal lattice with two short-range nearest neighbour potentials, as a proof of concept.

5.2 Background

5.2.1 Pair Constrained Minimisation

The interior-point primal-dual Newton method was used to perform constrained minimisations on the fracture systems. The energy of the system was minimised by means of optimisation of the atomic positions. In the context of the method described in Sec. 2.6.5, $f(x)$ is the total energy and x are the atomic positions.

A constraint, c_i, was used to hold the separation distance, $||x_v - x_w||$, between a pair of atoms denoted with indices v and w, at a predetermined length, $\phi_{v,w}$. The constraint is given by

$$c_i(x) = ||x_{v_i} - x_{w_i}|| - \phi_{v,w}, \tag{5.1}$$

where i denotes each constraint, and v_i and w_i denotes any pair of atoms for each constraint. The constraints were held to within a tolerance of the predetermined length which gave rise to the inequality constraint.

The idea of the interior-point method is to iteratively approach the solution from the interior of the region in n-dimensional space for which the solution holds true. Hence, before minimisation of the atoms the conditions of the constraints must be satisfied. Therefore, the atoms were manually moved to meet the separation constraints.

This method was used to optimise the atomic positions while maintaining the separation of the atoms near the crack tip at a fixed distance. This minimisation was performed to ensure the crack did not advance or retreat.

5.3 Methodology

A fundamental issue when crossing between branches of mechanics is the conversion between the mathematical framework used to describe the problem at hand. Modelling fracture systems often requires going from a continuum description to a discrete description. This transition does not result in a system which is in a minimal energy state. Thus, an energy minimisation is required to alter the system's positions into a well in the energy landscape. This step is computationally expensive and occurs before the start of further investigation into the system. Furthermore, continuum theory often relies on the system having infinite length while atomistic computational domains do not have infinite size. Thus, atomistic domains are limited by their ability to represent the infinite domain, which results in another discrepancy.

To improve the representation of an infinite domain, a non-linear correction term was introduced.

5.3.1 Correction Scheme

The basis of the correction scheme stems from the concept that to achieve an energy minimised system the CLE displacements are applied to the lattice and then minimised. The correction scheme is a modification to the CLE displacements, with the idea that the improved displacements would reduce the number of steps during the minimisation. This is adapted from the work done by Braun *et al.* for dislocations defects [136].

To initialise a fracture system, an atomistic lattice, with positions x, is deformed with the CLE displacements, u_0. The energy of the system is then minimised, which alters the positions. The energy minimised displacements, $\hat{u}$, satisfy

$$\nabla E(x + \hat{u}) = 0, \tag{5.2}$$

where E is the energy of the system. The system is now considered as initialised.

Consider decomposing $\hat{u}$ into two parts, such that

$$\hat{u} = u_0 + u_{\mathrm{c}}, \tag{5.3}$$

where u_{c} are the corrections to the CLE displacements which encapsulate the changes in displacements during the energy minimisation. The displacements are expected to be small, i.e. $u_{\mathrm{c}} \ll u_0$. To maintain the link to the infinite continuum displacements described by Irwin's analytical solution, the atoms towards the boundary match the CLE displacements. Then, the new decomposition satisfies

$$\nabla E(x + \hat{u}) = \nabla E(x + u_0 + u_{\mathrm{c}}) = 0. \tag{5.4}$$

A Taylor expansion of Eq. 5.4 around the point $x + u_0$ gives

$$\begin{aligned}\nabla E(x + u_0 + u_{\mathrm{c}}) =& \nabla E(x + u_0) \\ &+ \nabla\nabla E(x + u_0)(x + u_0 + u_{\mathrm{c}} - x - u_0) \\ &+ \mathcal{O}\big((u_{\mathrm{c}})^2\big).\end{aligned} \tag{5.5}$$

As the u_{c} terms are expected to be small, the higher order terms can be ignored to form an approximation of Eq. 5.4 given by

$$\nabla E(x + u_0 + u_{\mathrm{c}}) \approx \nabla E(x + u_0) + \nabla\nabla E(x + u_0)u_{\mathrm{c}}. \tag{5.6}$$

Let u_{ac} be an approximation to the correction term, $u_{\mathrm{c}} \approx u_{\mathrm{ac}}$, and solve the now approximate equilibrium condition such that

$$\nabla E(x + u_0) + \nabla\nabla E(x + u_0)u_{\mathrm{ac}} = 0. \tag{5.7}$$

Then the approximate correction term is

$$u_{\mathrm{ac}} = -\Big[\nabla\nabla E(x + u_0)\Big]^{-1}\nabla E(x + u_0), \tag{5.8}$$

where $\nabla\nabla E$ is also referred to as the Hessian of the energy. This is equivalent to the high dimensional Newton step given by $x_{n+1} = x_n - \big[\nabla\nabla E(x_n)\big]^{-1}\nabla E(x_n)$ for $n \geqslant 0$. Newton's method can be used to find the solutions to equations of the form $E(x) = 0$. Thus, the correction term is a Newton iteration towards the minimal energy of the system. The approximate correction term, u_{ac}, is applied to the CLE displacements and can be considered as a step in a minimisation scheme.

For dislocation defects it has been shown that corrections to the corresponding CLE displacements can be calculated analytically [136] and similarly for mode III cracks [137]. However, this has not been possible for mode I cracks. Instead, the correction term was estimated using a larger domain. For a domain of interest, d_a, the correction term was computed on another domain, d_b. The size of d_b was sufficiently large such that when the improved boundary is applied to d_a the edge effects of d_b are mitigated for the atoms within the size of d_a.

A computationally intensive part of the correction term is the calculation of the Hessian term. Here, the correction term was further approximated. This was done to test the method with hierarchical modelling in mind, where the correction term could be computed with higher accuracy methods. In the case of DFT based calculations the Hessian of a crystal cell would be cheaper to compute due to its periodic properties, compared to a crack system which has zero or one periodic direction. For simplified systems there is periodicity in the crack plane direction and for realistic systems there is no periodicity. Periodicity allows for the possibility to compute the Hessian on a smaller cell and replicate the values to produce the Hessian of a larger bulk system. Hence, the Hessian term was calculated on the crystal configuration. Thus, Eq. 5.8 becomes

$$u_{\mathrm{ac}} = -\Big[\nabla\nabla E(x)\Big]^{-1}\nabla E(x+u_0). \tag{5.9}$$

Implementation

Typical fracture simulations begin with generating a bulk crystal structure by repeating a unit cell. The CLE displacements are applied to the lattice which generates the crack configuration. The system's energy is then minimised by altering the positions such that the energy is reduced into a local minimum. These steps are shown in Fig. 5.1.

The minimisation step can be computationally expensive and increases in cost with increasing radii. Large radii are needed in fracture simulations to reduce finite-size effects as well as capture long range stress fields.

The correction scheme can reduce the computational cost of the minim-

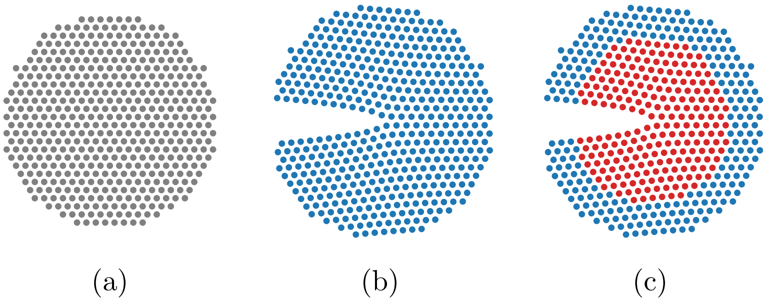
(a) (b) (c)

Figure 5.1: Schematic diagram for generating an initial stable crack configuration. a) 2D hexagonal lattice, with a lattice spacing of 1 Å, made from repeat unit cells. b) System with CLE displacements applied onto the crystal positions. c) Energy minimised system where the atoms coloured red are optimised and the atoms coloured blue are not optimised. The blue atoms remain at their CLE positions.

isation step or reduce the size of the system required. The correction term was computed on a larger system. Although the system was larger, the boundary correction term is simpler to compute than a full minimisation. This larger system will henceforth be referred to as the *boundary system*.

The correction term was computed on the boundary system which had a radius, R_{bc}, defined to be

$$R_{\mathrm{bc}} \geqslant 4R, \tag{5.10}$$

where R is the radius of the system to correct. The boundary system was four times the size of the system to correct. This size was chosen to mitigate edge effects with the region of radius R. The Hessian component of the correction term was calculated on the crystal lattice and the gradient was computed on the crack configuration. Let u_1 represent the corrected displacements, which is given by

$$u_1 = u_0 + u_{\mathrm{ac}}, \tag{5.11}$$

where u_0 are the CLE displacements, and u_{ac} is the correction term. The corrected displacements, generated from the boundary system, were then applied to smaller systems.

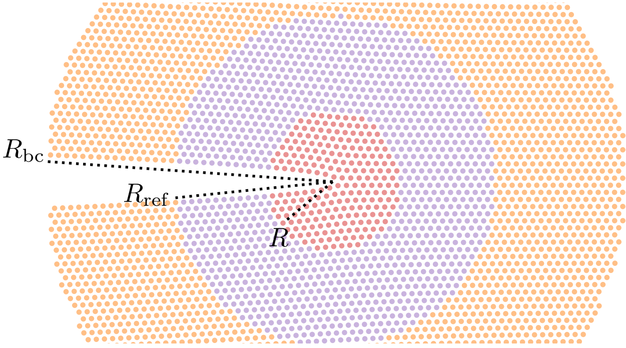

Figure 5.2: Schematic of the systems used to compute the correction term and perform the convergence tests. A crack system of size R_{bc} with CLE displacements was used to compute the correction term, coloured orange. The correction term was applied to the crack system of size R_{ref}. Here, $R_{\mathrm{bc}} \geqslant 4R_{\mathrm{ref}}$. The system of size R_{ref} was then energy minimised and became the reference system for the convergence tests. Multiple systems of size $R \leqslant R_{\mathrm{ref}}/4$ were generated, with both CLE displacements and corrected CLE displacements. The systems of size R were compared with the reference system; this comparison formed the convergence test.

5.3.2 Convergence Tests

Convergence tests with respect to system size were performed to demonstrate the effectiveness of the scheme. The strain error and energy error are detailed here.

Systems

The convergence tests require a set of subsystems and a reference system. The error of the properties measured from the subsystems are compared with the values obtained from the reference system. The radius of the reference system is R_{ref}. The radii of the subsystems are $R_{\mathrm{sub},R}$, where $R_{\mathrm{sub},R} = \{R \leqslant R_{\mathrm{ref}}/4\}$. The correction term was computed on the boundary system which had a radius of R_{bc} where $R_{\mathrm{bc}} \geqslant 4R_{\mathrm{ref}}$. A schematic of the system sizes are shown in Fig. 5.2.

The crystal lattice was built in the same manner for each of the three types of systems. A simple 2D hexagonal lattice with a equilibrium bond length of 1.0 Å was used. The atoms were modelled using either an IBS potential or a LJ potential, with a cutoff of 1.4 Å. The unit cell was repeated until a circular system of a particular radius, with an additional region of two and a half times the potential cutoff, was generated. The stated radius of the system is the size of the region in which the atoms are free to move.

The additional region acts as the clamped boundary, i.e. is fixed during minimisations, to mitigate surface effects. The CLE displacements were applied to the circular crystal, as shown in the schematic diagram in Fig. 5.1. The stress intensity factor, K, Young's modulus, E, and Poisson's ratio, ν, were computationally chosen to ensure the reference system had an equilibrated stable crack system, with the crack tip at the centre of the domain and half way between two layers of atoms. The crack tip and the initial K were calculated using the methods described Sec. 4.3.4 and Sec. 4.3.5 respectively. The system was restricted to movement of the positions to the $x - y$ plane.

The corrected displacements, u_1, were calculated using the boundary system. The reference system was generated, and the subsystems were generated using the reference system. All the systems, the reference system and the subsystems, were energy minimised for both sets of displacements u_0 and u_1. The relaxed set of displacements for each system, $\hat{u}_0$ and $\hat{u}_1$, were composed of

$$\hat{u}_0 = u_0 + u_{\text{res}}, \tag{5.12}$$

$$\hat{u}_1 = u_1 + u'_{\text{res}}, \tag{5.13}$$

where u_{res} and u'_{res} represent the change in displacements during the minimisation, and where the relaxed displacements satisfied

$$\nabla E(x + \hat{u}_0) = 0, \tag{5.14}$$

$$\nabla E(x + \hat{u}_1) = 0, \tag{5.15}$$

respectively. The boundary region of a system was clamped during minimisation; thus, each system's minimised displacements, $\hat{u}_{i,R}$, can be written as

$$\hat{u}_{i,R} = \begin{cases} \hat{u}_i & \text{for } r \leqslant R, \\ u_i & \text{for } r > R, \end{cases} \tag{5.16}$$

where i is either 0 or 1 to denote the CLE or corrected displacements respectively; r is the radius from the crack tip; within the radius R the atoms are free to move during a minimisation; and beyond R the atoms are clamped. The displacements of the clamped atoms match the non-minimised positions.

The minimised displacements for the reference system will be referred to as $\hat{u}_{i,\text{ref}}$.

Each minimisation was a two stage process. First, a pair constrained minimisation where the atoms of the next bond ahead of the crack tip, in the crack advancement direction, were constrained at their initial bond length in the crack configuration. Second, a unconstrained LBFGS minimisation was performed.

Strain Error

The strain on a bond was computed by the change in bond length over the original length. Thus, the strain error is calculated by comparing the length of the bonds across two different configurations, where one configuration is the reference configuration which acts as the true set of positions. The strain across all bonds, Du, of one configuration is

$$Du = \frac{(x+u)_p - (x+u)_q}{l_0} \text{ for } (p,q) \in B, \tag{5.17}$$

where l_0 is the original bond length; (p,q) is an atom pair; $(x+u)_p$ is the position and displacement of atom p; $(x+u)_q$ is the position and displacement of atom q; and B is the set of all bonds. Du is a vector where the number of elements in Du is equal to the number of bonds in the configuration.

The strain error, ρ, is then

$$\rho = Du_a - Du_b, \tag{5.18}$$

where a and b are the displacements of two different systems.

To compute the strain error between systems of different radial sizes, the domain of the smaller system must be extended to the size of the larger system. This was done by extending the boundary region of the smaller system. In other words, the displacements of the smaller system were embedded into a system with a size equal to the larger system. The boundary of this extended system was generated in the same manner as the boundary of the smaller system, i.e. the displacements matched the non-minimised displacements u_0 or u_1. This can also be considered as systems with an equal total size which have different sizes for the fixed boundary regions, and thus the systems have different sizes for the free movement regions.

The strain error of a system before and after minimisation was computed. A system with CLE and minimised CLE displacements with a radial size of 128 Å was compared to a system with minimised CLE displacements with a radial size of 512 Å. The strain error before and after minimisation was calculated for three different potentials: a L-IBS potential, an IBS potential and a LJ potential. All three potentials had a cutoff distance of 1.4 Å.

The strain error with respect to system size was computed for an IBS potential and a LJ potential. The system sizes used here were: 4 Å, 8 Å, 12 Å, 16 Å, and 24 Å. The reference system had a radial size 128 Å. The minimised displacements of the subsystems were compared with the minimised displacements of the reference system.

Energy Error

The energy error as a result of minimisation, ΔE, is the difference in energy of the system before and after minimisation, which is given by

$$\Delta E_{i,R} = E(x + u_{i,R}) - E(x + \hat{u}_{i,R}). \tag{5.19}$$

The energy error with respect to system size, η, is the difference in energy error as a result of minimisation compared to a reference system. η will henceforth be referred to as *energy error* and is given by

$$\eta = \Delta E_{i,R} - \Delta E_{i,\mathrm{ref}}. \tag{5.20}$$

Similarly to the strain error, the domain of the smaller system must be extended to the size of the larger system to compute the energy error between systems of different radial sizes.

5.4 Results and Discussion

5.4.1 Minimisation Strain Error

The strain error as a result of minimisation is the discrepancy between the continuum description and the atomistic description.

The strain error was calculated for three different potentials; a L-IBS potential, an IBS potential and a LJ potential. The results are shown in

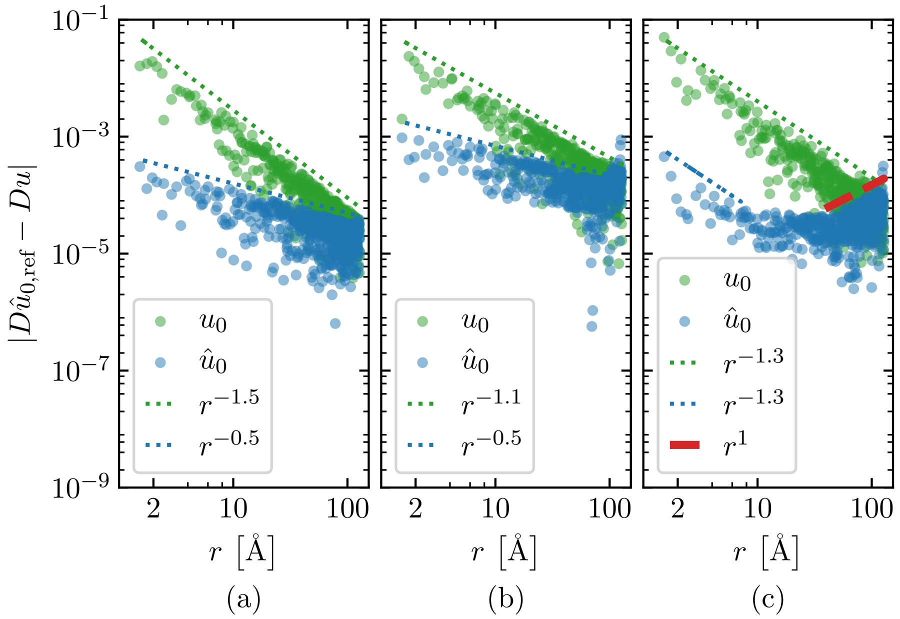

Figure 5.3: Decay of the strain errors, $|D\hat{u}_{0,\mathrm{ref}} - Du|$, where Du is either $Du_{0,R}$ or $D\hat{u}_{0,R}$, with respect to the distance from the crack tip, r. Strain errors are shown for three potentials: a) a L-IBS potential, b) an IBS potential, and c) a LJ potential. The strain errors were calculated by comparing the CLE displacements, $u_{0,R}$, and energy minimised displacements, $\hat{u}_{0,R}$, of a configuration with a radius of 128 Å, to the energy minimised displacements, $\hat{u}_{0,\mathrm{ref}}$, of a reference system with a radius of 512 Å. Rate of decay lines are shown.

Fig. 5.3. The non-minimised and minimised displacements are compared with the minimised displacements of a larger system.

The strain errors associated with the L-IBS and IBS potentials decay with respect to system size, as expected. For the simple potentials, L-IBS and IBS, a minimisation reduced the strain error compared to a larger reference system. The strain error associated with the anharmonic LJ potential decays with the u_0 displacements. However, for the minimised case it does not decay as cleanly as the other two potentials, and exhibits edge effects where the strain error increases as it approaches the fixed boundary of the system. The rate at which the error decays is the same for some range radially close to the crack tip. Beyond that region the error is constant for a short distance and then increases towards the boundary. The radial distance at which the rate increases is much greater than the cutoff distance of the potential.

This shows that even though the potentials had a cutoff distance, their affect upon neighbouring atoms was seen for distances greater than their range, i.e. the range of elastic interaction is much greater than the cutoff of the potential. It also highlights the affects of the fixed boundary and thus its importance to the overall behaviour.

5.4.2 Corrected Displacements

The difference between the CLE displacements and the corrected displacements were small, with a maximum change of $< 0.5\,\%$ of the equilibrium bond length. The difference in positions around the crack tip, where the differences were the greatest are visually shown in Fig. 5.4. The small change in the displacements reinforce the idea that the correction scheme can be considered as the first iteration towards a possible energy minimum.

5.4.3 Forces

The forces across each atom were investigated to highlight the improvement between the CLE displacements and the corrected displacements.

The forces of a system with a radial size of 128 Å were investigated. The system was modelled using a LJ potential with a cutoff of 1.4 Å. The forces of the system with CLE displacements, F_{u_0}, and the forces with the corrected displacements, F_{u_1}, were computed. The forces are shown in Fig. 5.5.

The forces on the atoms across the system behave as expected, such that they decay with increasing radii. The rate of decay of the force for the atoms in the bulk-like part improves with the u_1 displacements, compared to the u_0 displacements. The atoms along the crack surface see no improvement in the rate. However, the overall magnitude has decreased by a small amount.

In the previous chapter during the investigation of the static and flexible boundary methods for minimal energy paths, a hypothesis was that a non-zero net force was hindering convergence of the barrier with respect to system size. Therefore, the force components of an initial fracture system were investigated.

The force components, F_x and F_y, within radial regions centred around the crack tip were computed. The forces were of a system with a radial size of 128 Å, which was modelled using a LJ potential with a cutoff of 1.4 Å. The sum of force components within a ball of radius r, B_r, centred at the crack tip, $\sum_{B_r} F$, were computed with respect to the size of the ball.

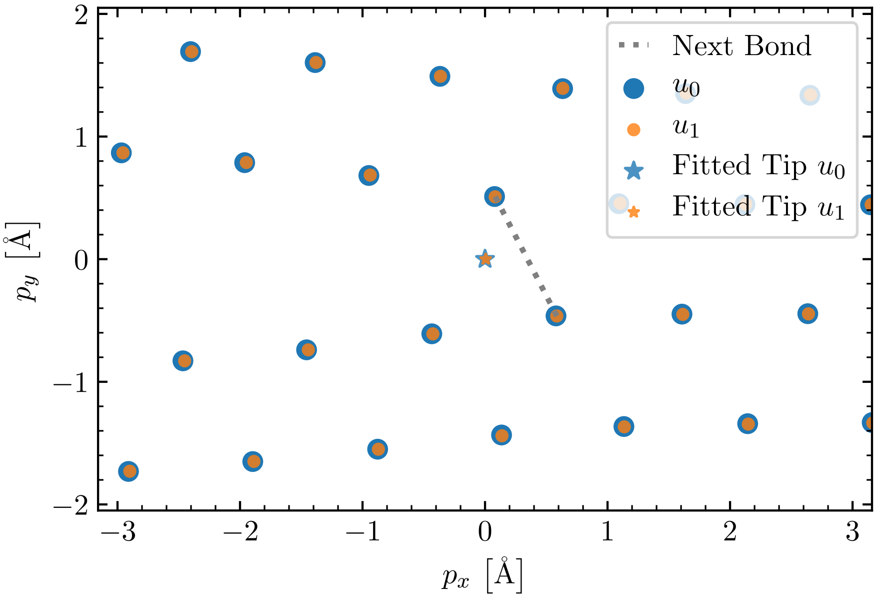

Figure 5.4: Visual representation of a fractured 2D hexagonal lattice, with the CLE displacement, u_0, and the corrected CLE displacements, u_1. The system had a radial size of 8 Å and was modelled using a LJ potential with a cutoff of 1.4 Å. The correction term used to correct the displacements was computed on a system with a radial size of 64 Å. The fitted crack tip for both displacements are shown, along with the next bond along the crack propagation direction. p_x and p_y are the components of the atomic positions in x and y respectively, which are plotted relative to the crack tip. The atoms with u_0 displacements are plotted larger than the atoms with u_1 displacements; thus, the centre points of the atoms should be compared.

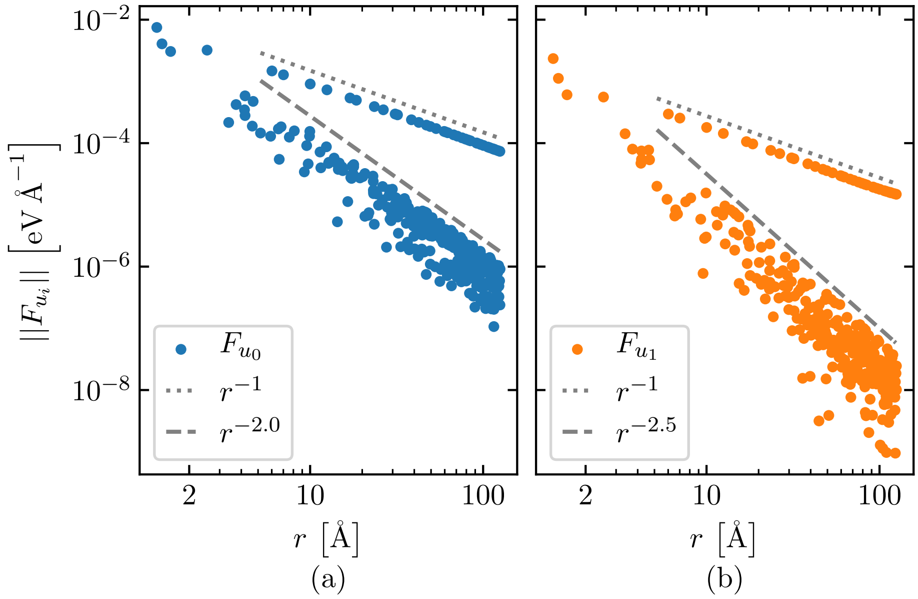

(a) (b)

Figure 5.5: Decay of forces, F, of a 2D hexagonal lattice with a) CLE displacements, u_0, and b) corrected displacements, u_1. The system was modelled using a LJ potential with a cutoff radius of 1.4 Å. The small dashed lines and the large dashed lines are the rates of decay for atoms along the crack surface and atoms in the bulk part of the system, respectively.

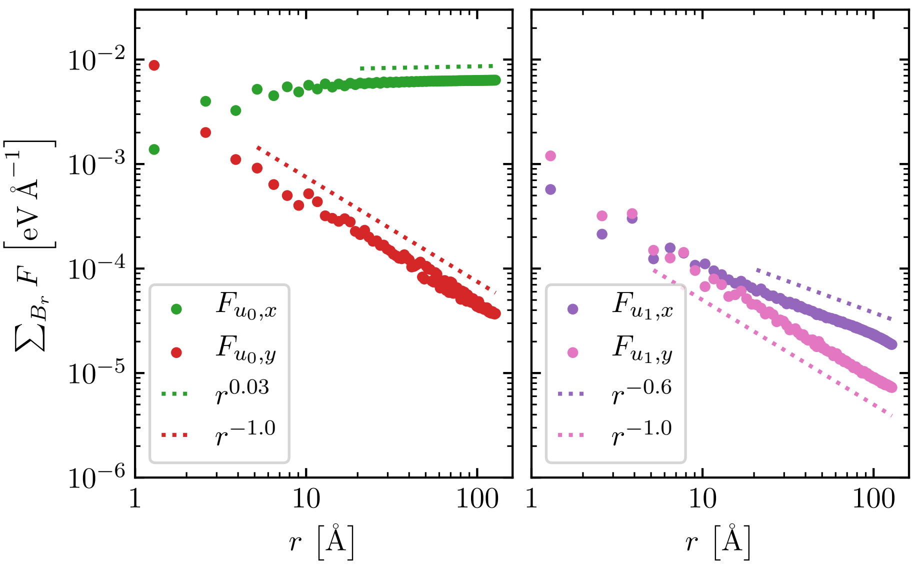

(a) (b)

Figure 5.6: Sum of the force components, $\sum_{B_r} F$, within a ball of radius r, B_r, centred at the crack tip, for a) the CLE displacements, u_0, and b) the corrected displacements, u_1. The forces are of a 2D hexagonal lattice, with a radius of 128 Å, modelled using a LJ potential with a cutoff of 1.4 Å. $F_{u_i,x}$ and $F_{u_i,y}$ are the force components in x and y respectively. Rate of decay lines are shown.

The sum of forces components, $F_{u_0,x}$ and $F_{u_0,y}$, for the CLE displacements are shown in Fig. 5.6. The force component in y, red data points, decays with radial size. The force component in x, green data points, does not decay with radial size; it remains fairly constant and diverges at a slow rate. There is a net force in the x direction which comes from the asymmetry in that direction, as opposed to the y direction which maintains symmetry.

The corrected displacements, which were computed on a system four times as large, were applied and the sum of forces components were computed. The force components, $F_{u_1,x}$ and $F_{u_1,y}$, are shown in Fig. 5.6. $F_{u_1,y}$ decays with a similar rate to $F_{u_0,y}$ of r^{-1} and is of a lower magnitude. $F_{u_1,x}$ decays compared to $F_{u_0,x}$; although it decays with a slower rate compared to the rate for $F_{u_1,y}$. The corrected displacements remove the constant force component in the x direction.

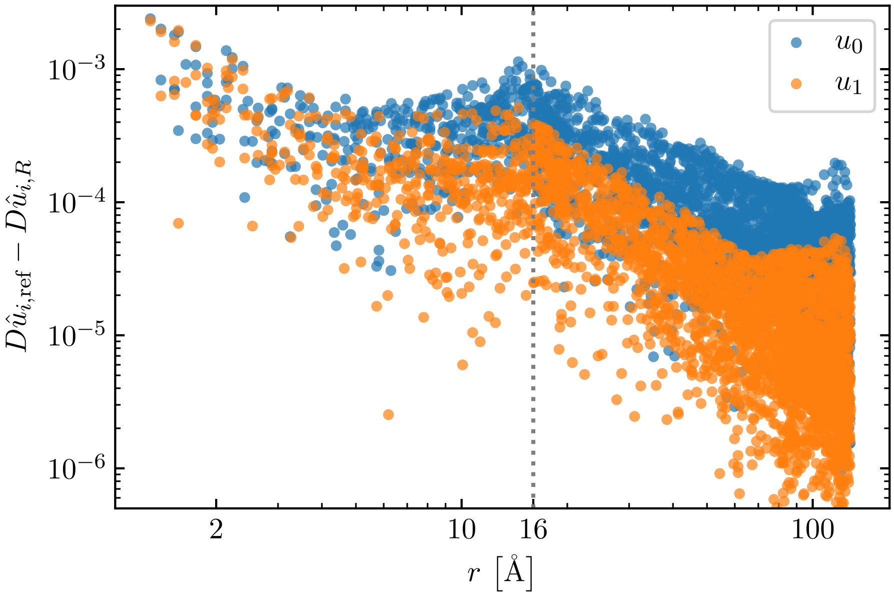

Figure 5.7: Strain error of a system with respect to a reference system, $D\hat{u}_{i,\mathrm{ref}} - D\hat{u}_{i,R}$, plotted as a function of distance from the crack tip, r. The system was a 2D hexagonal lattice modelled using a LJ potential with a cutoff of 1.4 Å. A system with a radial size of 128 Å with an energy minimised region of 16 Å was compared to a reference system with a radial size of 128 Å with a energy minimised region of 128 Å. The displacements for the system and reference system are $\hat{u}_{i,R}$ and $\hat{u}_{i,\mathrm{ref}}$ respectively. For the system with the smaller minimised region, the dashed line at $r = 16$ Å denotes the point at which the atomistic region transitions to the continuum region. A subset of points are shown. The index i is 0 or 1 for the CLE displacements or the corrected displacements respectively.

5.4.4 Strain and Energy Errors

To demonstrate the validity of the scheme, the strain errors and the energy errors with respect to system size were calculated. Two simple potentials were investigated to show proof of the concept.

Strain Error

The boundary effect of a smaller subsystem representing a larger one can be seen more clearly in Fig. 5.7, where the strain error with respect to a larger system is plotted. A system with a radial size of 128 Å with an energy minimised region of 16 Å was compared with an energy minimised region of 128 Å. The strain errors for the CLE displacements and corrected displacements were computed.

There is overall decay of the error, with improved overall decay from the corrected displacements. The strain error of atoms near the centre of the crack remain relatively similar to each other. There is a change at the boundary of the inner region, near 16 Å, for the u_0 displacements. The optimised u_1 displacements, $\hat{u}_1$, improve this mismatch over the optimised CLE displacements, $\hat{u}_0$. The corrected displacements somewhat corrects the finite edge effect of the smaller minimised system. The finite size effect of the larger reference system, near 80 Å and beyond, can be seen towards the edge of the system because the strain error increases as it approaches the boundary.

Error Convergence

The correction scheme modifies the boundary conditions in an attempt to improve the error decay. The strain error convergence and the energy error convergence tests with respect to system size are detailed.

The errors computed here are the differences between two systems. A system with a minimised region of size R was compared to a minimised reference system with a radius of 128 Å.

Comparing the subsystems with the reference system, the strain error convergence and the energy error convergence are shown in Fig. 5.8 and Fig. 5.9, for an IBS potential and a LJ potential respectively.

For the IBS potential, the corrected displacements only improve the prefactor by a small amount and the rate of convergence remains roughly the same. There is little benefit seen in the application of the correction term for this simple potential, at least in regards to the strain error. However, in terms of the energy error, the correction scheme turned the divergent error into a convergent error.

For the LJ potential, applying the corrected displacements showed an improvement over the CLE displacements. The rate of the strain error decay almost doubles. The improvement of the energy error is similar to the IBS potential where errors turned from divergent to convergent.

A divergent energy error brings into question whether the minimised u_0 displacements can be considered as a valid reference system. This could be an issue of the system sizes used here, and if so even larger systems are required

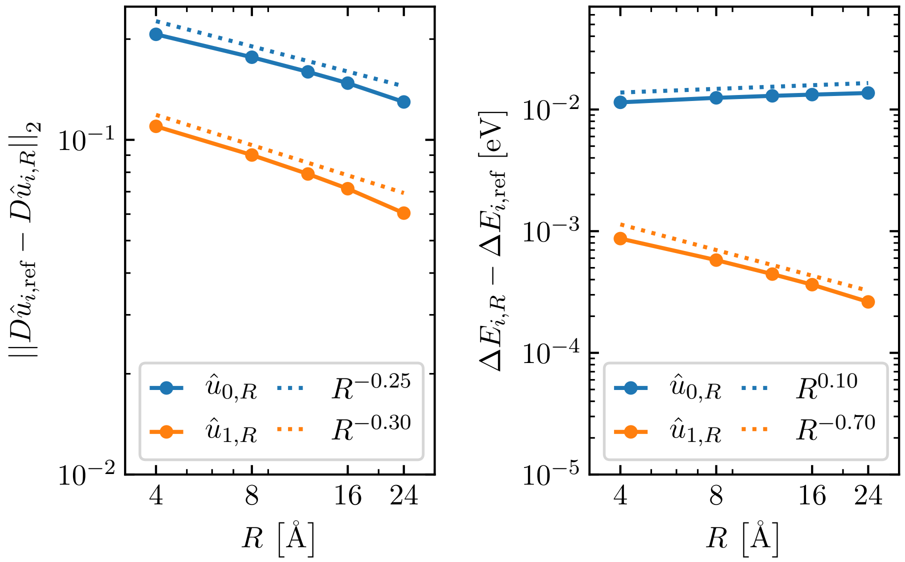

(a) (b)

Figure 5.8: Convergence of a) the strain error, $||D\hat{u}_{i,\mathrm{ref}} - D\hat{u}_{i,R}||_2$, and b) the energy error, $\Delta E_{i,R} - \Delta E_{i,\mathrm{ref}}$, with respect to system size, R, using an IBS potential with a cutoff of 1.4 Å. Each system was compared to a reference configuration with a radial size of 128 Å. The index i is 0 or 1 for the CLE displacements or the corrected displacements respectively. Rate of decay lines are shown.

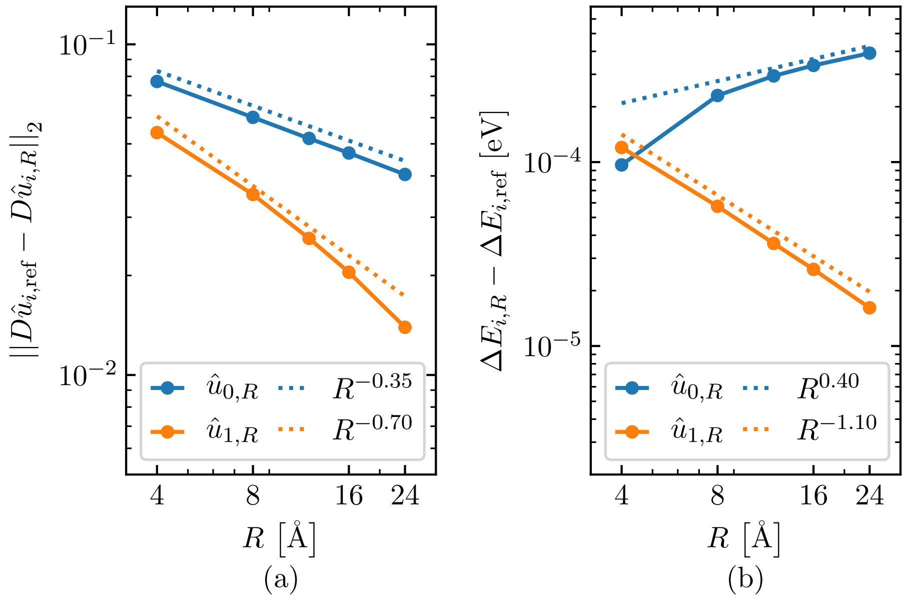

Figure 5.9: Convergence of a) the strain error, $||D\hat{u}_{i,\mathrm{ref}} - D\hat{u}_{i,R}||_2$, and b) the energy error, $\Delta E_{i,R} - \Delta E_{i,\mathrm{ref}}$, with respect to system size, R, using a LJ potential with a cutoff of 1.4 Å. Each system was compared to a reference configuration with a radial size of 128 Å. The index i is 0 or 1 for the CLE displacements or the corrected displacements respectively. Rate of decay lines are shown.

to address this. The energy error may diverge initially and then flatten out at larger system sizes. Or, the issue is based in the potentials investigated here and more realistic potentials may show a convergent energy error within the system sizes explored here. Investigation into local properties would be beneficial to further test this method. Local properties, such as the energy barrier, which do not depend so heavily on the boundary of the system would allow for comparison of that property across both reference systems.

5.5 Conclusion

A method to improve the boundary conditions used for fracture simulations was tested. To explore the ability of the method, convergence tests of the strain error and the energy error were performed on a 2D hexagonal lattice with short range potentials.

To tackle large system sizes required by fracture simulations, a method to improve the boundary conditions was developed and tested. The scheme performs an iteration, similar to Newton's method, towards the energy minimum on a system with CLE displacements. The benefit of this method is that the components of the iteration step are computed using computationally cheaper variants compared to Newton's method. This is not particularly important for interatomic potentials, since they are relatively cheap. This method allows the use of more accurate atomic descriptions, such as DFT, to be easily used in place of the interatomic potentials. The convergence tests showed improvements when using the corrected displacements, particularly for a LJ potential. The convergence rate for the strain error doubles. The energy errors goes from a diverging property to a converging property. This method improves the representation of the reference system compared to the uncorrected CLE displacements. Compared to the CLE displacements, the corrected displacements can allow for either: the use of smaller system sizes for the same magnitude of error; or for smaller errors on system with comparable size.

It is expected that this method will produce varying levels of improvements for different potentials and materials. Error convergence rates, with respect to system size, are expected to be slower for longer range potentials, when compared to shorter range potentials. Longer range potentials will likely need larger boundary systems to produce the correction term. The cost of computing the correction term on a larger boundary system could be reduced by computing the Hessian term on a crystal configuration. However, the error convergence rates, with respect to system size, would be worse, and therefore the method would be less effective.

6 Conclusion

Nonlinear methods were employed to compute properties of atomistic brittle fracture. New methodology was developed and tested with a 2D hexagonal lattice as a proof of concept.

Fracture propagation of the SiC 6H polytype along the (0001) plane was studied computationally and experimentally; both the experimental and MD simulations showed brittle cleavage. The slow, stable crack growth of the experiment allowed comparison of the experimentally measured fracture energy with the static surface energy DFT calculations. The results were in relatively good agreement with one another compared to previous literature. The method employed in the experiments presents a new opportunity to study fracture at the micro-structural length scale.

Methods to compute energy profiles and energy barriers for breaking a single bond along the crack advancement direction were developed. The energy barrier and lattice trapping range for a fractured diamond-structured carbon system, which was open along the (111) plane, and a fractured 2D hexagonal lattice were computed. The static and flexible boundary methods are relatively simple compared to the pseudo arc-length continuation scheme. However, a discrepancy between the method and theory for the flexible case was found, which called its credibility into question. The continuation scheme was tested on a simple 2D hexagonal lattice and proved to be useful at obtaining the energy barrier and the detailed bounds of the lattice trapping range. The continuation scheme also showed how the system would evolve. The methodology in its current state is computationally expensive. An adaptive step size, which is larger in the straight segments and smaller as it approaches a fold, would reduce a significant chunk of the cost.

Basic MD simulations generally run in the picoseconds range. Thus, the simulations are limited to events that happen in that time frame. The energy barrier of an event can be large in the sense that they are not so easily overcome via thermal activation due to the low probability that the atom(s) have enough energy to overcome the barrier. Consequently, this leads to long timescales for such events to occur. These energy barriers could be used to obtain transition rates for use in large scale KMC simulations to statistically simulate the chance of crossing the barrier to reduce computational time.

A method to tackle the large system sizes needed, and to combat the imperfect conversion from the CLE solutions to an atomistic domain, was developed. The method computed a new boundary from a larger atomistic domain. It was shown to improve convergence rates of the strain error and the total energy error with respect to the uncorrected case. While the computation of the new boundary is expensive, the key progression and philosophy is that the correction term could be computed using higher accuracy codes such as DFT. The correction term partly relies on the crystal structure, and inherent periodicity in DFT computation allows for relatively small domains to represent much larger domains.

The computational expense of the continuation scheme could also be reduced by incorporating the boundary correction scheme. All the methods developed here can be extended in a variety of directions. The methods were only tested on a simple 2D lattice with relatively simple potentials. Extending the cutoff range to include second nearest neighbours, or beyond, will stretch the possible application of these methods. Some other extensions include modelling surfaces of realistic materials, or adding variations in the structure such as dislocations, grain boundaries, and impurities. These would add challenging environments and intricate local chemical interactions which would require the use of higher accuracy modelling techniques such as DFT. These simple modifications can lead to results with potentially complex outcomes, and exploring these modifications would be another step towards the pursuit of understanding the vast energy landscape and dynamics of brittle fracture.

Bibliography

[1] Sernicola, G., Giovannini, T., Patel, P., Kermode, J. R., Balint, D. S., Britton, T. B. & Giuliani, F. In situ stable crack growth at the micron scale. *Nature Communications* **8,** 108. doi:`10.1038/s41467-017-00139-w` (Dec. 2017).

[2] Patel, P., Buze, M., Pastewka, L., Braun, J., Ortner, C. & Kermode, J. R. *Atomistic Modelling of Fracture with Nonlinear Elastic Boundary Conditions (In prep.)*

[3] Padture, N. P. Advanced structural ceramics in aerospace propulsion. *Nature Materials* **15,** 804–809. doi:`10.1038/nmat4687` (Aug. 2016).

[4] Kazantseva, N. V., Stepanova, N. N., Rigmant, M. B., Stepanova, N. N. & Rigmant, M. B. *Superalloys* doi:`10.1201/9781315106168` (CRC Press, Dec. 2018).

[5] Ohnabe, H., Masaki, S., Onozuka, M., Miyahara, K. & Sasa, T. Potential application of ceramic matrix composites to aero-engine components. *Composites Part A: Applied Science and Manufacturing* **30,** 489–496. doi:`10.1016/S1359-835X(98)00139-0` (Apr. 1999).

[6] Griffith, A. A. The Phenomena of Rupture and Flow in Solids. *Philosophical Transactions of the Royal Society A: Mathematical, Physical and Engineering Sciences* **221,** 163–198. doi:`10.1098/rsta.1921.0006` (Jan. 1921).

[7] Bao, Z., Guo, X. & Shang, F. An atomistic investigation into the nature of fracture of Ni/Al2O3 interface with yttrium dopant under tension. *Engineering Fracture Mechanics* **150,** 239–247. doi:`10.1016/j.engfracmech.2015.05.040` (2015).

[8] Bitzek, E., Kermode, J. R. & Gumbsch, P. Atomistic aspects of fracture. *International Journal of Fracture* **191,** 13–30. doi:10.1007/s10704-015-9988-2 (2015).

[9] Tamer Al-Motasem, A., Mai, N. T., Choi, S. T. & Posselt, M. Atomistic study on mixed-mode fracture mechanisms of ferrite iron interacting with coherent copper and nickel nanoclusters. *Journal of Nuclear Materials.* doi:10.1016/j.jnucmat.2015.12.046 (2016).

[10] Bernstein, N., Kermode, J. R. & Csányi, G. Hybrid atomistic simulation methods for materials systems. *Reports on Progress in Physics.* doi:10.1088/0034-4885/72/2/026501 (2009).

[11] E, W. *Principles of Multiscale Modeling* 488 (Cambridge University Press, 2011).

[12] Carter, C. B. & Norton, M. G. *Ceramic Materials* doi:10.1007/978-1-4614-3523-5 (Springer New York, New York, NY, 2013).

[13] Brenner, D. W. & Shenderova, O. A. Theory and modelling of diamond fracture from an atomic perspective. *Philosophical Transactions of the Royal Society A: Mathematical, Physical and Engineering Sciences* **373,** 20140139. doi:10.1098/rsta.2014.0139 (Mar. 2015).

[14] Lawn, B. *Fracture of Brittle Solids* Second, 11–12. doi:10.1017/CBO9780511623127 (Cambridge University Press, 1993).

[15] Braibant, S., Giacomelli, G. & Spurio, M. *Particles and Fundamental Interactions* doi:10.1007/978-94-007-2464-8 (Springer Netherlands, Dordrecht, 2012).

[16] Gupta, V. P. *Principles and Applications of Quantum Chemistry* doi:10.1016/C2014-0-05143-X (Elsevier, 2016).

[17] Born, M. & Oppenheimer, R. Zur Quantentheorie der Molekeln. *Annalen der Physik* **389,** 457–484. doi:10.1002/andp.19273892002 (1927).

[18] Martin, R. M. *Electronic Structure* 624. doi:10.1017/CBO9780511805769 (Cambridge University Press, Cambridge, 2004).

[19] Rajagopal, a. K. & Callaway, J. Inhomogeneous electron gas. *Physical Review B* **7,** 1912–1919. doi:10.1103/PhysRevB.7.1912 (1973).

[20] Kryachko, E. S. & Ludeña, E. V. *Density functional theory: Foundations reviewed* 2014. doi:10.1016/j.physrep.2014.06.002.

[21] Foulkes, W. M. C., Mitas, L., Needs, R. J. & Rajagopal, G. Quantum Monte Carlo simulations of solids. *Reviews of Modern Physics* **73,** 33–83. doi:10.1103/RevModPhys.73.33 (2001).

[22] Austin, B. M., Zubarev, D. Y. & Lester, W. A. Quantum Monte Carlo and Related Approaches. *Chemical Reviews* **112,** 263–288. doi:10.1021/cr2001564 (Jan. 2012).

[23] Hohenberg, P. & Kohn, W. Inhomogeneous Electron Gas. *Physical Review* **136,** B864–B871. doi:10.1103/PhysRev.136.B864 (Nov. 1964).

[24] Kohn, W. & Sham, L. J. Self-Consistent Equations Including Exchange and Correlation Effects. *Physical Review* **140,** A1133–A1138. doi:10.1103/PhysRev.140.A1133 (Nov. 1965).

[25] Tran, F., Stelzl, J. & Blaha, P. Rungs 1 to 4 of DFT Jacob's ladder: Extensive test on the lattice constant, bulk modulus, and cohesive energy of solids. *The Journal of Chemical Physics* **144,** 204120. doi:10.1063/1.4948636 (May 2016).

[26] Becke, A. D. Perspective: Fifty years of density-functional theory in chemical physics. *The Journal of Chemical Physics* **140,** 18A301. doi:10.1063/1.4869598 (May 2014).

[27] Cohen, A. J., Mori-Sánchez, P. & Yang, W. Challenges for Density Functional Theory. *Chemical Reviews* **112,** 289–320. doi:10.1021/cr200107z (Jan. 2012).

[28] Singh, D. J. & Nordström, L. *Planewaves, Pseudopotentials and the LAPW Method* doi:10.1007/978-0-387-29684-5 (Springer US, 2006).

[29] Payne, M. C., Teter, M. P., Allan, D. C., Arias, T. A. & Joannopoulos, J. D. Iterative minimization techniques for ab initio total-energy calculations: molecular dynamics and conjugate gradients. *Reviews of Modern Physics* **64,** 1045–1097. doi:10.1103/RevModPhys.64.1045 (Oct. 1992).

[30] Sirdeshmukh, D. B., Sirdeshmukh, L. & Subhadra, K. *Atomistic Properties of Solids* doi:10.1007/978-3-642-19971-4 (Springer Berlin Heidelberg, Berlin, Heidelberg, 2011).

[31] Milman, V., Lee, M. H. & Payne, M. C. Ground-state properties of CoSi2 determined by a total-energy pseudopotential method. *Physical Review B* **49,** 16300–16308. doi:10.1103/PhysRevB.49.16300 (June 1994).

[32] Monkhorst, H. J. & Pack, J. D. Special points for Brillouin-zone integrations. *Physical Review B* **13,** 5188–5192. doi:10.1103/PhysRevB.13.5188 (June 1976).

[33] Hamann, D. R., Schlüter, M. & Chiang, C. Norm-Conserving Pseudopotentials. *Physical Review Letters* **43,** 1494–1497. doi:10.1103/PhysRevLett.43.1494 (Nov. 1979).

[34] Vanderbilt, D. Soft self-consistent pseudopotentials in a generalized eigenvalue formalism. *Physical Review B* **41,** 7892–7895. doi:10.1103/PhysRevB.41.7892 (Apr. 1990).

[35] Milman, V., Winkler, B., White, J. A., Pickard, C. J., Payne, M. C., Akhmatskaya, E. V. & Nobes, R. H. Electronic structure, properties, and phase stability of inorganic crystals: A pseudopotential plane-wave study. *International Journal of Quantum Chemistry* **77,** 895–910. doi:10.1002/(SICI)1097-461X(2000)77:5<895::AID-QUA10>3.0.CO;2-C (Jan. 2000).

[36] Clark, S. J., Segall, M. D., Pickard, C. J., Hasnip, P. J., Probert, M. I. J., Refson, K. & Payne, M. C. First principles methods using CASTEP. *Zeitschrift für Kristallographie - Crystalline Materials* **220.** doi:10.1524/zkri.220.5.567.65075 (Jan. 2005).

[37] Newton, I. *Philosophiæ Naturalis Principia Mathematica (Latin)* (1687).

[38] Lagrange, J.-L. *Mécanique analytique* doi:10.1017/CBO9780511701795 (Cambridge University Press, Cambridge, 1815).

[39] Benacquista, M. J. & Romano, J. D. *Classical Mechanics* doi:10.1007/978-3-319-68780-3 (Springer International Publishing, Cham, 2018).

[40] Swope, W. C., Andersen, H. C., Berens, P. H. & Wilson, K. R. A computer simulation method for the calculation of equilibrium constants for the formation of physical clusters of molecules: Application to small water clusters. *The Journal of Chemical Physics* **76,** 637–649. doi:10.1063/1.442716 (Jan. 1982).

[41] Frenkel, D. & Smit, B. *Understanding Molecular Simulation* 638. doi:10.1016/B978-0-12-267351-1.X5000-7 (Elsevier, 2002).

[42] Stillinger, F. H. & Weber, T. a. Computer simulation of local order in condensed phases of silicon. *Physical Review B* **31,** 5262–5271. doi:10.1103/PhysRevB.31.5262 (1985).

[43] Raabe, D. *Computational Materials Science* doi:10.1002/3527601945 (Wiley, June 1998).

[44] Lewars, E. G. *Computational Chemistry* doi:10.1007/978-3-319-30916-3 (Springer International Publishing, Cham, 2016).

[45] Tersoff, J. New empirical approach for the structure and energy of covalent systems. *Physical Review B* **37,** 6991–7000. doi:10.1103/PhysRevB.37.6991 (Apr. 1988).

[46] Pastewka, L., Pou, P., Pérez, R., Gumbsch, P. & Moseler, M. Describing bond-breaking processes by reactive potentials: Importance of an environment-dependent interaction range. *Physical Review B* **78,** 161402. doi:10.1103/PhysRevB.78.161402 (Oct. 2008).

[47] Pastewka, L., Klemenz, A., Gumbsch, P. & Moseler, M. Screened empirical bond-order potentials for Si-C. *Physical Review B* **87,** 205410. doi:10.1103/PhysRevB.87.205410 (May 2013).

[48] Andersen, H. C. Molecular dynamics simulations at constant pressure and/or temperature. *The Journal of Chemical Physics* **72,** 2384–2393. doi:10.1063/1.439486 (Feb. 1980).

[49] Schlick, T. *Molecular Modeling and Simulation: An Interdisciplinary Guide* doi:10.1007/978-1-4419-6351-2 (Springer New York, New York, NY, 2010).

[50] Hansen, K. *Statistical Physics of Nanoparticles in the Gas Phase* doi:10.1007/978-3-319-90062-9 (Springer International Publishing, Cham, 2018).

[51] Leimkuhler, B. & Matthews, C. *Molecular Dynamics* doi:10.1007/978-3-319-16375-8 (Springer International Publishing, Cham, 2015).

[52] Fineberg, J., Gross, S., Marder, M. & Swinney, H. Instability in dynamic fracture. *Physical Review Letters* **67,** 457–460. doi:10.1103/PhysRevLett.67.457 (1991).

[53] Bazant, M. Z., Kaxiras, E. & Justo, J. F. Environment Dependent Interatomic Potential for Bulk Silicon. *Physical Review B* **56,** 15. doi:10.1103/PhysRevB.56.8542 (1997).

[54] Bartók, A. P., Kermode, J., Bernstein, N. & Csányi, G. Machine Learning a General-Purpose Interatomic Potential for Silicon. *Physical Review X* **8,** 041048. doi:10.1103/PhysRevX.8.041048 (Dec. 2018).

[55] Kermode, J. R., Albaret, T., Sherman, D. M., Bernstein, N., Gumbsch, P., Payne, M. C., Csányi, G. & De Vita, A. Low-speed fracture instabilities in a brittle crystal. *Nature* **455,** 1224–1227. doi:10.1038/nature07297 (2008).

[56] Rafii-Tabar, H., Hua, L. & Cross, M. A multi-scale atomistic-continuum modelling of crack propagation in a two-dimensional macroscopic plate. *Journal of Physics: Condensed Matter* **10,** 2375–2387. doi:10.1088/0953-8984/10/11/003 (1998).

[57] Luo, X. & Qin, Y. *Hybrid machining : theory, methods, and case studies* (2018).

[58] Zhang, B., Yang, Z., Wu, Y. & Sun, H. Hierarchical multiscale modeling of failure in unidirectional fiber-reinforced plastic matrix composite. *Materials & Design (1980-2015)* **31,** 2312–2318. doi:10.1016/J.MATDES.2009.12.009 (May 2010).

[59] Ural, A. & Mischinski, S. Multiscale modeling of bone fracture using cohesive finite elements. *Engineering Fracture Mechanics* **103,** 141–152. doi:10.1016/J.ENGFRACMECH.2012.05.008 (May 2013).

[60] Guo, Y., Liang, Y., Li, J. & Gong, B. A novel connectivity-based hierarchical model for multi-scale fracture system in carbonate reservoir simulation. *Fuel* **250,** 327–338. doi:10.1016/J.FUEL.2019.03.048 (Aug. 2019).

[61] Oden, J. T., Vemaganti, K. & Moës, N. Hierarchical modeling of heterogeneous solids. *Computer Methods in Applied Mechanics and Engineering* **172,** 3–25. doi:10.1016/S0045-7825(98)00224-2 (Apr. 1999).

[62] Kermode, J. R., Gleizer, A., Kovel, G., Pastewka, L., Csányi, G., Sherman, D. & De Vita, A. Low Speed Crack Propagation via Kink Formation and Advance on the Silicon (110) Cleavage Plane. *Physical Review Letters* **115,** 1–5. doi:10.1103/PhysRevLett.115.135501 (2015).

[63] Gleizer, A., Peralta, G., Kermode, J. R., De Vita, A. & Sherman, D. Dissociative chemisorption of O2 inducing stress corrosion cracking in silicon crystals. *Physical Review Letters* **112,** 1–5. doi:10.1103/PhysRevLett.112.115501 (2014).

[64] Kermode, J. R., Ben-Bashat, L., Atrash, F., Cilliers, J. J., Sherman, D. & De Vita, A. Macroscopic scattering of cracks initiated at single impurity atoms. *Nature Communications* **4,** 2441. doi:10.1038/ncomms3441 (2013).

[65] Moras, G., Ciacchi, L. C., Elsässer, C., Gumbsch, P. & De Vita, A. Atomically smooth stress-corrosion cleavage of a hydrogen-implanted crystal. *Physical Review Letters* **105,** 1–4. doi:10.1103/PhysRevLett.105.075502 (2010).

[66] Ladevèze, P. Multiscale modelling and computational strategies for composites. *International Journal for Numerical Methods in Engineering* **60,** 233–253. doi:10.1002/nme.960 (2004).

[67] Smith, R. C. *Uncertainty Quantification Theory, Implementation, and Applications* (SIAM, 2014).

[68] Probert, M. Improved algorithm for geometry optimisation using damped molecular dynamics. *Journal of Computational Physics* **191,** 130–146. doi:10.1016/S0021-9991(03)00308-5 (Oct. 2003).

[69] Cottle, R. W. & Thapa, M. N. *Linear and Nonlinear Optimization* doi:10.1007/978-1-4939-7055-1 (Springer New York, New York, NY, 2017).

[70] Nocedal, J. & Wright, S. *Numerical Optimization* doi:10.1007/978-0-387-40065-5 (Springer New York, 2006).

[71] Bitzek, E., Koskinen, P., Gähler, F., Moseler, M. & Gumbsch, P. Structural Relaxation Made Simple. *Physical Review Letters* **97,** 170201. doi:10.1103/PhysRevLett.97.170201 (Oct. 2006).

[72] Zörnig, P. *Nonlinear Programming* doi:10.1515/9783110315288 (DE GRUYTER, Berlin, Boston, Jan. 2014).

[73] K Mogensen, P. & N Riseth, A. Optim: A mathematical optimization package for Julia. *Journal of Open Source Software.* doi:10.21105/joss.00615 (2018).

[74] Hess, S. *Tensors for Physics* doi:10.1007/978-3-319-12787-3 (Springer International Publishing, Cham, 2015).

[75] Perez, N. *Fracture Mechanics* doi:10.1007/978-3-319-24999-5 (Springer International Publishing, Cham, 2017).

[76] Gould, P. L. *Introduction to linear elasticity* 1–346. doi:10.1007/978-1-4614-4833-4 (Springer New York, New York, NY, 2013).

[77] Iadonisi, G., Cantele, G. & Chiofalo, M. L. *Introduction to Solid State Physics and Crystalline Nanostructures* doi:10.1007/978-88-470-2805-0 (Springer Milan, Milano, 2014).

[78] Scott, T. R. *The Universe as It Really Is* doi:10.7312/scot18494 (Columbia University Press, New York Chichester, West Sussex, Dec. 2018).

[79] *Novel Aspects of Diamond* (ed Yang, N.) doi:10.1007/978-3-030-12469-4 (Springer International Publishing, Cham, 2019).

[80] Perdew, J. P., Burke, K. & Ernzerhof, M. Generalized Gradient Approximation Made Simple. *Physical Review Letters* **77,** 3865–3868. doi:10.1103/PhysRevLett.77.3865 (Oct. 1996).

[81] *Smart Ceramics* (ed Mishra, A. K.) doi:10.1201/9781315163598 (Pan Stanford, Mar. 2018).

[82] Marder, M. Effects of atoms on brittle fracture. *International Journal of Fracture.* doi:10.1023/B:FRAC.0000049501.35598.87 (2004).

[83] Jones, J. E. On the Determination of Molecular Fields. II. From the Equation of State of a Gas. *Proceedings of the Royal Society A: Mathematical, Physical and Engineering Sciences* **106,** 463–477. doi:10.1098/rspa.1924.0082 (Oct. 1924).

[84] Teoh, S. H. Fatigue of biomaterials: A review. *International Journal of Fatigue.* doi:10.1016/S0142-1123(00)00052-9 (2000).

[85] Padture, N. P., Gell, M. & Jordan, E. H. Thermal barrier coatings for gas-turbine engine applications. *Science (New York, N.Y.)* **296,** 280–4. doi:10.1126/science.1068609 (Apr. 2002).

[86] Cowles, B. A. High cycle fatigue in aircraft gas turbines—an industry perspective. *International Journal of Fracture* **80,** 147–163. doi:10.1007/BF00012667 (Apr. 1996).

[87] Lall, P., Islam, M., Evans, J., Suhling, J. & Shete, T. Damage mechanics of electronics on metal-backed substrates in harsh environments. *IEEE Transactions on Components and Packaging Technologies* **29,** 204–212. doi:10.1109/TCAPT.2006.870390 (Mar. 2006).

[88] *ASTM E399-12e3, Standard Test Method for Linear-Elastic Plane-Strain Fracture Toughness KIc of Metallic Materials. ASTM International, West Conshohocken, PA* 2012. doi:10.1520/E0399-12E03.

[89] *C28.01 Committee. C1161-13 Standard Test Method for Flexural Strength of Advanced Ceramics at Ambient Temperature. ASTM International, West Conshohocken, PA* 2013. doi:10.1520/C1161-13.

[90] Wiederhorn, S. M., Roberts, D. E., Chuang, T.-j. & Chuck, L. Damage-Enhanced Creep in a Siliconized Silicon Carbide: Phenomenology. *Journal of the American Ceramic Society* **71,** 602–608. doi:10.1111/j.1151-2916.1988.tb05926.x (July 1988).

[91] Chen, D., Zhang, X.-F. & Ritchie, R. O. Effects of Grain-Boundary Structure on the Strength, Toughness, and Cyclic-Fatigue Properties of a Monolithic Silicon Carbide. *Journal of the American Ceramic Society* **83,** 2079–2081. doi:10.1111/j.1151-2916.2000.tb01515.x (Dec. 2004).

[92] Al Nasiri, N., Ni, N., Saiz, E., Chevalier, J., Giuliani, F. & Vandeperre, L. Effect of microstructure and grain boundary chemistry on slow crack growth in silicon carbide at ambient conditions. *Journal of the European Ceramic Society* **35,** 2253–2260. doi:10.1016/J.JEURCERAMSOC.2015.02.020 (Aug. 2015).

[93] Krenkel, W. & Berndt, F. C/C–SiC composites for space applications and advanced friction systems. *Materials Science and Engineering: A* **412,** 177–181. doi:10.1016/J.MSEA.2005.08.204 (Dec. 2005).

[94] Ansermet, J.-P. & Brechet, S. D. *Principles of Thermodynamics* doi:10.1017/9781108620932 (Cambridge University Press, Dec. 2018).

[95] Tahir-Kheli, R. *General and Statistical Thermodynamics* doi:10.1007/978-3-642-21481-3 (Springer Berlin Heidelberg, Berlin, Heidelberg, 2012).

[96] Razeghi, M. *Fundamentals of Solid State Engineering* doi:10.1007/978-3-319-75708-7 (Springer International Publishing, Cham, 2019).

[97] Benedek, G. & Toennies, J. P. *Atomic Scale Dynamics at Surfaces* doi:10.1007/978-3-662-56443-1 (Springer Berlin Heidelberg, Berlin, Heidelberg, 2018).

[98] Dove, M. T. *Introduction to Lattice Dynamics* 258. doi:10.1017/CBO9780511619885 (Cambridge University Press, Cambridge, 1993).

[99] Wang, Y., Liu, Z.-K. & Chen, L.-Q. Thermodynamic properties of Al, Ni, NiAl, and Ni3Al from first-principles calculations. *Acta Materialia* **52,** 2665–2671. doi:10.1016/J.ACTAMAT.2004.02.014 (May 2004).

[100] Wang, Y., Shang, S.-L., Fang, H., Liu, Z.-K. & Chen, L.-Q. First-principles calculations of lattice dynamics and thermal properties of polar solids. *npj Computational Materials* **2,** 16006. doi:10.1038/npjcompumats.2016.6 (Nov. 2016).

[101] Baroni, S., de Gironcoli, S., Dal Corso, A. & Giannozzi, P. Phonons and related crystal properties from density-functional perturbation theory. *Reviews of Modern Physics* **73,** 515–562. doi:10.1103/RevModPhys.73.515 (July 2001).

[102] Xie, J., de Gironcoli, S., Baroni, S. & Scheffler, M. First-principles calculation of the thermal properties of silver. *Physical Review B* **59,** 965–969. doi:10.1103/PhysRevB.59.965 (Jan. 1999).

[103] Maradudin, A. A. *Theory of lattice dynamics in the harmonic approximation* 319 (Academic Press, 1963).

[104] Togo, A., Chaput, L., Tanaka, I. & Hug, G. First-principles phonon calculations of thermal expansion in Ti3SiC2, Ti3AlC2, and Ti3GeC2. *Physical Review B* **81,** 174301. doi:10.1103/PhysRevB.81.174301 (May 2010).

[105] Kermode, J. Multiscale Hybrid Simulation of Brittle Fracture. *PhD Thesis, University of Cambridge,* 186. doi:10.17863/CAM.16637 (2008).

[106] Knauss, W. G. Stresses in an Infinite Strip Containing a Semi-Infinite Crack. *Journal of Applied Mechanics* **33,** 356. doi:10.1115/1.3625049 (June 1966).

[107] Capitani, G. C., Di Pierro, S. & Tempesta, G. The 6H-SiC structure model: Further refinement from SCXRD data from a terrestrial moissanite. *American Mineralogist.* doi:10.2138/am.2007.2346 (2007).

[108] Leung, K., Pan, Z. & Warner, D. Atomistic-based predictions of crack tip behavior in silicon carbide across a range of temperatures and strain rates. *Acta Materialia* **77,** 324–334. doi:10.1016/j.actamat.2014.06.016 (Sept. 2014).

[109] Hughes, I. & Hase, T. *Measurements and their uncertainties : a practical guide to modern error analysis* 136 (Oxford University Press, 2010).

[110] Abavare, E. K. K., Iwata, J.-I., Yaya, A. & Oshiyama, A. Surface energy of Si(110)- and 3C-SiC(111)-terminated surfaces. *physica status solidi (b)* **251,** 1408–1415. doi:10.1002/pssb.201350335 (July 2014).

[111] Pollmann, J. & Krüger, P. Reconstruction models of cubic SiC surfaces. *Journal of Physics: Condensed Matter* **16,** S1659–S1703. doi:10.1088/0953-8984/16/17/012 (May 2004).

[112] Starke, U., Bernhardt, J., Schardt, J. & Heinz, K. SiC Surface Reconstruction: Relevancy of Atomic Structure for Gorwth Technology. *Surface Review and Letters* **06,** 1129–1141. doi:10.1142/s0218625x99001256 (Dec. 2002).

[113] Fernandez-Torre, D., Albaret, T. & De Vita, A. Role of Surface Reconstructions in (111) Silicon Fracture. *Physical Review Letters* **105,** 185502. doi:10.1103/PhysRevLett.105.185502 (Oct. 2010).

[114] Togo, A. & Tanaka, I. First principles phonon calculations in materials science. *Scripta Materialia* **108,** 1–5. doi:`10.1016/J.SCRIPTAMAT.2015.07.021` (Nov. 2015).

[115] Chaput, L., Togo, A., Tanaka, I. & Hug, G. Phonon-phonon interactions in transition metals. *Physical Review B* **84,** 094302. doi:`10.1103/PhysRevB.84.094302` (Sept. 2011).

[116] Volkert, C. A. & Minor, A. M. Focused Ion Beam Microscopy and Micromachining. *MRS Bulletin* **32,** 389–399. doi:`10.1557/mrs2007.62` (May 2007).

[117] Mayer, J., Giannuzzi, L. A., Kamino, T. & Michael, J. TEM Sample Preparation and FIB-Induced Damage. *MRS Bulletin* **32,** 400–407. doi:`10.1557/mrs2007.63` (May 2007).

[118] McColm, I. J. *Ceramic Hardness* doi:`10.1007/978-1-4757-4732-4` (Springer US, Boston, MA, 1990).

[119] Henshall, J. L., RowCliffe, D. J. & Edington, J. W. Fracture Toughness of Single-Crystal Silicon Carbide. *Journal of the American Ceramic Society* **60,** 373–375. doi:`10.1111/j.1151-2916.1977.tb15564.x` (July 1977).

[120] Leung, K. W. K., Pan, Z. L. & Warner, D. H. Kohn-Sham density functional theory prediction of fracture in silicon carbide under mixed mode loading. *Modelling and Simulation in Materials Science and Engineering* **24,** 035004. doi:`10.1088/0965-0393/24/3/035004` (Mar. 2016).

[121] Henshall, J. L. & Brookes, C. A. The measurement of KIC in single crystal SiC using the indentation method. *Journal of Materials Science Letters* **4,** 783–786. doi:`10.1007/BF00726990` (June 1985).

[122] Cramer, T., Wanner, A. & Gumbsch, P. Energy Dissipation and Path Instabilities in Dynamic Fracture of Silicon Single Crystals. *Physical Review Letters* **85,** 788–791. doi:`10.1103/PhysRevLett.85.788` (July 2000).

[123] Thomson, R., Hsieh, C. & Rana, V. Lattice Trapping of Fracture Cracks. *Journal of Applied Physics* **42,** 3154–3160. doi:`10.1063/1.1660699` (July 1971).

[124] Curtin, W. A. On lattice trapping of cracks. *Journal of Materials Research* **5,** 1549–1560. doi:10.1557/JMR.1990.1549 (July 1990).

[125] Bernstein, N. & Hess, D. W. Lattice Trapping Barriers to Brittle Fracture. *Physical Review Letters* **91,** 025501. doi:10.1103/PhysRevLett.91.025501 (July 2003).

[126] *Multiscale Materials Modeling* (eds Schmauder, S. & Schäfer, I.) doi:10.1515/9783110412451 (De Gruyter, Berlin, Boston, Jan. 2016).

[127] Hirth, J. P. & Lothe, J. *Theory of Dislocations* 2nd (Wiley, 1982).

[128] *Numerical Continuation Methods for Dynamical Systems* (eds Krauskopf, B., Osinga, H. M. & Galán-Vioque, J.) doi:10.1007/978-1-4020-6356-5 (Springer Netherlands, Dordrecht, 2007).

[129] Chan, T. F. C. & Keller, H. B. Arc-Length Continuation and Multigrid Techniques for Nonlinear Elliptic Eigenvalue Problems. *SIAM Journal on Scientific and Statistical Computing* **3,** 173–194. doi:10.1137/0903012 (June 1982).

[130] Kuznetsov, Y. A. *Elements of Applied Bifurcation Theory* doi:10.1007/978-1-4757-3978-7 (Springer New York, New York, NY, 2004).

[131] Taylor, C. & Dawes, J. H. Snaking and isolas of localised states in bistable discrete lattices. *Physics Letters A* **375,** 14–22. doi:10.1016/J.PHYSLETA.2010.10.010 (Nov. 2010).

[132] Buze, M., Hudson, T. & Ortner, C. Analysis of cell size effects in atomistic crack propagation. arXiv: 1905.13328 (May 2019).

[133] Taha, A. A. & Hanbury, A. An Efficient Algorithm for Calculating the Exact Hausdorff Distance. *IEEE Transactions on Pattern Analysis and Machine Intelligence* **37,** 2153–2163. doi:10.1109/TPAMI.2015.2408351 (Nov. 2015).

[134] Zimmerman, J. A., WebbIII, E. B., Hoyt, J. J., Jones, R. E., Klein, P. A. & Bammann, D. J. Calculation of stress in atomistic simulation. *Modelling and Simulation in Materials Science and Engineering* **12,** S319–S332. doi:10.1088/0965-0393/12/4/S03 (July 2004).

[135] Falk, M. L. & Langer, J. S. Dynamics of viscoplastic deformation in amorphous solids. *Physical Review E* **57,** 7192–7205. doi:`10.1103/PhysRevE.57.7192` (June 1998).

[136] Braun, J., Buze, M. & Ortner, C. The Effect of Crystal Symmetries on the Locality of Screw Dislocation Cores. *SIAM Journal on Mathematical Analysis* **51,** 1108–1136. doi:`10.1137/17M1157520` (Jan. 2019).

[137] Buze, M., Hudson, T. & Ortner, C. Analysis of an atomistic model for anti-plane fracture. arXiv: `1810.05501` (Oct. 2018).